Numerical Simulation of Eastern North Pacific Stratocumulus

By

Joseph H. Wakefield
and
Wayne H. Schubert

Department of Atmospheric Science
Colorado State University
Fort Collins, Colorado

Colorado State University

Department of Atmospheric Science

Paper No. 294

NUMERICAL SIMULATION OF EASTERN NORTH PACIFIC STRATOCUMULUS

Joseph S. Wakefield
Wayne H. Schubert

The research reported here has been supported
by the GARP Section of the Office of Climate
Dynamics, National Science Foundation
Grant ATM 76-09370

Department of Atmospheric Science
Colorado State University
Fort Collins, Colorado 80523

July, 1978

Atmospheric Science Paper No. 294

TABLE OF CONTENTS

TABLE OF CONTENTS Continued

LIST OF TABLES

LIST OF FIGURES

LIST OF FIGURES Continued

LIST OF FIGURES Continued

LIST OF SYMBOLS

English Symbols

b	Dimensionless constant in cloud base equation
c_p	Specific heat of air at constant pressure
C_T	Bulk transfer coefficient
D	Large-scale divergence
$F_L^{\downarrow}$	Downward longwave radiative flux
F_S	Shortwave radiative flux
g	Acceleration of gravity
h	Moist static energy ($h = c_pT + gz + Lq$)
H	Scale height ($H = \frac{RT}{g}$)
k	Entrainment parameter
ℓ	Liquid water mixing ratio
L	Latent heat of condensation
p	Air pressure
q	Water vapor mixing ratio
$(q+\ell)$	Total water mixing ratio
R	Gas constant
s	Dry static energy ($s = c_pT + gz$)
s_v	Virtual dry static energy ($s_v = s + c_pT(\delta q - \ell)$)
t	Time
T	Temperature
V	Horizontal wind speed
w	Vertical wind speed
$\overline{w'X'}$	Vertical turbulent flux of property X

x	Downstream coordinate
z	Height

Greek Symbols

β	Dimensionless constant
γ	Dimensionless constant
δ	Dimensionless constant
ΔX	Jump of property X across cloud top ($\Delta X = X(z_{B+}) - X(z_{B-})$)
ε	Dimensionless constant
ε_L	Longwave radiative emissivity of the cloud
κ	Dimensionless constant ($\kappa = \frac{R}{c_p}$)
λ	Longitude
ρ	Density of air
σ	Stefan-Boltzmann constant
ϕ	Latitude

Subscripts

B	Value at cloud top
C	Value at cloud base
M	Constant value in the mixed layer
S	Value at the surface

Superscripts

+	Just above
-	Just below
*	Saturation value

1. Introduction

A persistent feature of the atmosphere over the eastern portions of the Pacific and Atlantic oceans is the existence of broad areas of stratocumulus corvection. These stratocumulus regimes lie to the east of the large semi-permanent subtropical high pressure centers.

A theoretical study of this stratocumulus convection was carried out by Lilly (1968). Refinements to and further work with his model have been discussed by Schubert (1976), Deardorff (1976), Kraus and Schaller (1977), and Schubert et al. (1977a, b). In addition an observational program (the Marine Stratocumulus Experiment) was carried out in 1976 (Wakefield and Schubert, 1976) with the intent of verifying some of the features of the model.

That the stratocumulus are a persistent feature of the general circulation may be seen by examination of Figures 1.1 and 1.2. Figure 1.1 shows the mean relative July cloud cover for 1967-1970, as presented by Miller and Feddes (1971). Presented in Figure 1.2 are the results of Neiburger et al.'s (1961) compilation of observational data, which indicates that inversions exist 80-100% of the time in summer in the region indicated as persistently cloudy in Figure 1.1.

The general features of a stratocumulus-topped mixed layer are illustrated in Figure 1.3. Turbulent mixing below the inversion creates a layer in which thermodynamic properties are constant with height. In the case of a cloud-topped mixed layer, the well-mixed variables are moist static energy h and total water mixing ratio $q+\ell$. The data in Figure 1.3 below 80 kPa are taken from an aircraft sounding during the Marine Stratocumulus Experiment, while the rest are

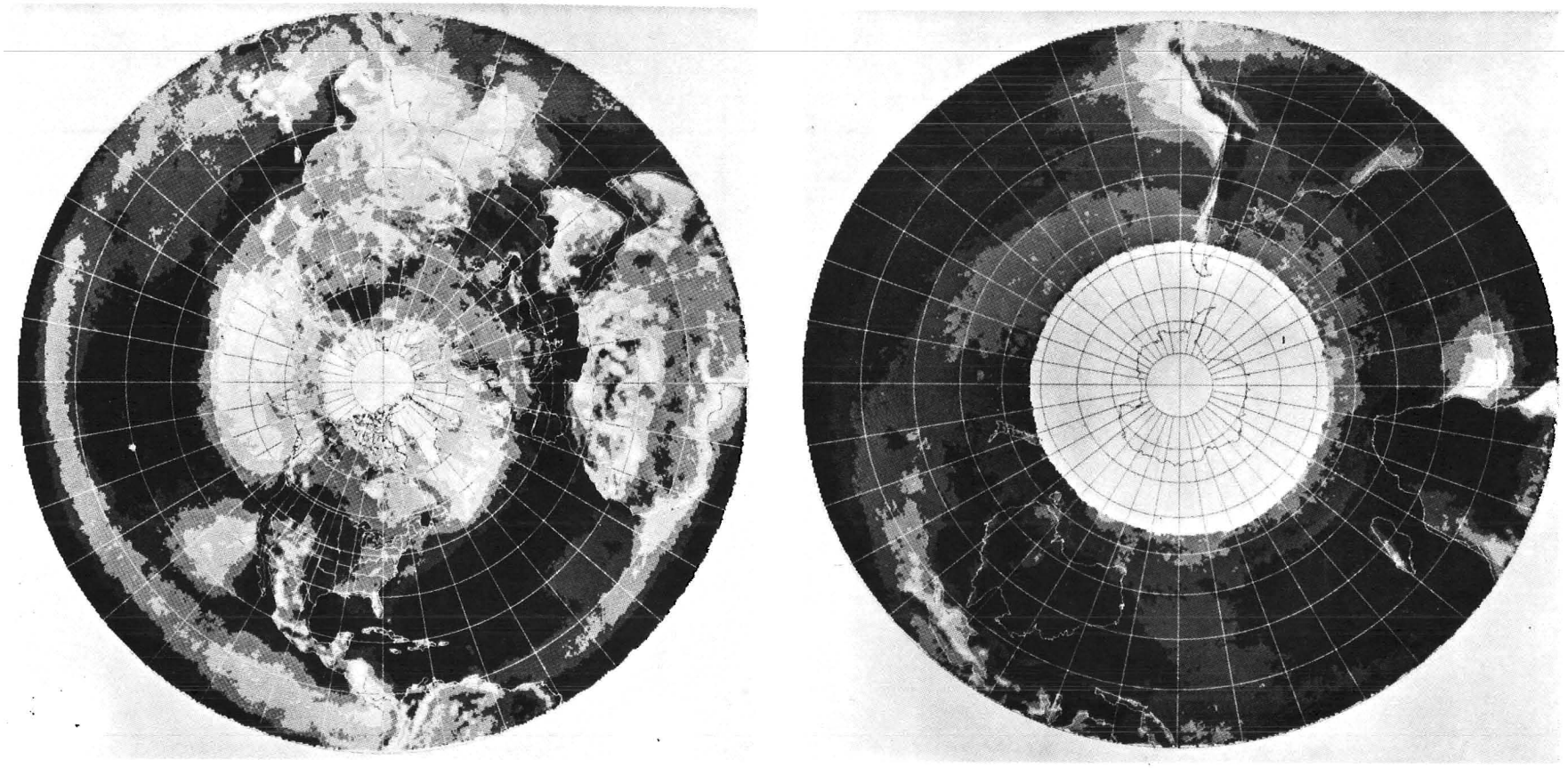

Figure 1.1 Mean July relative cloud cover
(from Miller and Feddes, 1971).

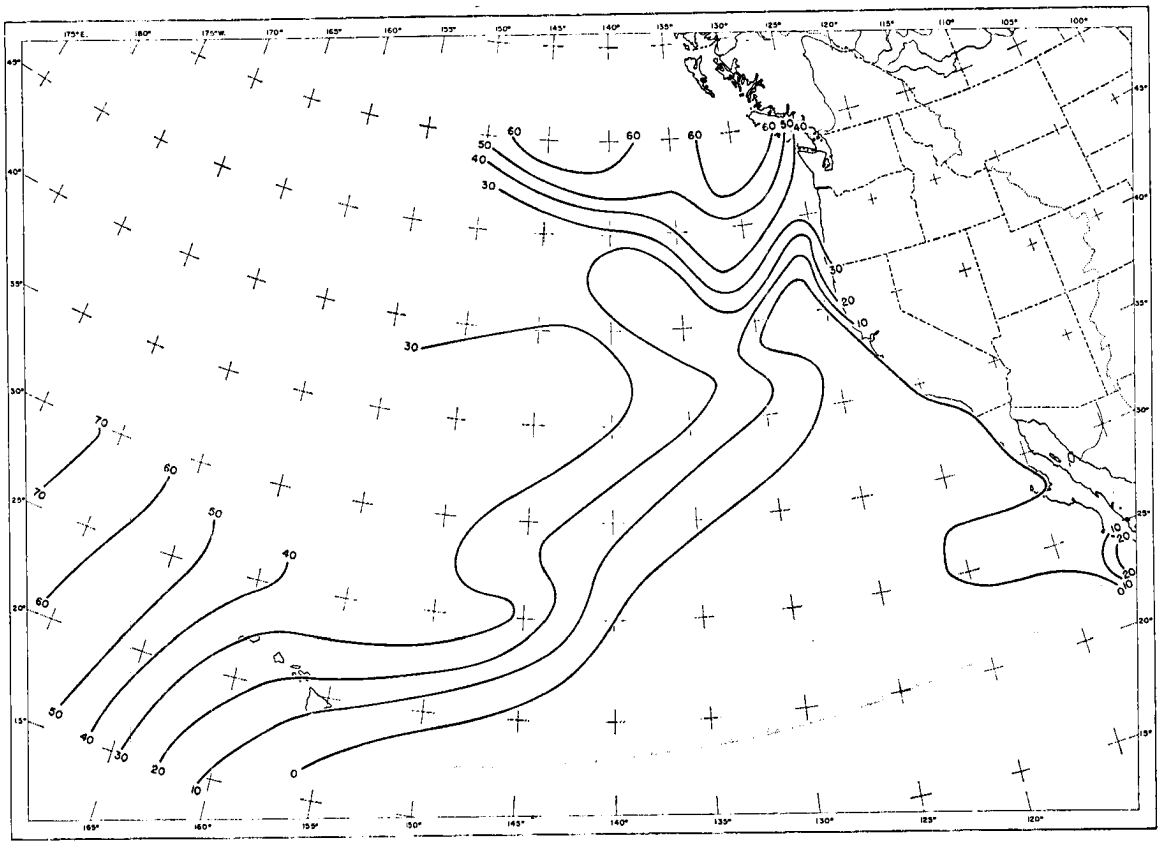

Figure 1.2 Percent of observations with no inversion for the period June through September (from Neiburger et al., 1961). An inversion has always been found in shaded areas.

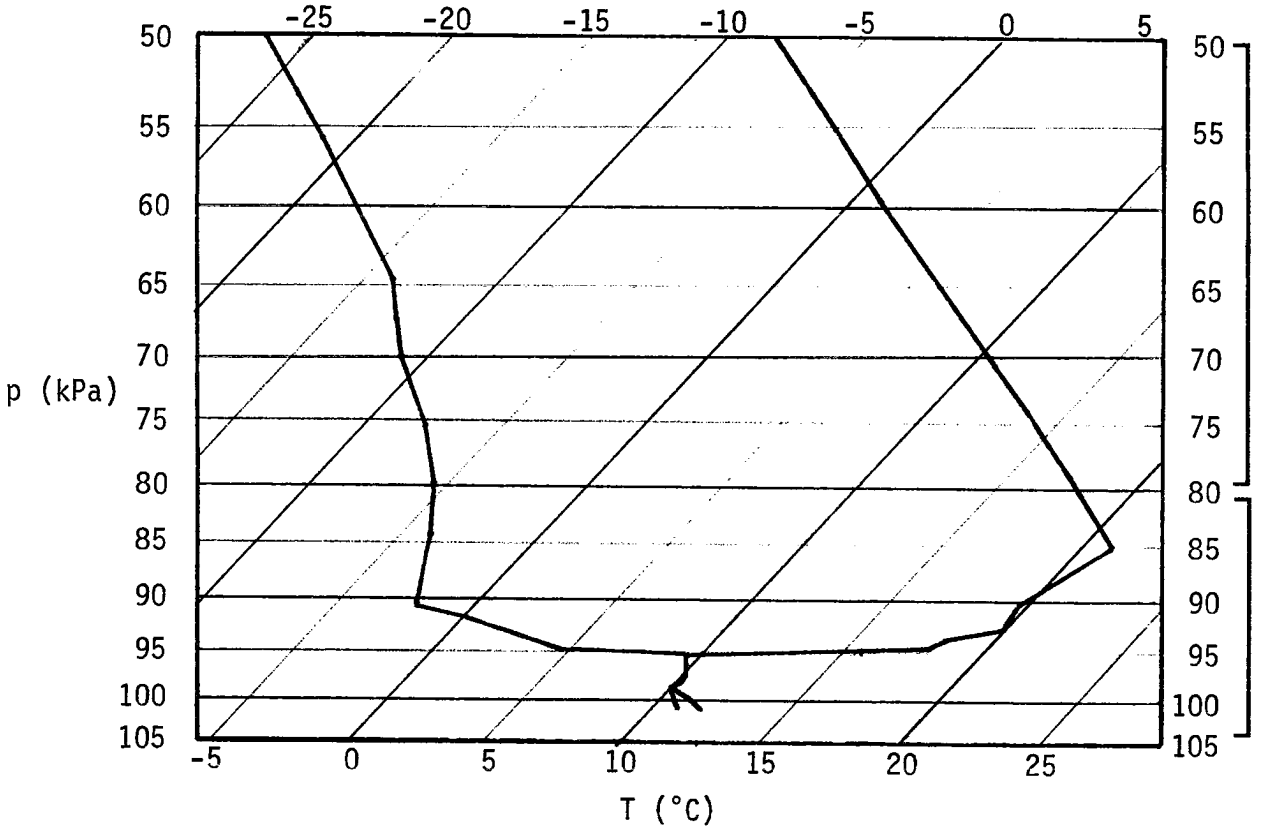

Figure 1.3 Temperature and dew point data from an NCAR Electra sounding near 37.8°N and 125.0°W, 17 June 1976.

from a mean July Oakland sounding. While a rather extreme case, it does serve to illustrate the significant warming and drying above the mixed layer.

The model to be employed in this study relates the mixed layer properties to various external parameters. The inputs to and outputs of the model are listed in Table 1.1.

Table 1.1. Summary of model inputs and outputs.

MODEL INPUTS	MODEL OUTPUTS
sea surface temperature, T_S	cloud top height, z_B
surface wind speed, V	cloud base height, z_C
large-scale divergence, D	mixed layer moist static energy, h_M
shortwave absorption in the mixed layer, ΔF_S	mixed layer total water mixing ratio, $(q+\ell)_M$
moist static energy above the mixed layer, $h(z_{B+})$	temperature at cloud top, $T(z_{B-})$
water vapor mixing ratio above the mixed layer, $q(z_{B+})$	profiles of the turbulent fluxes of moist static energy, $\overline{w'h'}$ and total water, $\overline{w'(q'+\ell')}$
downward longwave radiative flux above the mixed layer, $F_L^{\downarrow}(z_{B+})$	

Over land, the driving force for convection is surface heating. An upward flux of heat from the ground destabilizes the atmosphere, leading to convective overturning and mixing. In the stratocumulus case, the large surface heating observed over land does not occur, and

the driving mechanism for the convective mixing is the radiational cooling at the top of the mixed layer.

Figure 1.4 conceptually illustrates the convective mechanism in marine stratocumulus convection. Radiative cooling and the inversion warming and drying (which are caused by large-scale subsidence) lead to turbulent vertical fluxes of heat and moisture at the top of the layer. These fluxes in turn affect the mixed layer properties, which feed back into both the magnitude of the inversion and the radiative cooling. Mixed layer values of heat and moisture determine the surface fluxes, as well. These surface fluxes feed back into both the mixed layer properties and the cloud-top fluxes, completing the loop.

The purpose of this paper is to numerically simulate the stratocumulus convection of the eastern North Pacific and to compare it to the observational evidence of Neiburger et al. (1961). The model is presented in Chapter 2, and its radiative aspects are discussed in Chapter 3. Chapter 4 presents the large-scale input fields, and Chapter 5, the results of the numerical integrations.

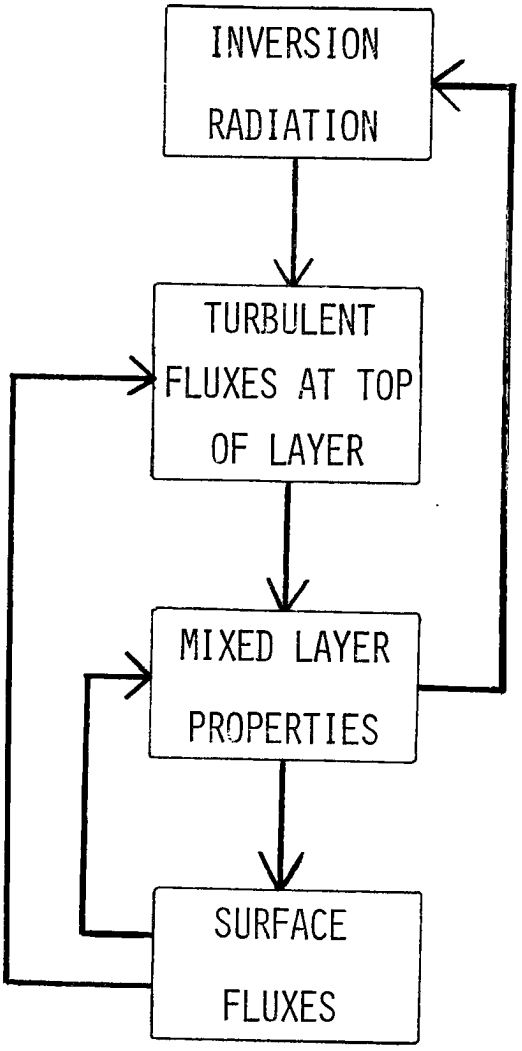

Figure 1.4. Conceptual flow diagram of marine stratocumulus convection process.

2. Governing equations

The model employed in this study is a slightly modified form of that used by Schubert et al. (1978a). More detailed descriptions of the set of equations may be found in that study, as well as in the original paper by Lilly (1968) and in Schubert (1976).

The model may be written as a set of twelve equations, and is summarized below:

$$(\overline{w'h'})_S = C_T V[h_S^* - h_M] \ , \tag{2.1}$$

$$(\overline{w'q'})_S = C_T V[q_S^* - (q+\ell)_M] \ , \tag{2.2}$$

$$\frac{z_C}{H} = \frac{(1+\gamma)[q_S^* - (q+\ell)_M] - \frac{\gamma}{L}[h_S^* - h_M]}{b} \ , \tag{2.3}$$

$$\Delta h = h(z_{B+}) - h_M \ , \tag{2.4}$$

$$\Delta(q+\ell) = q(z_{B+}) - (q+\ell)_M \tag{2.5}$$

$$T(z_{B-}) = \frac{1}{c_p}\left[h_M - L(q+\ell)_M + \frac{Lb}{(1+\gamma)H}(z_B - z_C) - gz_B\right] \ , \tag{2.6}$$

$$\Delta F_L = \varepsilon_L [\sigma T^4(z_{B-}) - F_L^{\downarrow}(z_{B+})] \ , \tag{2.7}$$

$$\left\{\beta\left[1-\left(\frac{z_C}{z_B}\right)^2\right]+\left(\frac{z_C}{z_B}\right)^2\right\}\overline{(w'h')}_B-\left\{\varepsilon\left[1-\left(\frac{z_C}{z_B}\right)^2\right]+(1-\varepsilon\delta)\left(\frac{z_C}{z_B}\right)^2\right\}L\overline{w'(q'+\ell')}_B$$

$$+\left\{\beta\left(\frac{z_B-z_C}{z_B}\right)^2+\left[1-\left(\frac{z_B-z_C}{z_B}\right)^2\right]\right\}\overline{(w'h')}_S-\left\{\varepsilon\left(\frac{z_B-z_C}{z_B}\right)^2+(1-\varepsilon\delta)\left[1-\left(\frac{z_B-z_C}{z_B}\right)^2\right]\right\}L\overline{(w'q')}_S$$

$$+\frac{1-k}{k}\min\left\{\begin{array}{c}\beta\overline{(w'h')}_B-\varepsilon L\overline{w'(q'+\ell')}_B\\ \left[\frac{z_B-z_C}{z_B}\overline{(w'h')}_S+\frac{z_C}{z_B}\overline{(w'h')}_B\right]-(1-\varepsilon\delta)L\left[\frac{z_B-z_C}{z_B}\overline{(w'q')}_S+\frac{z_C}{z_B}\overline{w'(q'+\ell')}_B\right]\\ \overline{(w'h')}_S-(1-\varepsilon\delta)L\overline{(w'q')}_S\end{array}\right\}=0\,. \tag{2.8}$$

$$\frac{L\Delta(q+\ell)}{\Delta h}\overline{(w'h')}_B-L\overline{w'(q'+\ell')}_B=\frac{L\Delta(q+\ell)}{\Delta h}\rho^{-1}\Delta F_L\,, \tag{2.9}$$

$$\frac{dh_M}{dt}=\frac{\overline{(w'h')}_S-\overline{(w'h')}_B+\rho^{-1}\Delta F_S}{z_B}\,, \tag{2.10}$$

$$\frac{d(q+\ell)_M}{dt}=\frac{\overline{(w'q')}_S-\overline{w'(q'+\ell')}_B}{z_B}\,, \tag{2.11}$$

$$\frac{dz_B}{dt}=-Dz_B+\frac{\rho^{-1}\Delta F_L-\overline{(w'h')}_B}{\Delta h}\,. \tag{2.12}$$

(The notation $\frac{d}{dt}$ here is interpreted as $\frac{\partial}{\partial t}+V\frac{\partial}{\partial x}$, where x is distance in the downstream direction, since the numerical integration proceeds along a streamline.)

Including the effects of both water vapor and liquid water on buoyancy, the virtual dry static energy, s_v, is defined as

$$s_v = s + c_p T(\delta q - \ell) \ , \tag{2.13}$$

where $\delta = 0.608$ and T is a constant reference temperature. By the definition of γ (equation (2.16)),

$$(1+\gamma)L\overline{w'q'} = \gamma\overline{w'h'} \quad \text{for} \quad z_C < z < z_B \ , \tag{2.14}$$

and the turbulent flux of virtual dry static energy may be written

$$\overline{w's_v'} = \begin{cases} \beta\,\overline{w'h'} - \varepsilon L\overline{w'(q'+\ell')} & z_C < z < z_B \qquad (2.15a) \\ \\ \overline{w'h'} - (1-\varepsilon\delta)L\overline{w'(q'+\ell')} & 0 < z < z_C \ , \qquad (2.15b) \end{cases}$$

where

$$\beta = \frac{1+\gamma\varepsilon(\delta+1)}{1+\gamma} \ , \qquad \gamma = \frac{L}{c_p}\left(\frac{\partial q^*}{\partial T}\right)_p \ , \qquad \varepsilon = \frac{c_p T}{L} \ . \tag{2.16}$$

Making use of (2.15), (2.8) is an integrated form of

$$\frac{k}{z_B}\int_C^{z_B} \overline{w's_v'}\,dz + \tfrac{1}{2}(1-k)(\overline{w's_v'})_{min} = 0 \ , \tag{2.17}$$

which is the assumed entrainment relation.

Since the layer is assumed to be well mixed, the fluxes of h and $(q+\ell)$ are linear with height below z_B. Therefore, (2.15) indicates that the s_v flux is linear below cloud and within the cloud, with a

discontinuity at cloud base. It might seem, then, that the minimum s_v flux appearing in (2.17) could occur at one of four locations: at the surface, just below cloud base, just above cloud base, or at cloud top. It has been demonstrated by Schubert et al. (1978a) that the flux increases across cloud base, and thus the minimum cannot occur at z_{C+}. The three lines inside the large brackets in (2.8) correspond to the three remaining possible solutions.

Equations (2.8) and (2.9) may be combined in a more convenient notation as

$$\begin{bmatrix} a_{11} & a_{12} \\ a_{21} & a_{22} \end{bmatrix} \begin{bmatrix} (\overline{w'h'})_B \\ L\overline{w'(q'+\ell')}_B \end{bmatrix} = \begin{bmatrix} b_1 \\ b_2 \end{bmatrix}, \qquad (2.18)$$

(2.19)

Equations (2.1) and (2.2) are bulk aerodynamical formulae for the surface fluxes of moist static energy, h, and water vapor mixing ratio, q. The transfer coefficient C_T is given by

$$C_T = (1 + 0.07\,V) \times 10^{-3}, \qquad (2.20)$$

(for V in ms^{-1}) as suggested by Deacon and Webb (1962). It can be seen from the form of (2.1) and (2.2) that the surface fluxes are proportional to wind speed and to the difference between the saturation value at the sea surface temperature and pressure and the mixed layer value.

Cloud base z_C is given by (2.3) as a function of the air-sea differences in h and q, the scale height H, and two dimensionless constants γ and b, where b is given by

$$b = \frac{RT}{c_p}\left(\frac{\partial q^*}{\partial p}\right)_p + p\left(\frac{\partial q^*}{\partial p}\right)_T = \kappa\varepsilon\gamma + p\left(\frac{\partial q^*}{\partial p}\right)_T \quad . \tag{2.21}$$

Equation (2.3) is an expression for the level at which the atmosphere will become saturated, i.e. where $q^* = (q+\ell)_M$. The constant b (b is an increasing function of temperature and a decreasing function of pressure) is simply the lapse rate of q^*.

Equations (2.4) and (2.5) are the cloud top jumps in moist static energy and total water mixing ratio, while the temperature just below cloud top and the cloud top jump of longwave radiation are given by (2.6) and (2.7). Cloud-top temperature is determined by following a dry adiabat to cloud base and a moist adiabat from there to cloud top. The first two terms on the right-hand side give the surface air temperature, and the last term gives the cooling due to dry adiabatic ascent. The third term represents the addition of heat due to condensation of water vapor within the cloud layer.

Equation (2.8) is, as noted above, the entrainment relation, and (2.9) expresses the relationship between the jumps of total water and moist static energy as implied by the budget equations for h and $(q+\ell)$ at the top of the layer,

$$\left(\frac{dz_B}{dt} - w_B\right)\Delta h + \overline{w'h'}_B = \rho^{-1}\Delta F_L \quad , \tag{2.22}$$

$$\left(\frac{dz_B}{dt} - w_B\right)\Delta(q+\ell) + \overline{w'(q'+\ell')}_B = 0 \quad . \tag{2.23}$$

The remaining three equations, (2.10) - (2.12), are predictive equations for the mixed layer (constant with height) values of h and $q+\ell$, and for the cloud top height, z_B.

Given a knowledge of sea surface temperature, winds, and divergence, as well as upper level (i.e. above the mixed layer) q, h, and $F_L^{\downarrow}$ profiles, the system (2.1) - (2.7), (2.18), (2.19), and (2.9) - (2.12) may be numerically integrated as follows:

1. Assume initial conditions for h_M, $(q+\ell)_M$, and z_B.
2. Compute the surface fluxes of h and q from (2.1) and (2.2).
3. Compute cloud base from (2.3).
4. Compute the cloud top jumps of h and $(q+\ell)$ from (2.4) and (2.5).
5. Compute the cloud top temperature from (2.6) and the cloud top jump in net longwave radiative flux from (2.7).
6. Solve the system (2.18) and (2.19) for the cloud top fluxes of h and $(q+\ell)$.
7. Predict new values of h_M, $(q+\ell)_M$, and z_B from (2.10) - (2.12).
8. Return to step 2.

The solution of (2.18) and (2.19) is not trivial. The form of (2.8) shows that in order for a solution to be found, the location of the minimum s_v flux must be known. From (2.15), it can be seen that this means that the fluxes of h and $(q+\ell)$ at cloud top must also be known. To solve (2.18) and (2.19), therefore, we assume that the

minimum occurs at each of the three possible levels, solve the matrix, and, in each case, use (2.15) to check the location of the minimum. In all cases we have found that a solution exists, and in those few cases where more than one solution exists, we have found that by using the solution with the minimum closer to the surface, the integration proceeds in an orderly manner.

3. Radiation

A recent difference in modeling technique among modelers of stratocumulus convective has been the treatment of radiation. Compare, for example, Lilly (1968) and Schubert (1976) with Deardorff (1976). In the former, longwave radiation is considered only at cloud top, where an instantaneous (in the vertical) jump in longwave radiative flux supplies the cooling at cloud top needed to destabilize the atmosphere and drive the convection. Deardorff, on the other hand, argued that "some [of the cooling] should be allowed to occur in the upper mixed layer just below the thermal jump", which has the effect of adding a layer to the model.

While it is not the purpose of this work to present an extensive discussion of the treatment of radiation, we have performed some experiments with the radiative formulation of Lilly (1968). It has been assumed that both the temperature and moisture of a parcel of air go through instantaneous jumps as the parcel passes through the top of the mixed layer. It seems appropriate, therefore, to deal with the radiation in a similar manner, i.e. to allow the longwave cooling to occur in an infinitesimally thin layer at cloud top. That this sort of treatment is not inappropriate may be seen by comparing Schubert et al.'s (1978 a, b) calculations of turbulent fluxes for a simulated Air Mass Transformation Experiment (AMTEX) case with those observed during AMTEX.

Presented in the left-hand column of Table 3.1 are values of turbulent fluxes of moisture and dry static energy at the air-sea interface adapted from Agee and Howley (1977) from a cold period of AMTEX 74. The moist static energy flux is simply the sum of the dry static energy and water vapor mixing ratio fluxes, since both are reported in the same units. The right-hand columns present results from Schubert et al. (1978b). (In this case the dry static energy flux is the difference between the moist static energy and water vapor fluxes.) Each of the three fluxes is shown at its maximum. The agreement between the model results and actual observations is rather good, especially considering that the sea surface temperature data were hypothesized and were not taken from observations. These results do not indicate that the radiation treatment is significantly flawed.

Further support for the cloud-top radiative jump hypothesis can be found in the results of the longwave transfer model of Cox (1973). The model was run for a case observed during the Marine Stratocumulus Experiment, using as input the sounding shown in Figure 1.3. The radiative profiles produced by the model are presented in Figure 3.1. While the radiative divergence is not confined entirely to the top of the cloud, it can be seen that of the total cooling of 43 watts per square meter, 37 or 86% occurs in the uppermost layer of the model. (The vertical resolution of the input sounding limits the depth of maximum cooling to a minimum of forty meters.)

3.1 Longwave emissivity

It was felt that one deficiency with the treatment of radiation in the model of Schubert et al. (1978b) was that the longwave cooling

Table 3.1. Observed and calculated sensible and latent heat fluxes (W m^{-2}). Model results are presented for the maximum in each of the three fluxes.

	AMTEX OBSERVATIONS	MODEL CALCULATIONS		
		Fluxes when $\overline{\rho w's'}_S$ is maximum	Fluxes when $\overline{\rho w'q'}_S$ is maximum	Fluxes when $\overline{\rho w'h'}_S$ is maximum
$\rho(\overline{w'h'}_S - L\overline{w'q'}_S)$	235	189	121	172
$\rho L\overline{w'q'}_S$	532	508	574	560
$\rho\overline{w'h'}_S$	767	697	695	732

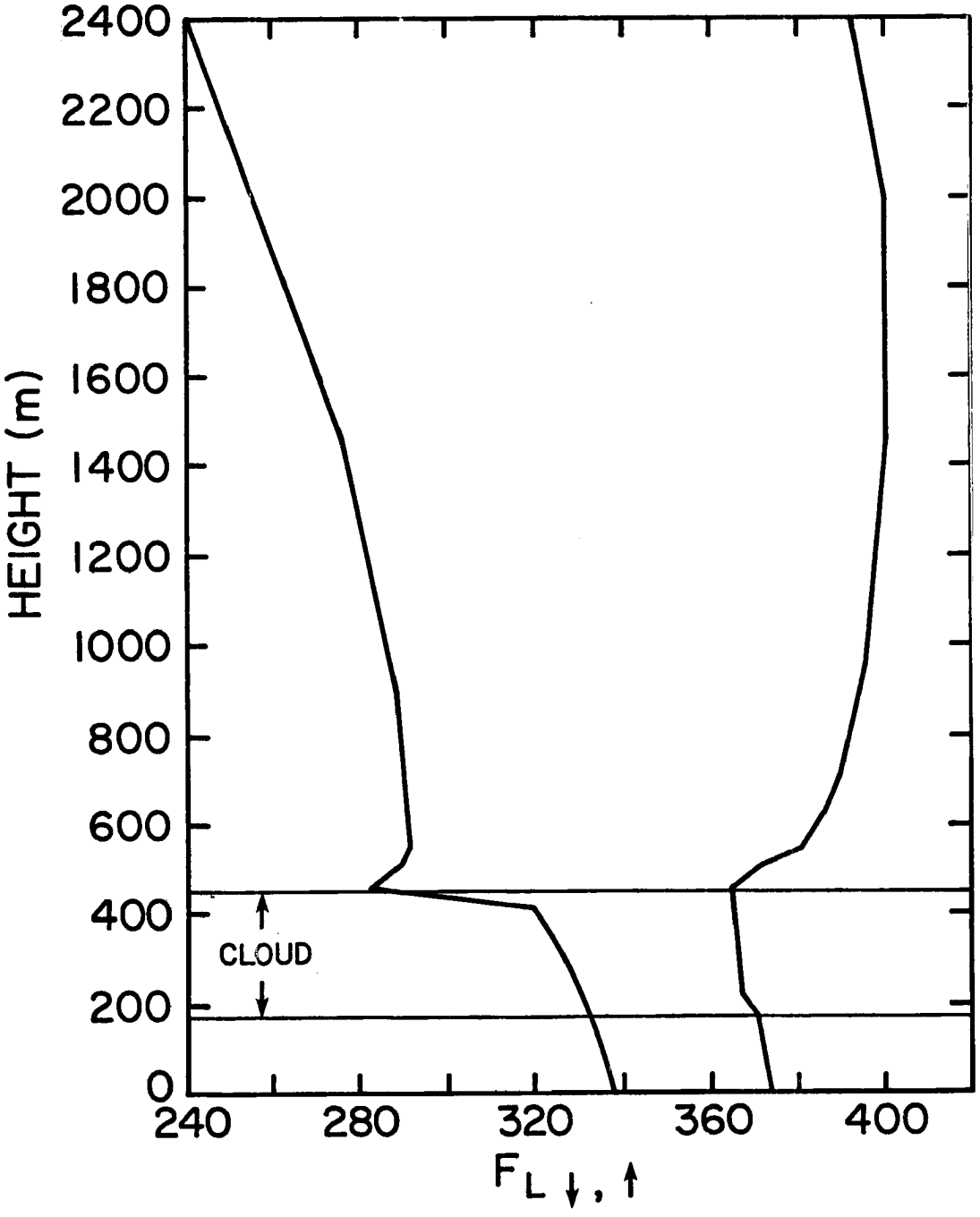

Figure 3.1 Upward and downward longwave radiative fluxes ($W m^{-2}$), from the longwave transfer model of Cox (1973). Input data are from Figure 1.3.

occurring at cloud top was based solely on the cloud-top temperature and the radiation field above the mixed layer. In fact, however, the amount of cooling depends to a significant degree on the optical thickness of the cloud. Thus it was determined that the cooling should be tempered by a longwave emissivity in order that it more closely approximate the conditions existing in the atmosphere.

Recognizing that the cooling off of a thin cloud approaches zero as its thickness approaches zero, the calculated cooling is multiplied by a depth-dependent longwave emissivity, ε_L. The function chosen to represent ε_L as determined by the thickness of the cloud is

$$\varepsilon_L = 0.5 + 0.5 \tanh \left(\frac{\ell n \left((z_B - z_C) / 50 \right)}{2} \right), \qquad (3.1)$$

where the thickness is given in meters. This function, as well as several authors' calculations of longwave emissivity, is illustrated in Figure 3.2. Sources of and notes on each of the curves presented are listed in Table 3.2.

It is immediately evident that the number density and size of the cloud droplets (and therefore the liquid water content of the cloud) have a major effect on the emissivity for any given cloud thickness. Also, the observational evidence (curves 6 and 7), while sparse, does not seem to fit very well with the theory. Note however that Paltridge (1971) reports an emissivity of 0.85 for a 180 m thick cloud. This point is indicated in Figure 3.2 by an asterisk, and seems to fit in very well with the theoretical curves.

The formula employed in this study appears to fall rather short in the region between 100 m and 1000 m (latter not shown). In light

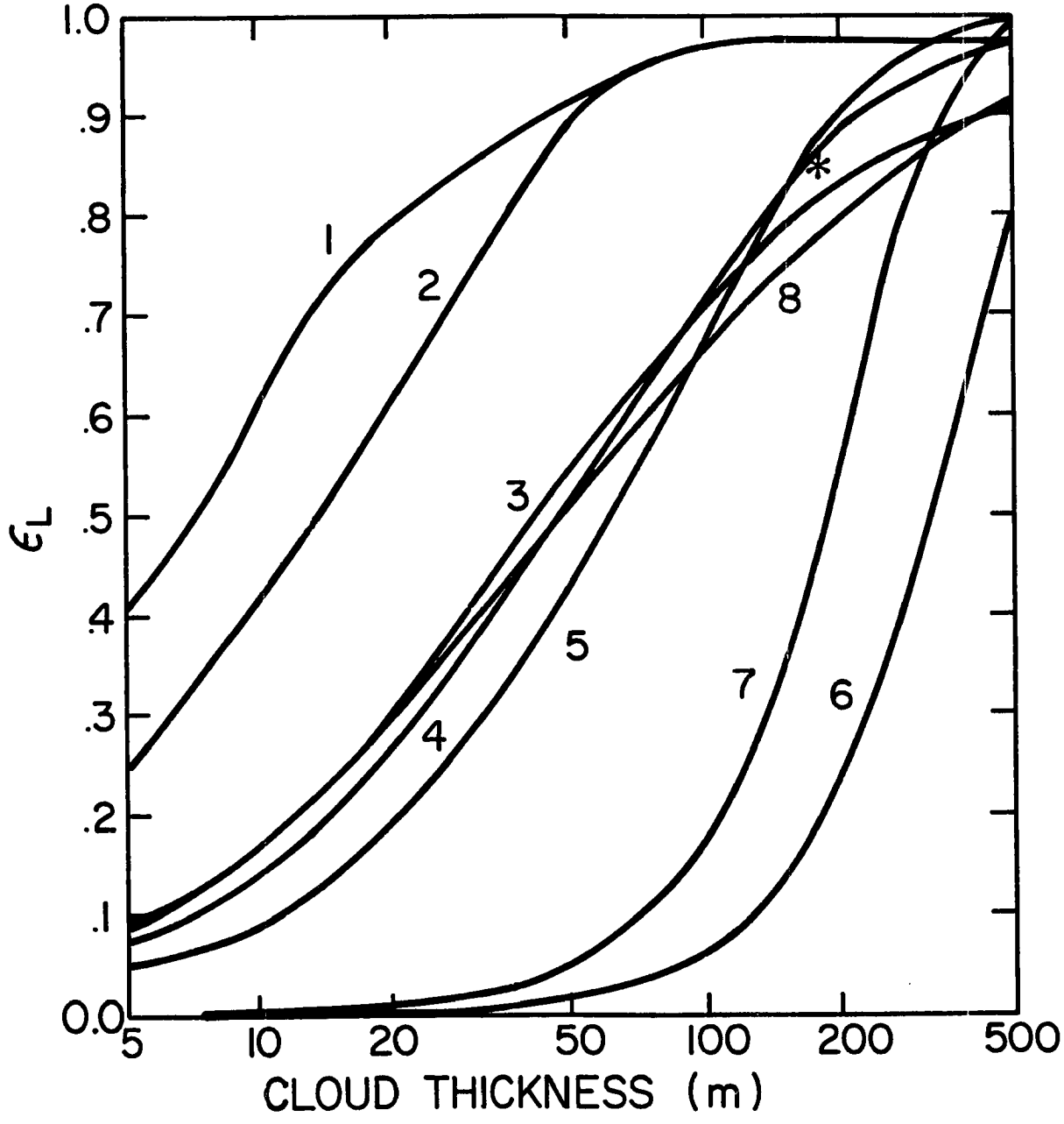

Figure 3.2 Longwave emissivity as a function of cloud thickness. Sources are given in Table 3.2. The function used in this study is line 8.

Table 3.2. Sources of and notes on the longwave emissivity curves presented in Figure 3.2.

CURVE	SOURCE	NOTES
1	Yamamoto et al., 1970	$\lambda = 5 - 50\ \mu m$; $N = 450\ cm^{-3}$; $\bar{\ell} = 0.28\ g\ m^{-3}$
2	Yamamoto et al., 1970	Same as curve 1 except $\lambda = 10.6\ \mu m$.
3	Yamamoto et al., 1966	$\lambda = 8 - 12\ \mu m$; $N = 200\ cm^{-3}$
4	Zdunkowski and Crandall, 1971	$\lambda = 10.6\ \mu m$; $\bar{\ell} = 0.1\ g\ m^{-3}$; $r_m = 5\ \mu m$
5	Hunt, 1973	$\lambda = 11\ \mu m$; $N = 200\ cm^{-3}$; $r_m = 4\ \mu m$
6	Paltridge, 1974	Based on observations.
7	Paltridge, 1974	Same as curve 6, but uses liquid water content data from Neiburger (1949).
8	This study	$\varepsilon_L = 0.5 + 0.5 \tanh\left(\frac{\ell n\left((z_B - z_C)/50\right)}{2}\right)$

of the rather precarious nature of the emissivity determination as a whole, this cannot be considered as too significant an error. Nevertheless, further investigation into this representation of the emissivity will be made in a later section.

3.2 Shortwave absorption

A second, and perhaps more significant, deficiency lies in the model's inclusion of shortwave heating. In Schubert et al.'s formulation, the shortwave heating is applied as a constant value at cloud top. It was felt that here, too, the shortwave absorption should be expressed as a function of cloud thickness.

That this shortcoming of the model may be more significant than the longwave emissivity problem lies in the fact that more longwave than shortwave radiation is absorbed in a given vertical distance through a cloud. The term absorption length will be used here to describe a characteristic distance over which the radiative flux is reduced to some fraction of its value above the cloud. Since most of the clouds with which this model deals are thicker than 100 - 200 meters, the variation in longwave emissivity is not very pronounced. As we shall see, however, the shortwave absorption does not reach its maximum value until the cloud is greater than 1000 m thick.

In developing a function describing the shortwave absorption with cloud thickness, the general approach of Deardorff (1976) was followed. He presented the shortwave radiative flux as

$$\frac{\partial F_S}{\partial z} = a + b\, e^{-(z_B - z)/\lambda}, \qquad (3.2)$$

where $a \approx .004$ W m^{-3}, $b \approx .025$ W m^{-3}, and λ is an absorption length. Equation (3.2) may be integrated through the cloud layer, such that, for constant λ,

$$\Delta F_S \equiv F_{S(z_B)} - F_{S(z_C)} = a(z_B - z_C) + b\lambda\left(1 - e^{-(z_B - z_C)/\lambda}\right). \qquad (3.3)$$

The absorption length λ should not, however, be interpreted as a constant. It should, on the other hand, decrease as the liquid water content of the atmosphere increases. A brief discussion of this problem is included in Oliver et al. (1978), from which the approximate relation $\lambda \approx 500/\bar{\ell}$ m is derived, where $\bar{\ell}$ is the average liquid water mixing ratio of the cloud (in g kg^{-1}). Coupling this with Neiburger's (1949) observation that $\bar{\ell} \approx (z_B - z_C)/5000$ g kg^{-1} we find that $\lambda \approx 2.5 \times 10^{-6}/(z_B - z_C)$, so

$$\Delta F_S = 0.004(z_B - z_C) + \frac{62500}{z_B - z_C}\left(1 - e^{-(z_B - z_C)^2/2.5 \times 10^6}\right) \text{W m}^{-2}. \qquad (3.4)$$

Equation (3.4) is plotted in Figure 3.3, along with the curves for three different constant absorption lengths, λ. The effects of assuming constant λ can easily be seen to lead to large differences in solar absorption.

A second adjustment to the model with regard to shortwave absorption was made. As stated previously, the shortwave heating had been applied at cloud top as a moderation to the calculated longwave cooling (i.e. in equation (2.7)). In the interest of improving the diurnal response of the model to shortwave heating, the ΔF_S term was taken from cloud top into the mixed layer, where it serves to heat

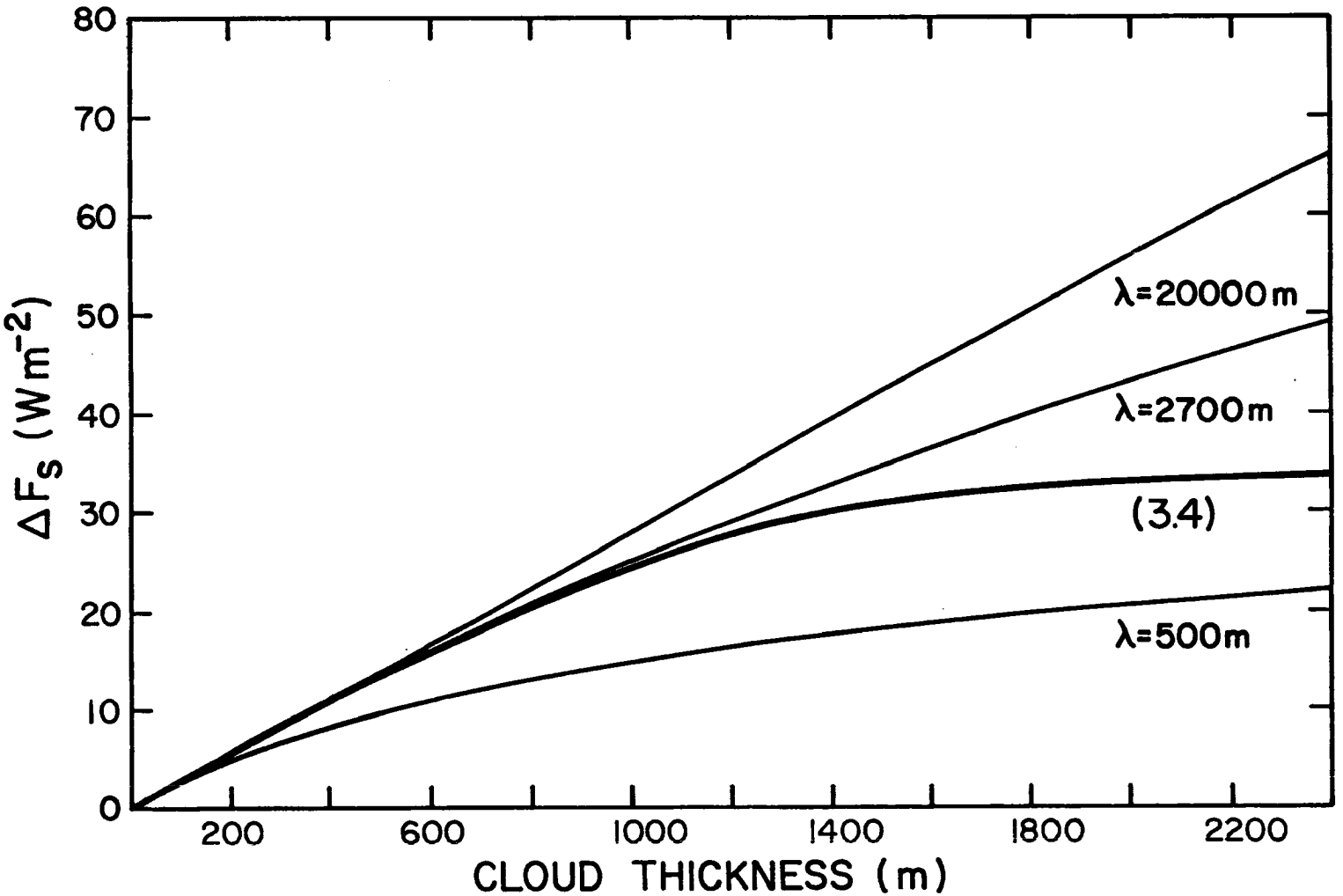

Figure 3.3 Shortwave absorption in the mixed layer as a function of cloud thickness. Also shown are curves for three different constant values of λ in (3.3).

the layer. This seems logical when the longer absorption length for shortwave radiation is considered. This will be examined in more detail in the next section.

Before proceeding to that point, however, a couple of things should be noted with regard to the shortwave radiation. The first of these is that the numbers presented here are intended to represent daily average values of shortwave absorption, i.e. including the nighttime part of each solar cycle. Lilly (1968) quotes a July 24-hour average solar absorption of 22.3 W m^{-2} (which is the value assumed also by Schubert (1976) and Schubert et al. (1978a)), which corresponds to a cloud depth of approximately 875 m in our case. Secondly, it should be noted that no provision for latitude is made in (3.4), but it can be shown using the results of Davis et al. (1978) that the range of solar absorption in a cloud of a given thickness is not more than about 15% over the latitude band 20° to 50°N in July.

3.3 Tests of the radiative parameterizations

Several tests were run in order that the effects of the radiative parameterizations be adequately understood. The results of two series of tests are presented below.

3.3.1 Sensitivity

The model was run several times over the varying external parameters illustrated in Figure 3.4. These are from one of the trajectories which will be described in Chapter 4. The experiments to be described in this section are summarized in Table 3.3.

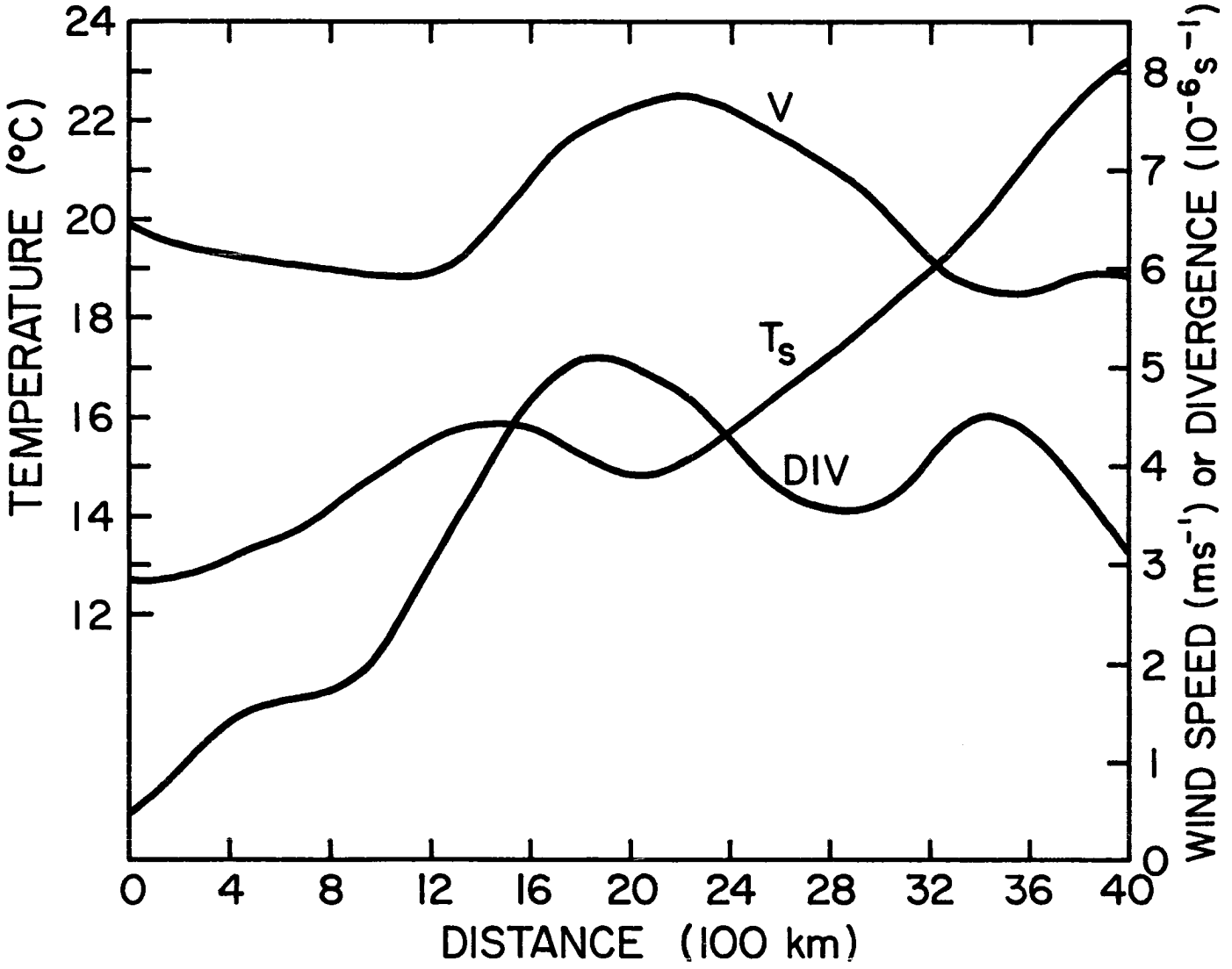

Figure 3.4 Wind speed, sea surface temperature, and large-scale divergence over which several test runs were made.

Table 3.3. Emissivity and absorption functions for the various sensitivity tests.

Experiment Number	Longwave Emissivity	Shortwave Absorption
1	1.0 (constant)	22.3 W m^{-2} (constant)
2	$0.5 + 0.5 \tanh\left(\frac{\ell n\left((z_B - z_C)/50\right)}{2}\right)$	Function of cloud thickness, applied to ΔF_L.
3	$0.5 + 0.5 \tanh\left(\frac{\ell n\left((z_B - z_C)/50\right)}{2}\right)$	Function of cloud thickness, applied to h_M equation.
4	$0.5 + 0.5 \tanh\left(\frac{\ell n\left((z_B - z_C)/50\right)}{1.7}\right)$	Function of cloud thickness, applied to h_M equation.

Experiment 1 is the Schubert et al. (1978a) method, experiments 2 and 3 employ the modifications discussed in sections 3.1 and 3.2, and experiment 4 explores the effect of having the longwave emissivity fall short in the 100 - 1000 m cloud thickness cases (see Figure 3.2 and accompanying discussion).

The parameter most obviously affected by any changes in the treatment of radiation is of course the cooling at cloud top. In the "old" formulation of the model, the cooling is the sum of the longwave cooling and the shortwave heating. In the present form, the cooling is not tempered by shortwave heating, and so the net cooling driving the system is larger. The cooling at cloud top for the four experiments is shown in Figure 3.5. Note that the difference between

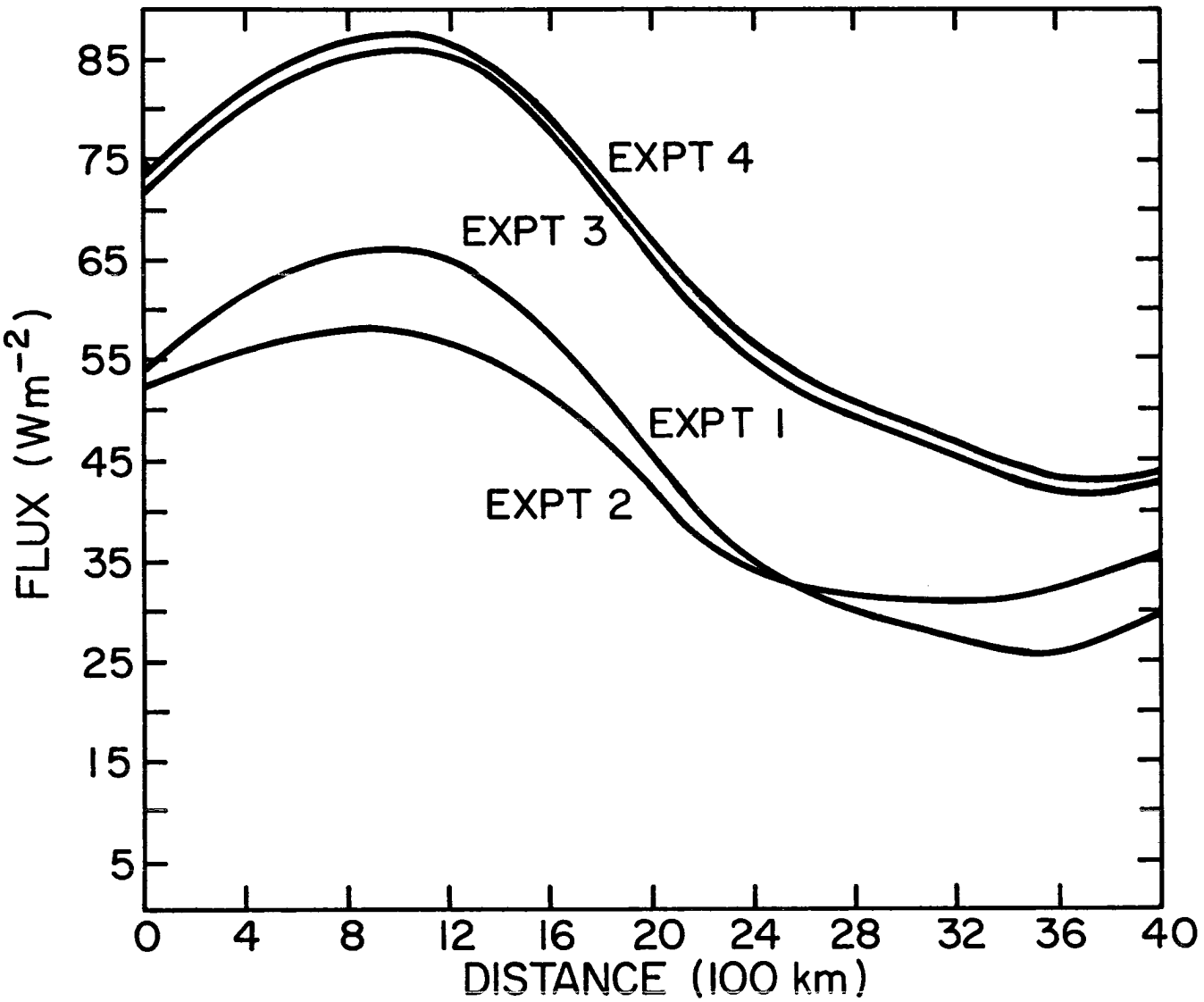

Figure 3.5 Cloud-top radiative jump results for the four experiments listed in Table 3.3.

experiments 1 and 2 is small, but is largest where the thickness deviates the most from 850 m (where the shortwave absorption is approximately equal in the two cases). Note also that the difference between experiments 3 and 4 is negligible. The difference between 1 and 2 and 3 and 4 is about 20 W m^{-2}, which corresponds to clouds approximately 750 meters thick. Cloud thickness actually ranged from about 750 m at the start to 1150 m at 1100 km to 250 m at the end of the experiments. The increase in cooling at the end of the experiments is associated with the increase in sea surface temperature. Cooling is primarily governed, however, by the cloud top height, which is shown in Figure 3.6a. Cloud base height is illustrated in Figure 3.6b.

It can be easily seen in Figure 3.6a that the relative difference between experiments 2 and 3 is considerably smaller in the case of cloud top height than in the case of radiative cooling. This can be readily understood by referring to (2.7) and (2.10). The increased cooling in (2.7) created by moving the shortwave heating to (2.10) is partially offset by an increase in $\rho\overline{w'h'}_B$. Note that the cloud top falls rapidly both as the sea surface temperature falls and as the divergence rises. The initial rise in cloud top against a rise in divergence can be explained by the fact that the system is very far from balance initially.

Cloud base behaves in such a way that the thickness of the cloud varies little between the four experiments.

Figure 3.7 presents the cloud-top mass entrainment. For a given divergence, the entrainment is directly related to the slope in cloud

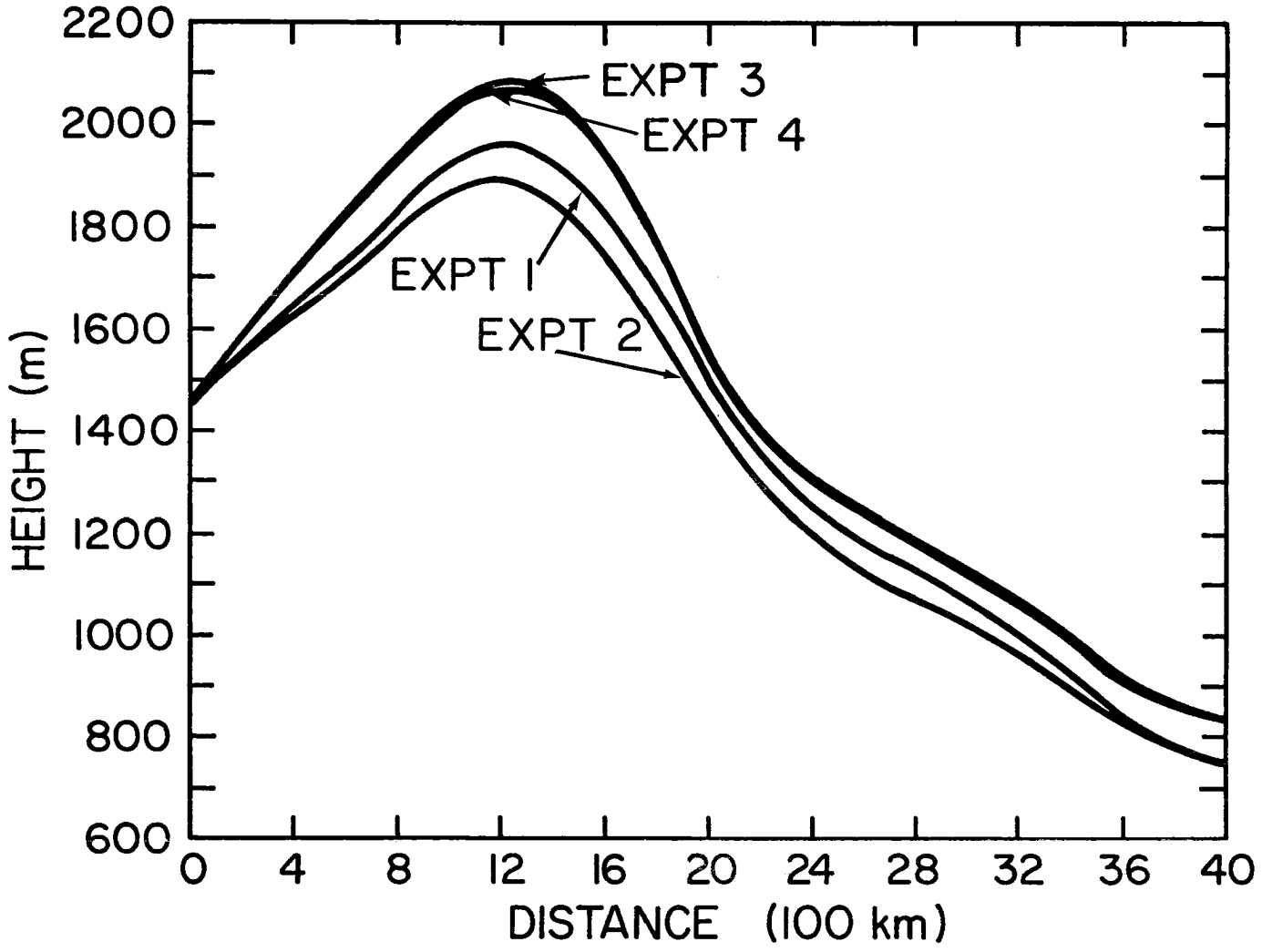

Figure 3.6a. Results of experiments 1-4: cloud top height.

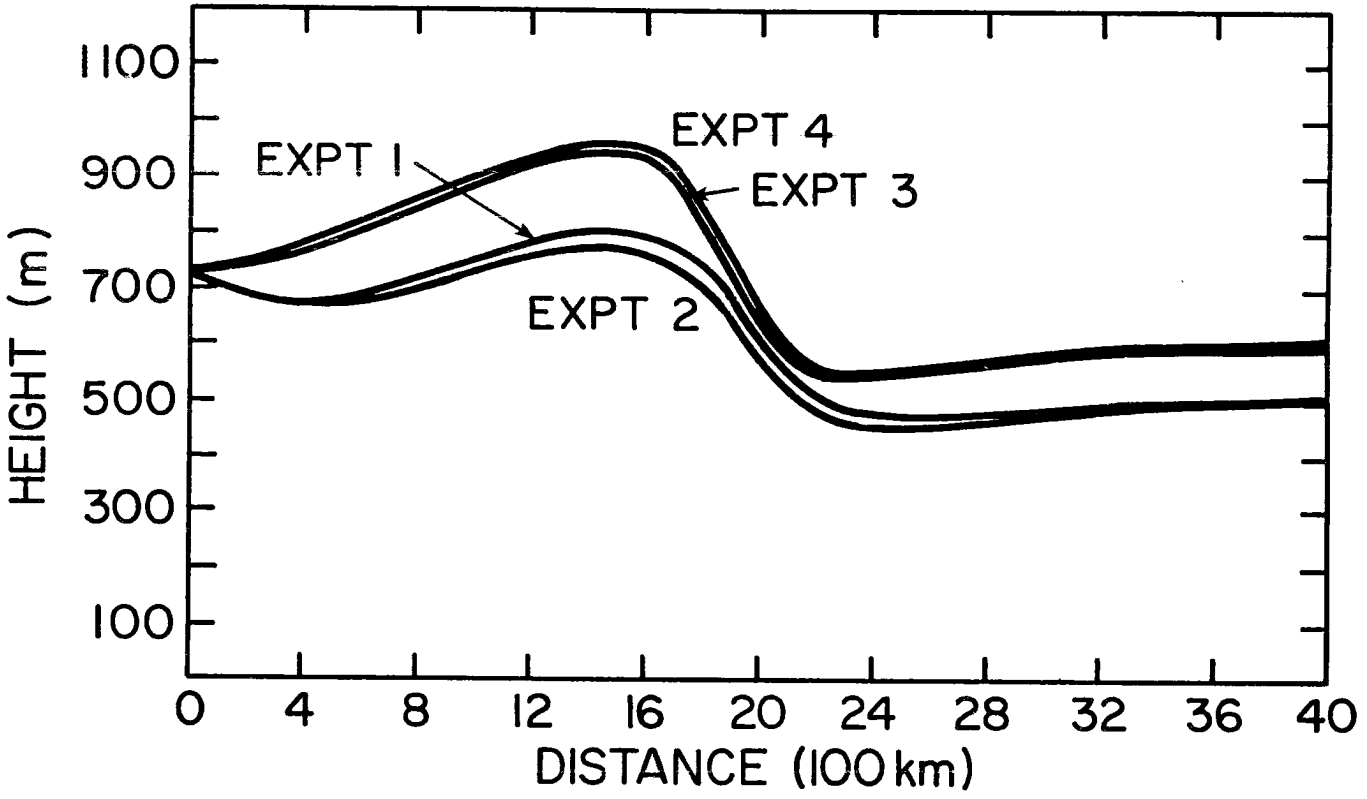

Figure 3.6b. Results of experiments 1-4: cloud base height.

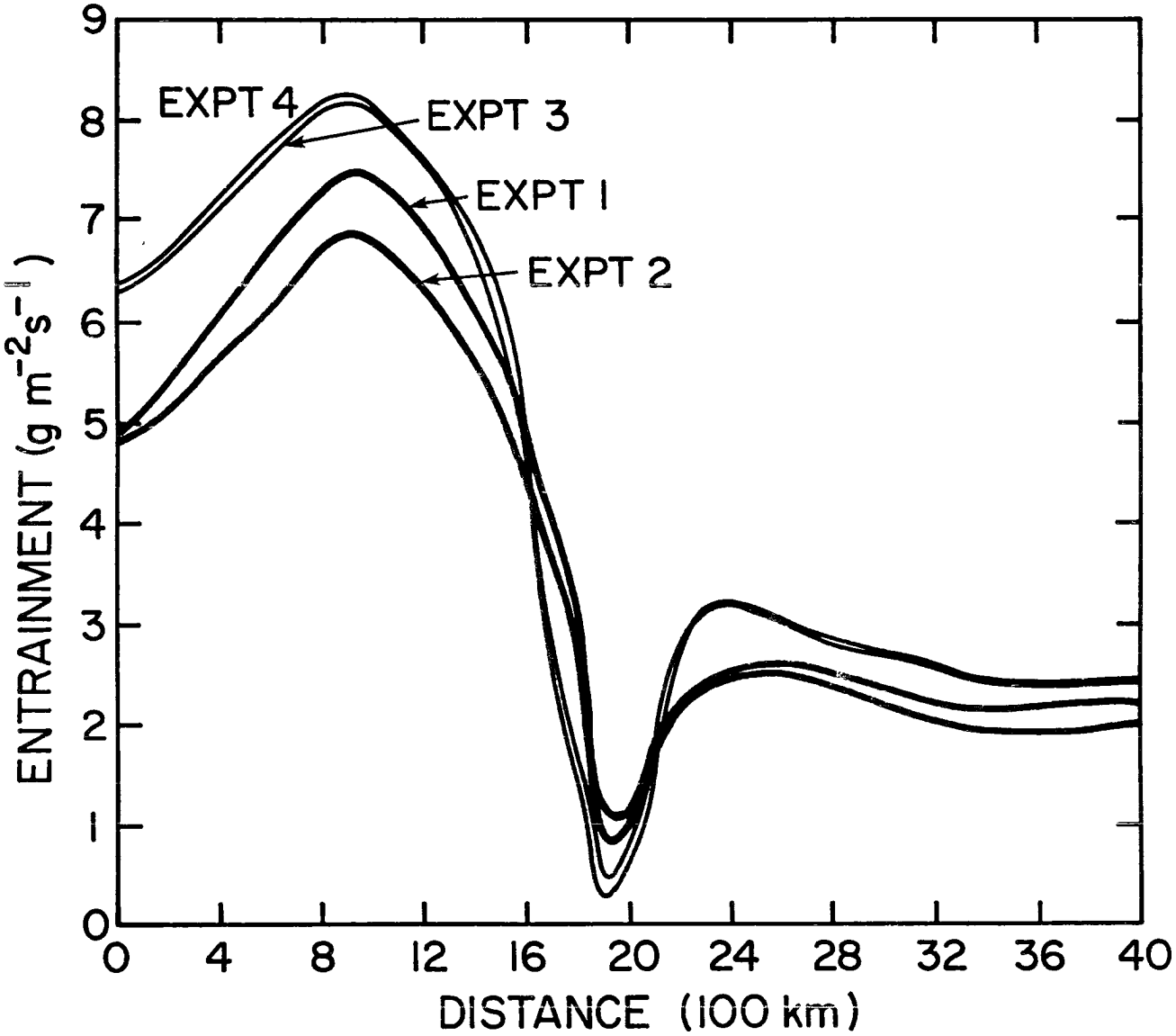

Figure 3.7. Results of experiments 1-4: entrainment at cloud top.

top height. Thus, entrainment reaches a minimum at about 1900 km. Note that when the heating is applied to the mixed layer (experiments 3 and 4), the entrainment is higher at all times but those when the air flow is over colder water, when it is lower than in experiments 1 and 2.

Virtual dry static energy fluxes for experiments 2 and 3 are shown in Figures 3.8a and 3.8b, respectively. It may be seen that as the entrainment approaches zero, so does the difference between the fluxes of virtual dry static energy just above and just below cloud base.

The minimum flux is found just below cloud base except during the period when the air is flowing over colder water, when the minimum is at the surface. For $\rho\overline{w's_v'}_{C-}$ to be positive the average flux of moist static energy must be greater than or nearly equal to the average water flux in the layer. When a parcel of air flows over colder water, the latent and sensitive heat fluxes both drop, which results in a larger drop in $\rho\overline{w'h'}_S$ than $\rho\overline{w'q'}_S$. In addition to this, a drop in $\rho\overline{w'(q'+\ell')}_B$ is associated with the drop in cloud top, with the net result that the s_v flux just below cloud base becomes positive. With shortwave heating applied to the mixed layer, the increased cooling leads to an increase in the cloud-top flux of moist static energy, and $\rho\overline{w's_v'}_{C-}$ is raised accordingly.

A perhaps unexpected result of these tests is that the mixed layer moist static energy is affected very little by the change in location of shortwave heating. Equation (2.10) indicates that, except when the moist static energy fluxes are close to a state of

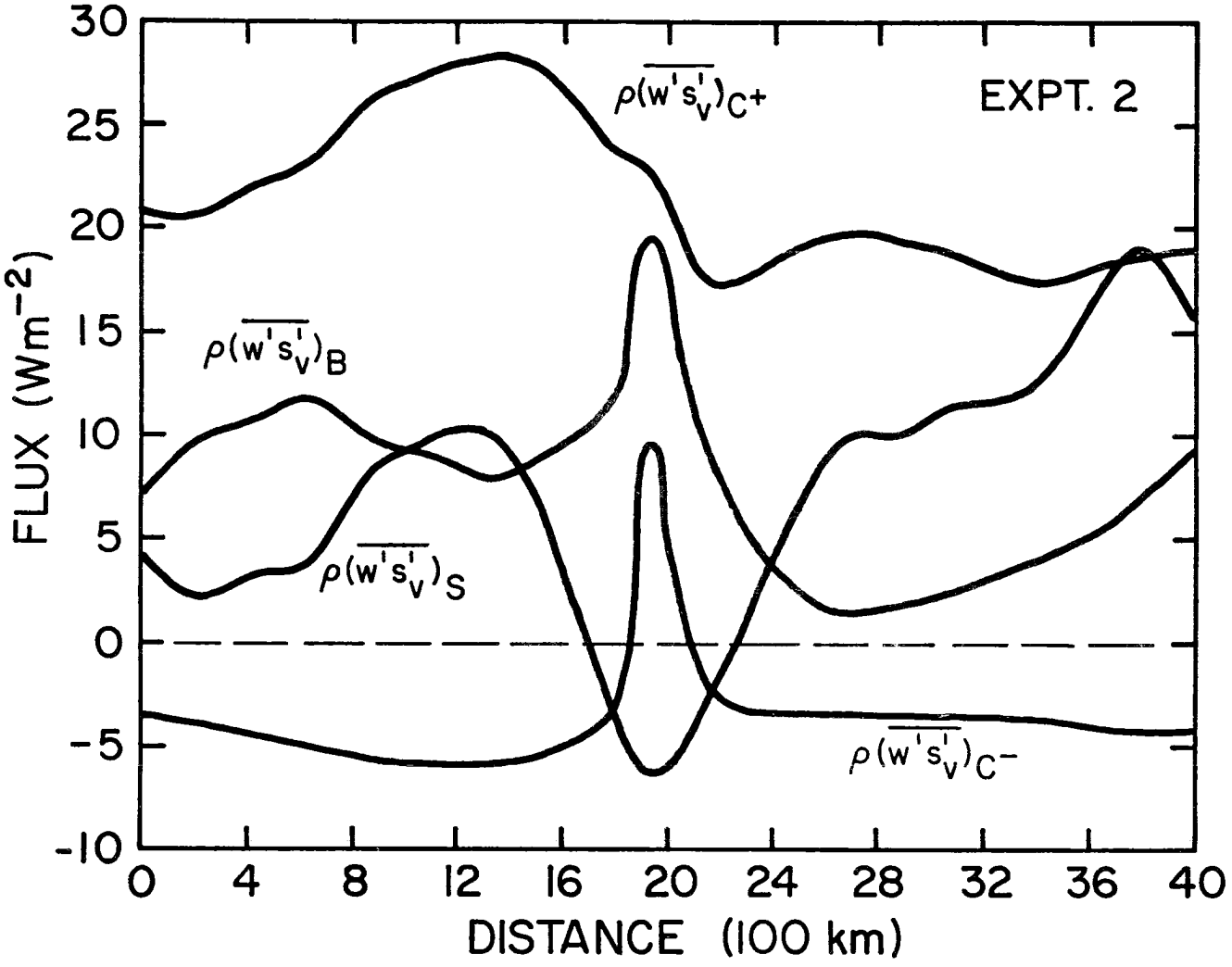

Figure 3.8a. Virtual dry static energy fluxes from experiment 2.

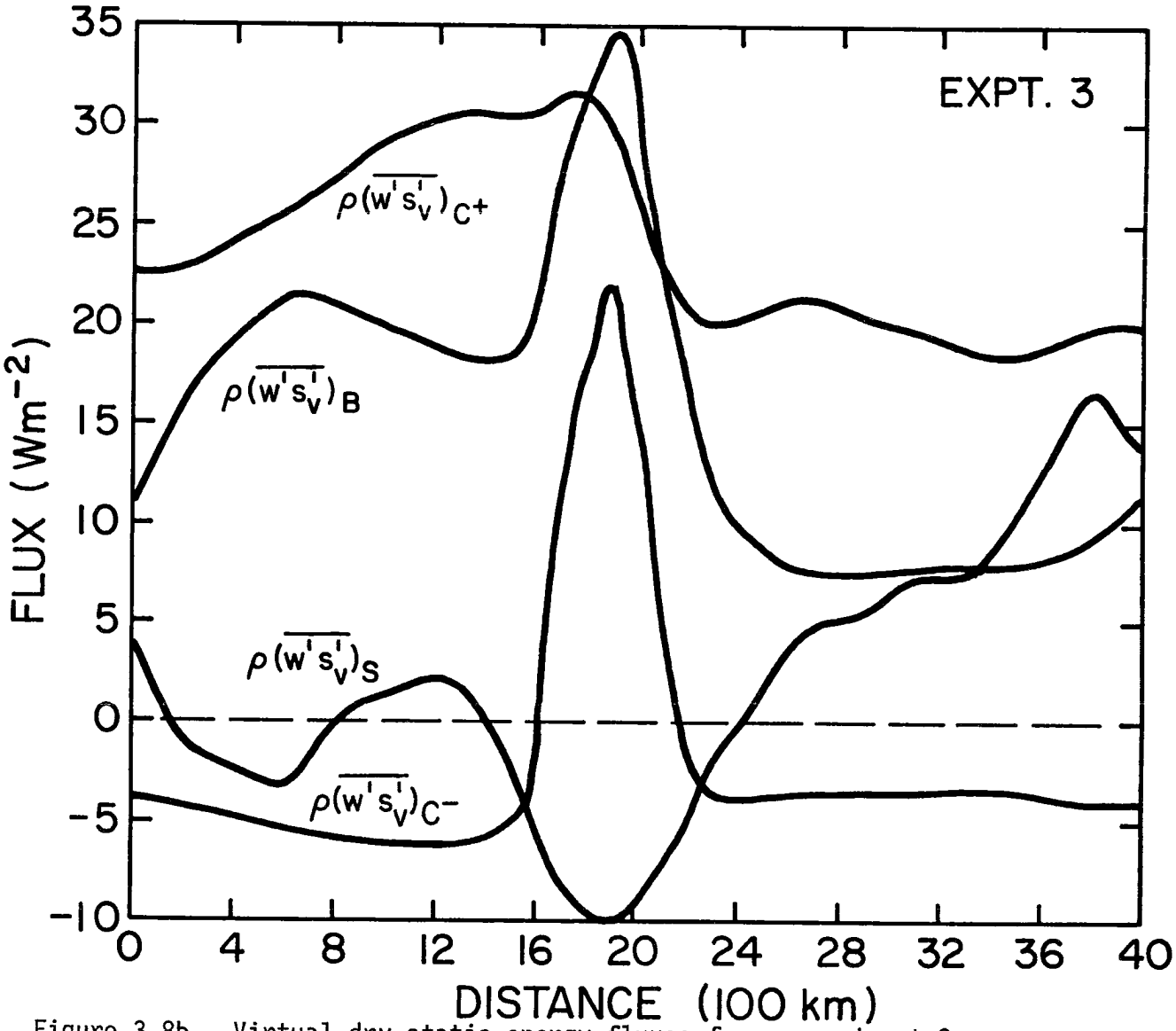

Figure 3.8b. Virtual dry static energy fluxes from experiment 3.

balance, the effect of the addition of the shortwave heating is not large. Such a balance occurs only after long periods of time under slowly varying conditions. Even then, the feedback through the model is such that h_M adjusts to the change in radiation.

3.3.2 Diurnal variation

Schubert (1976) tested his model's response to a diurnal cycle of shortwave radiative flux. His results showed the mixed layer becoming more shallow during the daylight hours, in accordance with observations (e.g. Neiburger et al. (1961) and Kraus (1963)). The variation in the height of cloud base, however, showed that it, too, lowered during the day, with the net result that the cloud thickness increased, leading him to conclude that "apparently, the concept of the sun 'burning off the stratus' is not valid in the present situation."

It was felt that the failure of the model to "burn off" the stratus was indicative of a deficiency in the model's treatment of radiation. Thus, several experiments were run in order to determine how this shortcoming might be remedied. For this purpose, the shortwave radiative flux was made a function of time, in the form

$$\Delta F_S = 2.75\,\overline{\Delta F_S}\,\max\left\{\begin{array}{c}.206 + .794\cos\left(\frac{\pi t}{12} - \pi\right)\\ \\ 0\end{array}\right\}, \qquad (3.5)$$

where t is the time of day in hours and ΔF_S is the mean shortwave absorption (either specified as a constant or calculated using (3.4)). The factor 2.75 in (3.5) is the ratio between the local noon maximum and the daily average. (This factor may be determined by integrating

(3.5) over a 24-hour cycle and observing that the result is $24\,\overline{\Delta F_S}$.) At t = 5 and t = 19 the shortwave absorption is zero, corresponding to sunrise and sunset.

The model was integrated using the fourth-order Runge-Kutta Scheme with a time step of 12 minutes (5 km at 6.94 m s^{-1}). Sea surface temperature was specified as 18.9°C and the entrainment parameter k was set at 0.2. Free-air values of h, q, T, and $F_L^{\downarrow}$ were as will be specified in Chapter 4, assuming a latitude of 30°N.

The experiments that were run are summarized in Table 3.4. Only those numbered will be illustrated, and the numbers correspond to those used in the previous tests. It can be seen that all combinations of form and location of longwave and shortwave radiation were tried. In addition, experiments were done with 70% of the shortwave absorption in the mixed layer and 30% at cloud top (in accordance with the results of Davis et al. (1978) that the majority of the shortwave heating occurs in the upper third of the cloud), and with the heating increased by a factor $z_B/(z_B - z_C)$, which simulates the heating rate in the cloud if all shortwave were absorbed in the cloud. This was an attempt to simulate the effect of adding a distinct cloud layer in the h equation.

In each experiment, the convection was allowed to reach a steady state, and then time was allowed to move forward. The experiments were initialized in the morning or in the evening at the time when the shortwave absorption equalled the 24-hour average value. It was found that the cycle became nearly repetitive after six days of integration, and that the final results were independent of initialization time.

Table 3.4. Summary of the experiments with diurnally-varying shortwave absorption.

Experiment Number	Longwave Emissivity	Shortwave Absorption		Large-Scale Divergence
1	1.0	22.3	T[‡]	$3.8 \times 10^{-6} s^{-1}$
	1.0	22.3	T	2.5
1a	1.0	22.3	T	1.5
	1.0	22.3	T	1.0
	1.0	$f(z_B - z_C)$[‡‡]	T	3.8
2	1.0	22.3	M[‡‡]	3.8
	1.0	$f(z_B - z_C)$	M	3.8
	$f(z_B - z_C)$[†]	22.3	T	2.5
	$f(z_B - z_C)$	$f(z_B - z_C)$	T	3.8
	$f(z_B - z_C)$	$f(z_B - z_C)$	T	1.0
	$f(z_B - z_C)$	22.3	M	2.5
3	$f(z_B - z_C)$	$f(z_B - z_C)$	M	3.8
	$f(z_B - z_C)$	$f(z_B - z_C)$	M	2.5
3a	$f(z_B - z_C)$	$f(z_B - z_C)$	M	1.5
	$f(z_B - z_C)$	$f(z_B - z_C)$	M	1.0
	$f(z_B - z_C)$	$f(z_B - z_C)$	70%M	3.8
	$f(z_B - z_C)$	$f(z_B - z_C)$	70%M	1.0
	$f(z_B - z_C)$	$\frac{z_B f(z_B - z_C)}{z_B - z_C}$	M	3.8
	$f(z_B - z_C)$	$\frac{z_B f(z_B - z_C)}{z_B - z_C}$	M	1.0

[†] equation (3.1)

[‡‡] equation (3.4)

[‡] shortwave applied at cloud top

[‡‡] shortwave applied in mixed layer

The results of experiment 1 are shown in Figure 3.9. This is the Schubert et al. (1978a) method, and can be compared approximately to the diurnal results of Schubert (1976). (The difference is that in this case, the properties of the mixed layer influence the radiative fluxes.) The obvious characteristic of this formulation is that the cloud thickens during the day and becomes thinner at night. Comparing this to experiment 2 (Figure 3.10), it can be seen that in the latter, where the shortwave radiation heats the mixed layer, the cloud thickness diminishes as the sun rises and does not begin to increase until after noon.

Direct comparison of experiments 1 and 2 is made in Figure 3.11, where cloud base height and cloud thickness from the two experiments are illustrated. In experiment 1, where the shortwave warms the cloud top, the rising sun decreases cooling at the top and therefore leads to a decrease in the cloud-top turbulent fluxes of moist static energy and water. This leads to a condition in which the surface fluxes are larger than the cloud-top fluxes, and the mixed layer warms and moistens. As a result, the cloud base drops rapidly. This is not the case, however, when shortwave heating occurs within the mixed layer. Here, the radiative cooling stays nearly constant, while the mixed layer warms but does not moisten. The increase in h_M due to increased temperature allows the cloud-top flux to remain nearly constant, while the flux of water drops as in experiment 1. Thus, the cloud base rises initially as the air warms, but then falls when the moistening becomes sufficient to overcome the shortwave warming.

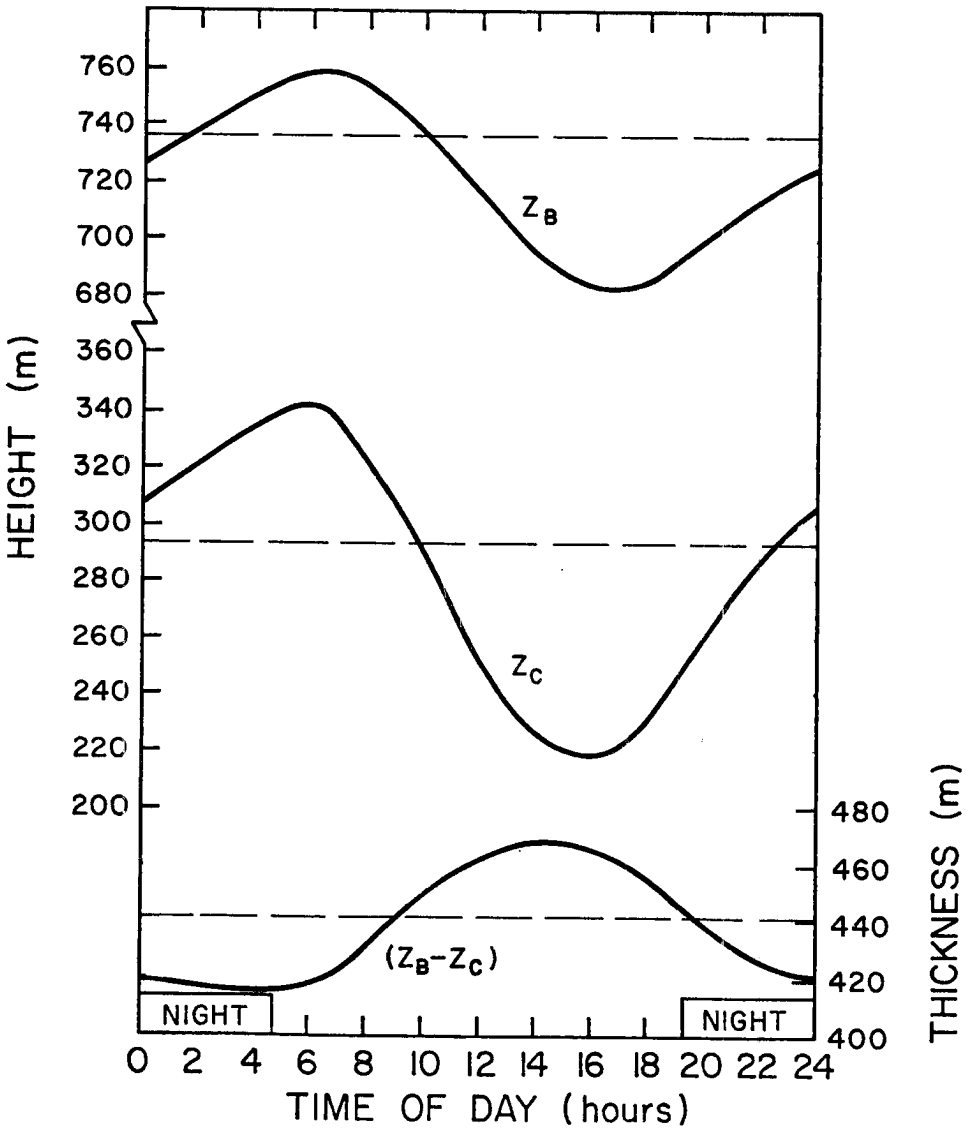

Figure 3.9. Cloud top height, cloud base height, and cloud thickness from experiment 1 of Table 3.4. Steady state values are indicated by horizontal dashed lines.

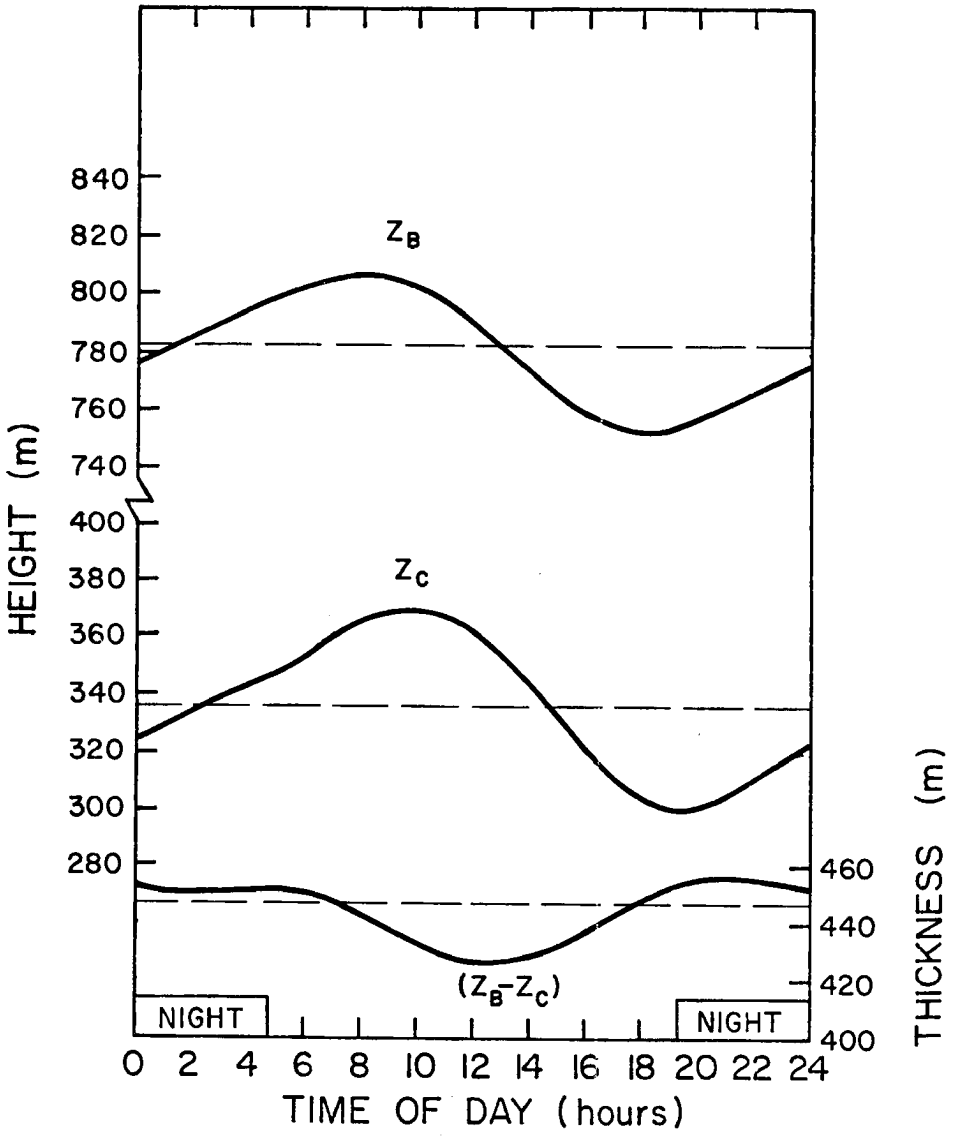

Figure 3.10. Cloud top height, cloud base height, and cloud thickness from experiment 2.

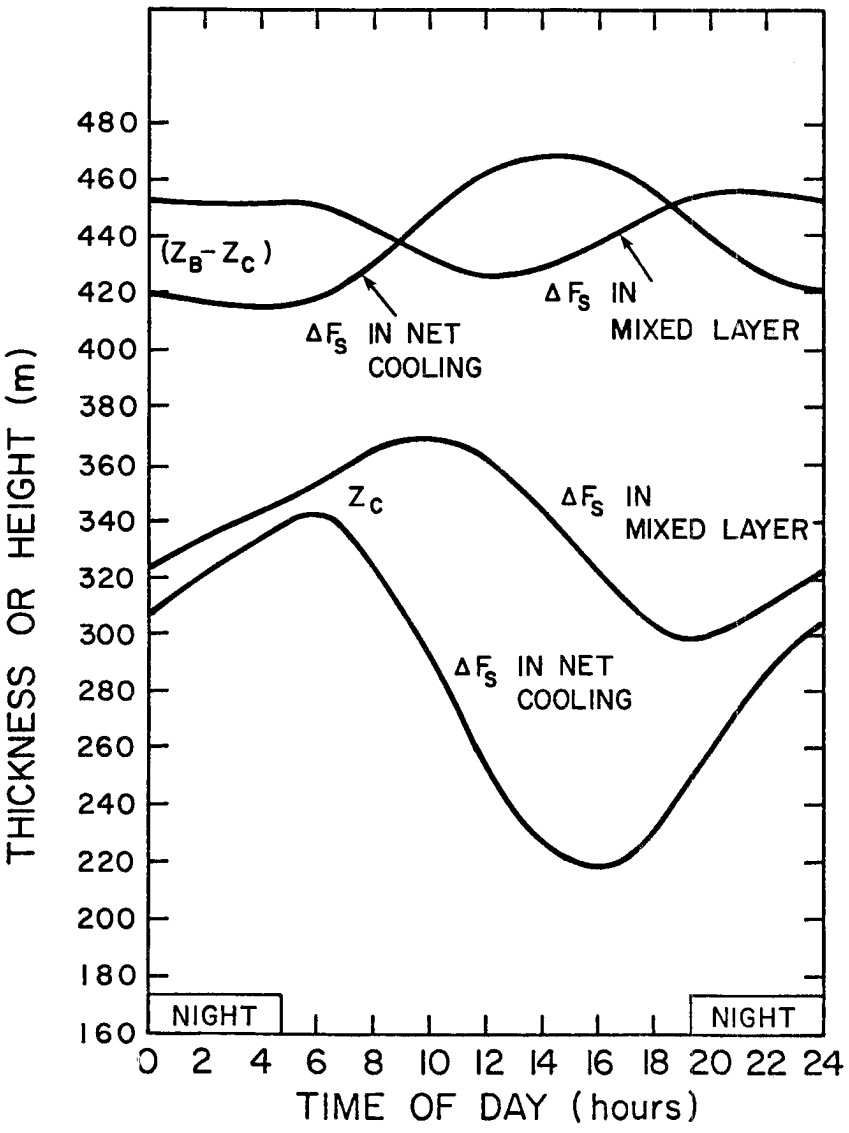

Figure 3.11. Comparison of results of experiments 1 and 2.

The net effect of applying the shortwave heating to the mixed layer as opposed to the cloud top is that of changing the sign of the impulse it imparts to the cloud base height. At the top of the mixed layer, its initial effect is to lower the cloud base and therefore thicken the cloud. When the shortwave heats the mixed layer, it acts to raise the cloud base height initially, and correspondingly makes the cloud thinner.

Figure 3.12 illustrates the results of experiment 3. The cloud in this case was thin enough that the shortwave absorption was not large, reaching a maximum of 35 W m^{-2} (about 2/3 ΔF_L) at noon. This explains the small oscillation evidenced in this case.

In light of the low amplitude of the diurnal response of experiment 3, it was decided to run the same experiment with a small divergence. Since the cloud top height is roughly inversely proportional to the large-scale divergence (Schubert, 1976), the effect of lowering the divergence is to raise the cloud top height and, accordingly, the cloud thickness (cloud base is not nearly as divergence-dependent as cloud top--see Schubert et al., 1978a). Thus, shortwave heating will be larger and the diurnal response should be significantly more vigorous.

The low divergence case was applied to experiments 1 and 3. It is interesting to note in Figure 3.13a that in the case of fixed radiative parameters, the increased depth of the mixed layer has the effect of damping the diurnal variation in cloud base height and cloud thickness. This is easily understood if the magnitudes of the various fluxes are considered. While all fluxes rise, it is the net flux into

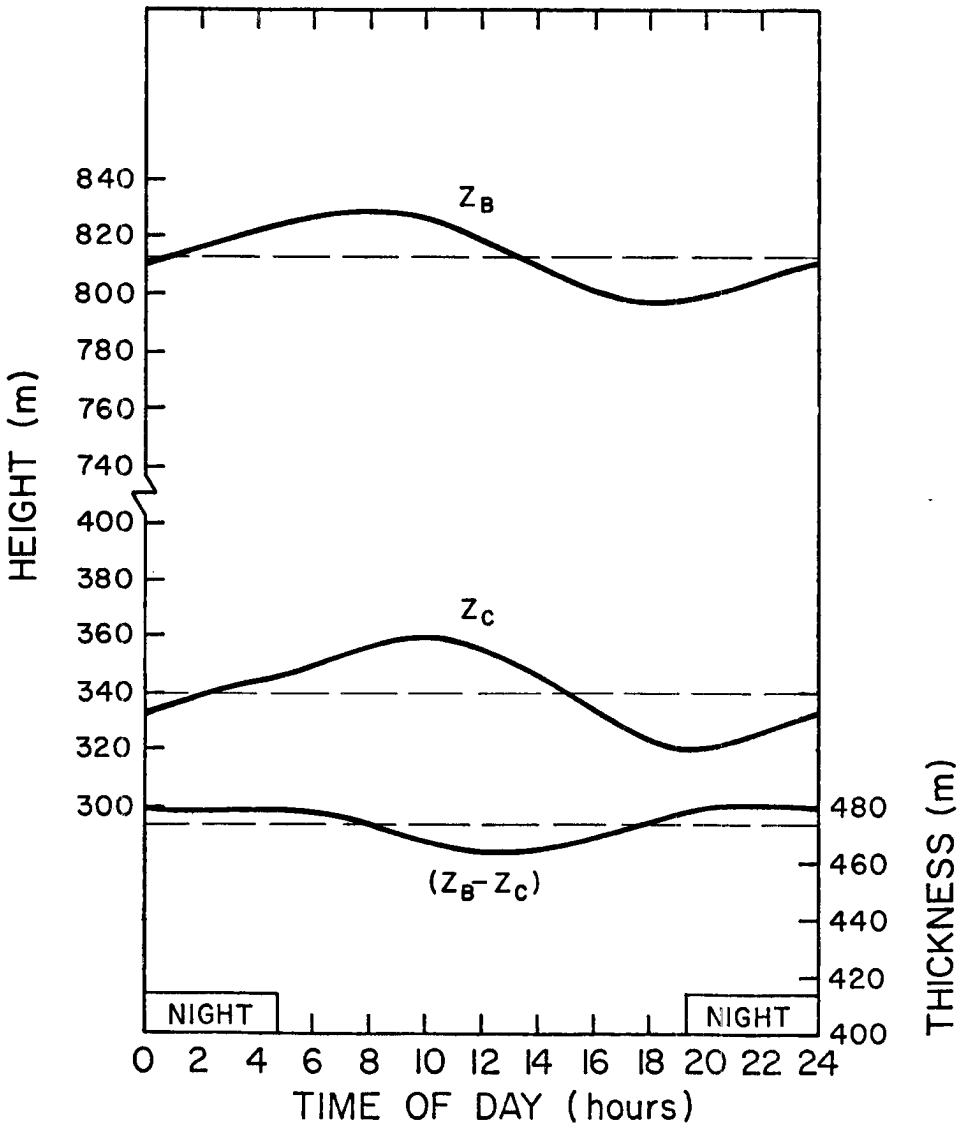

Figure 3.12. Cloud top height, cloud base height, and cloud thickness from experiment 3.

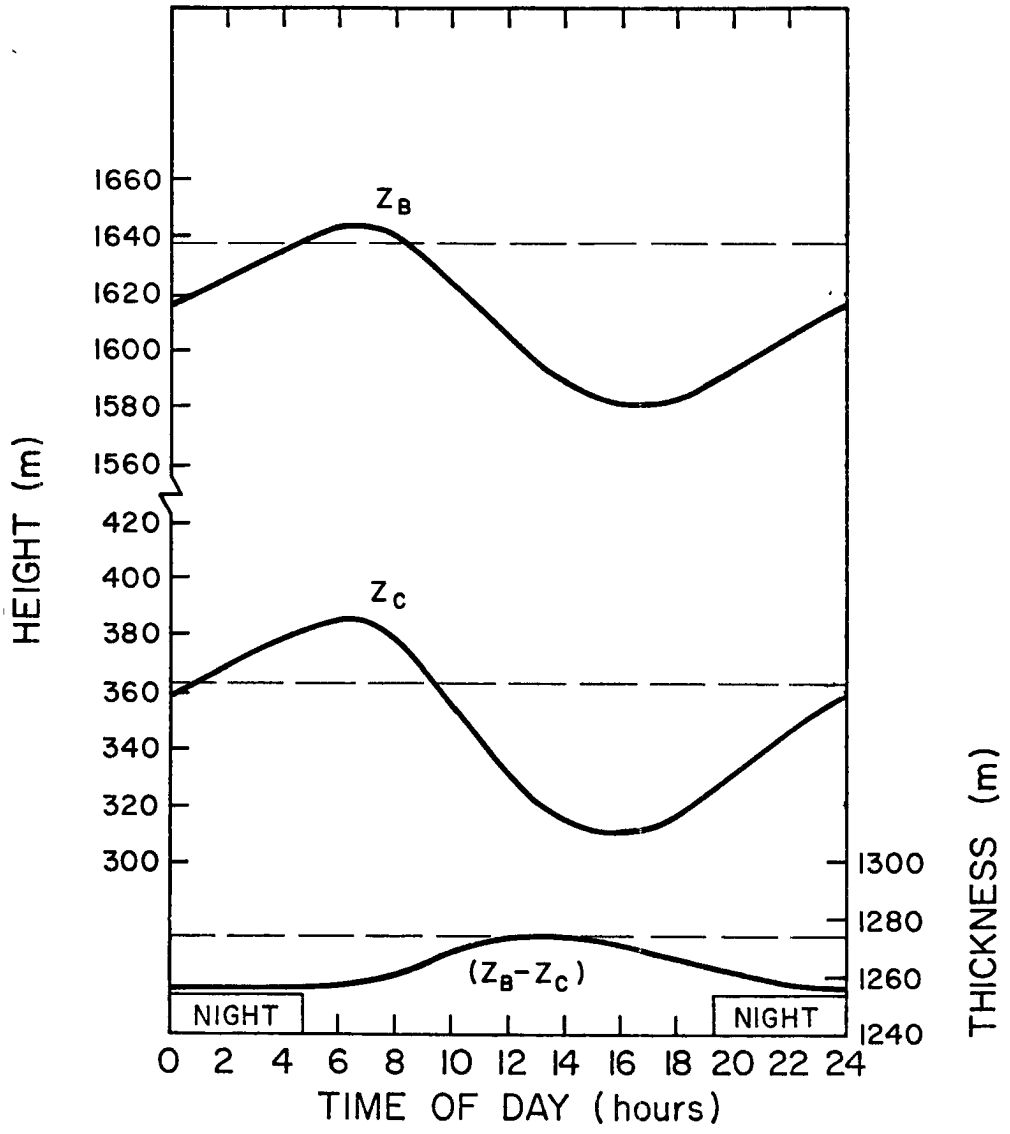

Figure 3.13a. Cloud top height, cloud base height, and cloud thickness from experiment 1a.

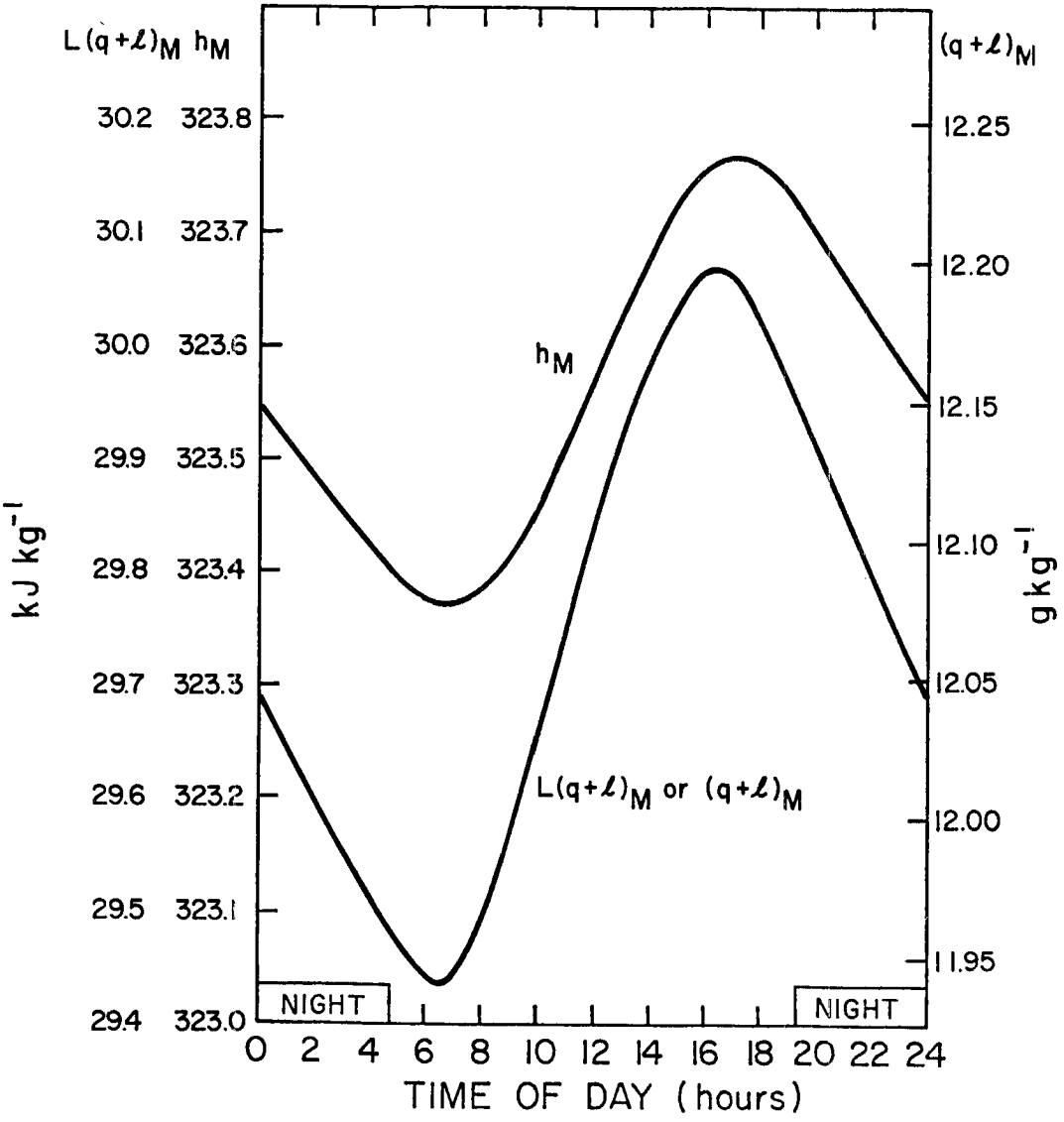

Figure 3.13b. Mixed layer values of moist static energy and total water mixing ratio from experiment 1a.

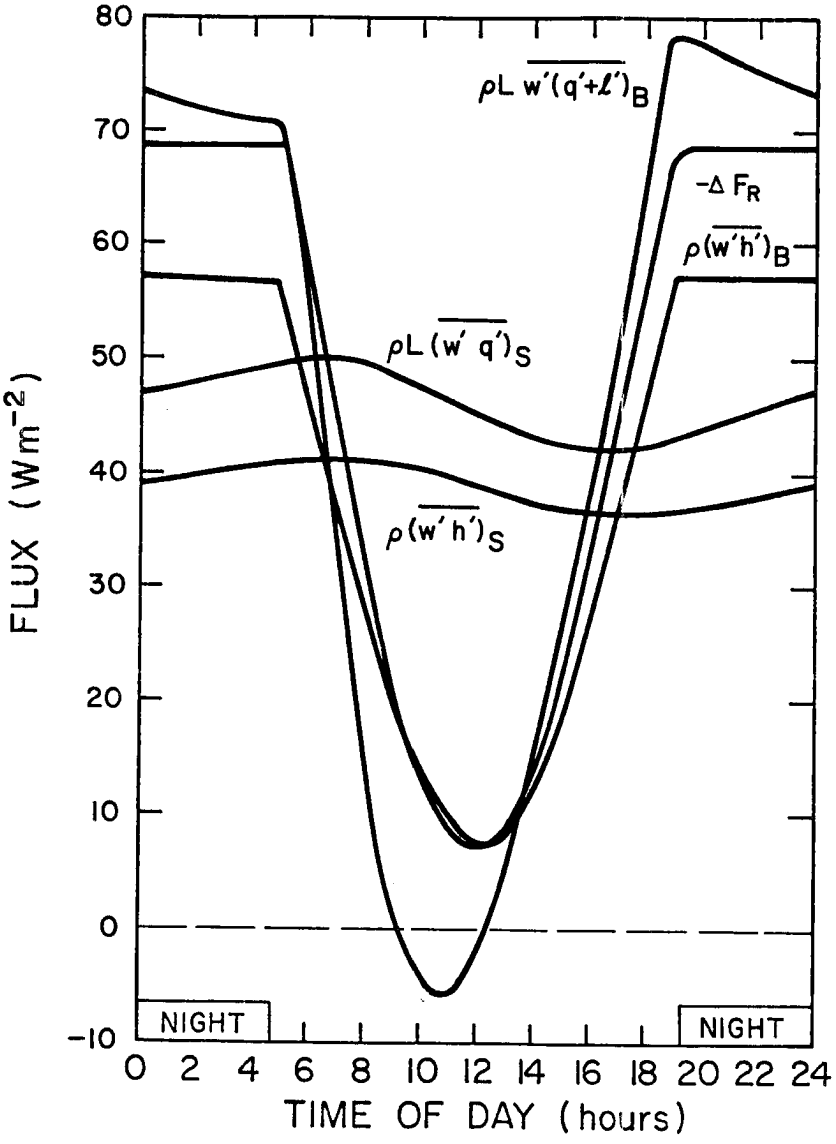

Figure 3.13c. Fluxes of moist static energy, total water, and radiation from experiment 1a.

or out of the mixed layer that governs the changes in cloud base and cloud thickness. While this net change in heat and moisture may be larger in this case than in experiment 1, it follows from the increased depth of the layer that less mean change is taking place, and thus the diurnal response is not as large.

Results of experiment 3a are illustrated in Figure 3.14: Figure 3.14a shows cloud top and cloud base heights and cloud thickness; Figure 3.14b, mixed layer values of moist static energy and total water mixing ratio; and Figure 3.14c, fluxes of h, $(q+\ell)$, and longwave and shortwave radiation.

It can be seen in Figure 3.14a that the objective set forth for this section has been achieved, i.e. the cloud becomes thinner during the day, albeit by a rather small amount. An explanation of the diurnal cycle may be found in Figures 3.14b and 3.14c.

During the night, the surface fluxes of h and $(q+\ell)$ are smaller than the cloud-top fluxes. As a result, the mixed layer is cooling (very slightly) and drying. (The air temperature just above the surface is given simply by the difference $h_M - L(q+\ell)_M$.) At sunrise, the shortwave radiation begins to heat the air, resulting in an increase in the cloud-top h flux and a corresponding decrease in the cloud-top $(q+\ell)$ flux. At about 0630, ΔF_S becomes large enough to overcome the difference between the fluxes of moist static energy, and h_M begins to increase. Mixed layer water content, however, continues to decrease until the cloud top flux becomes smaller than the cloud base flux, at about 0800. Therefore, the layer is warming between 0630 and 0800 and, since the sea surface temperature is

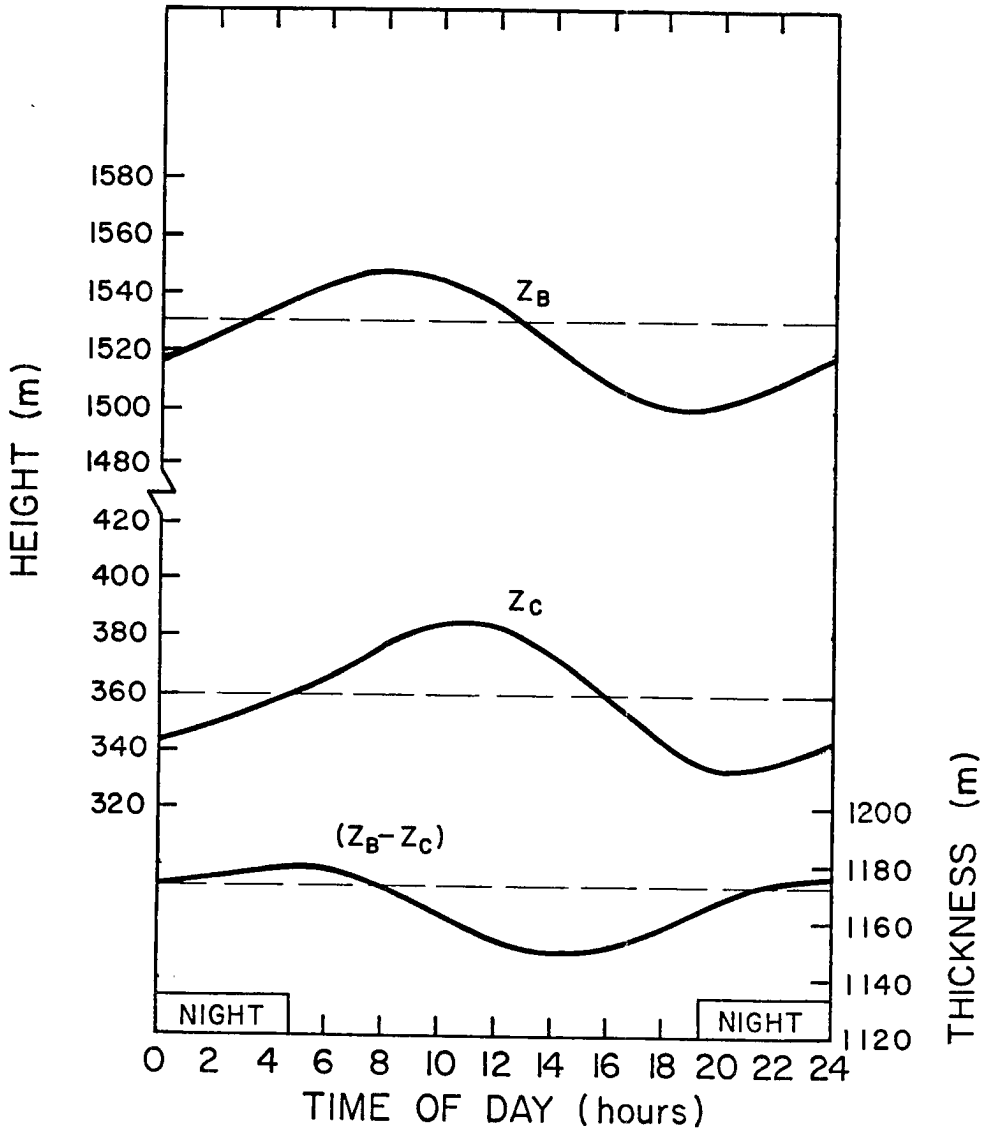

Figure 3.14a. Cloud top height, cloud base height, and cloud thickness from experiment 3a.

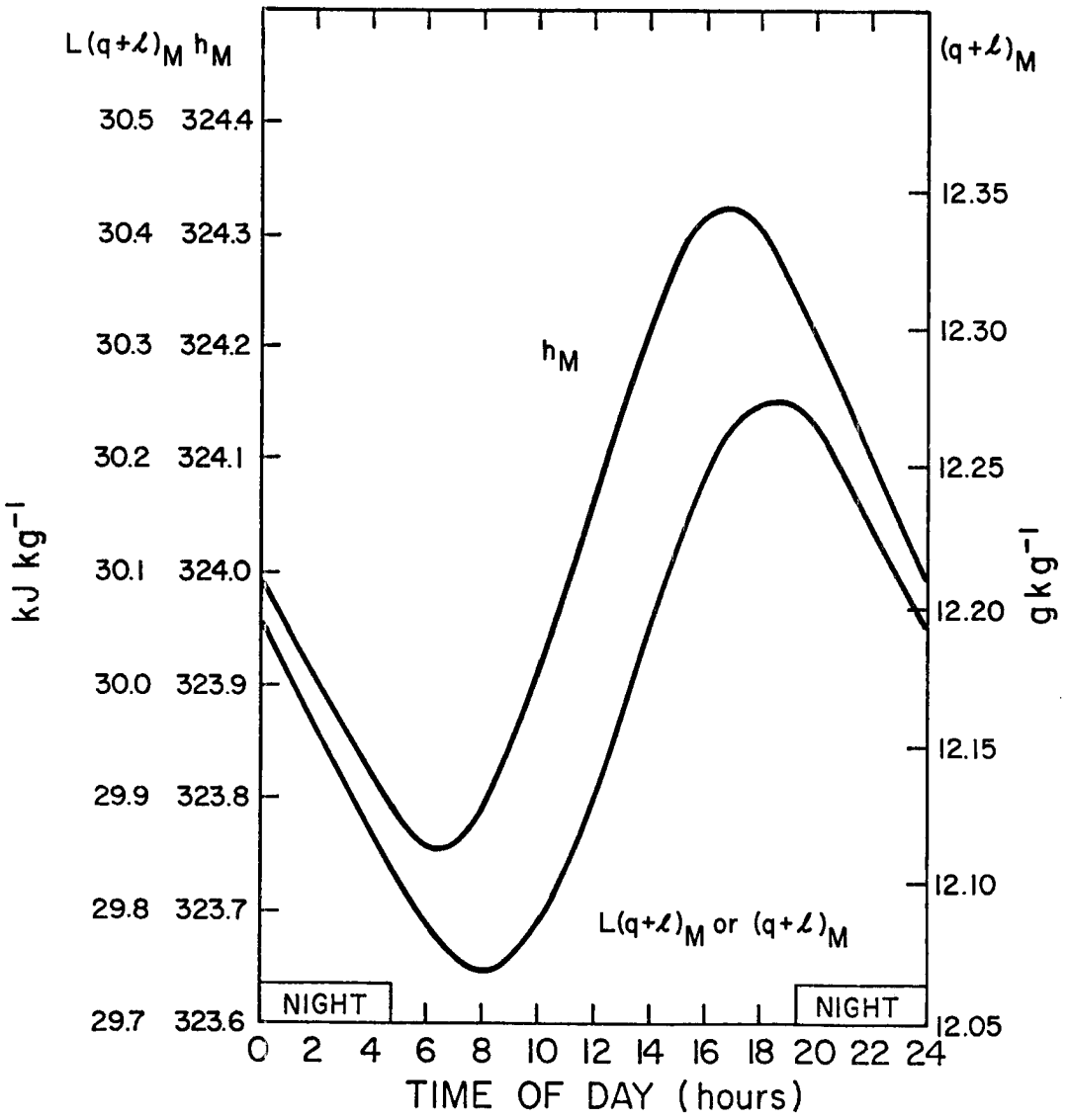

Figure 3.14b. Mixed layer values of moist static energy and total water mixing ratio from experiment 3a.

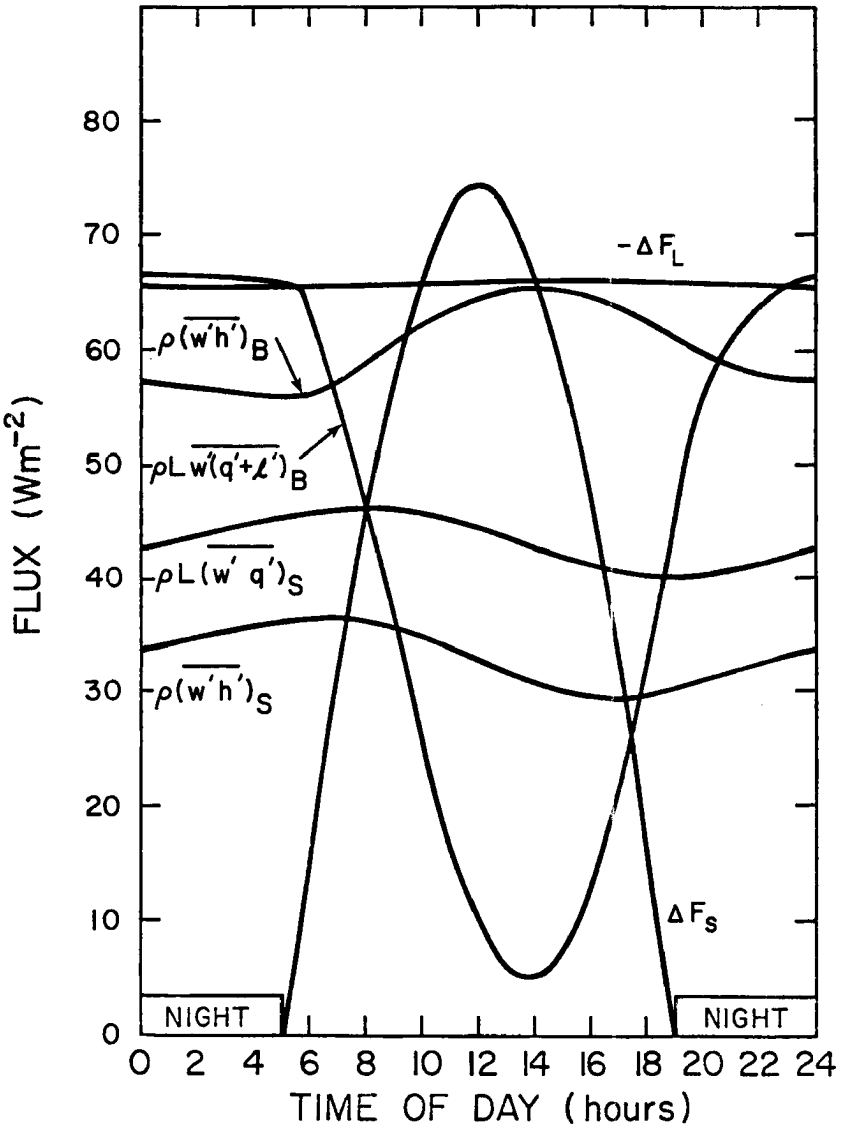

Figure 3.14c. Fluxes of moist static energy, total water, and radiation from experiment 3a.

constant, the surface flux of h diminishes slightly. Surface fluxes continue to shrink as both h_M and $(q+\ell)_M$ rise. The mixed layer exhibits inertia similar to that observed in a diurnal temperature oscillation, as the peaks or valleys in all of the fluxes and in h_M and $(q+\ell)_M$ lag the maximum shortwave heating by two to seven hours (the surface air is warmest between 1230 and 1345, 0.81 degrees warmer than the ocean, while at its coldest, between 2215 and 0215, it is 0.57 degrees warmer than the ocean).

At this point it is interesting to examine the diurnal behavior of experiment 1a, which was shown in Figure 3.13. In particular, note that the surface air is warmest at sunrise (by 0.55 degrees) and cools off during the morning to 0.32 degrees warmer than the (constant) sea surface temperature between 1320 and 1545 (Figure 3.13b). Since the shortwave radiation does not heat the mixed layer, $\rho\overline{w'h'}_B$ does not increase in this case, and the driving radiative cooling decreases considerably during daylight hours (Figure 3.13c), contributing to the general collapse of the mixed layer evident in Figure 3.13a.

While it appears that we have successfully modeled the diurnal behavior of the cloud-topped mixed layer, it may not be the case that we have done so correctly. Observational evidence over the open ocean is lacking, and near the coast, the sea-breeze circulation has been cited in observational studies as the driving mechanism (e.g. Mack et al. (1974) and Neiburger (1944)). Thus, the change in depth of the mixed layer (i.e. cloud top height) may be due to diurnal changes in divergence.

Under the assumption that sea breeze circulations are responsible for the observed diurnal variations in mixed-layer depth, two experiments were run, using the same initial conditions as in experiment 3a. Since winds blow onshore during the day and offshore during the night, the divergence was taken as a sinusoidal oscillation whose maximum occurred at 1600 LT, or about two hours after the maximum land-sea temperature difference. The peak-to-peak amplitude of $4 \times 10^{-6} s^{-1}$, while perhaps inappropriately large for a sea-breeze circulation, was chosen for the reasons outlined below.

In the first experiment (Figure 3.15), the response of the model to the diurnally-varying divergence is shown. It can be seen that the observed variation in cloud top height may be explained by divergence alone, and that the cloud thickness decreases during the day. However, the phase of the thickness oscillation does not appear to be correct, since the cloud continues to evaporate until nearly 2200.

The cloud base height is nearly constant all day. This is not an unexpected response to divergence changes (see Schubert et al., 1978a), but it is in conflict with the diurnal shortwave results presented earlier. Unfortunately, observations of cloud base height are lacking, so this point must remain untested. Diurnal variations of air temperature, however, are almost non-existent, which is not favorable.

If sea-breeze divergence is responsible for the observed diurnal oscillations, one would not expect to see such changes over open ocean. However, Neiburger et al. (1961) report diurnal variations

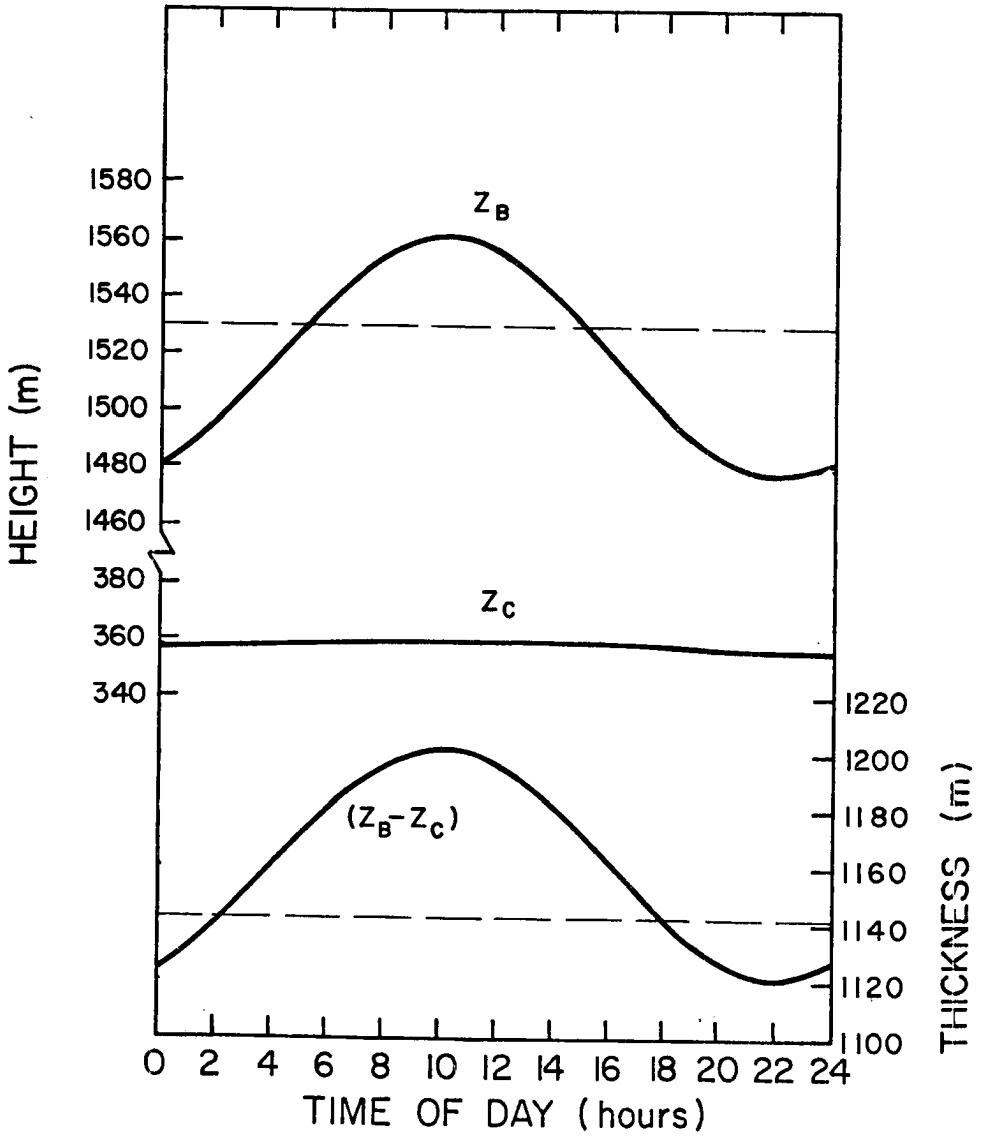

Figure 3.15. Cloud-top height, cloud base height, and cloud thickness for the diurnally-varying divergence experiment. Maximum divergence is at 1600 LT.

of inversion height over the ocean, "even 500 miles from shore." Such oscillations may be due to absorption of shortwave radiation in the mixed layer or to variations in the large-scale divergence field.

Diurnal variations in divergence have been reported over open ocean (e.g. Nitta and Esbensen, 1974), apparently as a compensatory response to diurnal changes in shortwave absorption. Albrecht (1977) suggested that a peak-to-peak divergence amplitude of $4 \times 10^{-6} s^{-1}$ was required to balance the solar radiation above the inversion. In this case, the maximum divergence would be expected to occur around 0400 LT. Results of an experiment with this divergence oscillation would be as in Figure 3.15, but with the phase shifted by about 12 hours. Again, it is probable that shortwave radiative effects must interact directly with the cloud to produce any variations in cloud base height.

Figure 3.16 illustrates the results of experiments involving diurnal variations of both divergence and shortwave radiation. The solid lines are for the sea-breeze case, i.e. maximum divergence at 1600 LT, while the dashed lines are for the case of maximum divergence at 0400 LT. The response of the model atmosphere to the combination of shortwave radiative warming and radiationally-driven divergence seems to be the better of the two.

If both processes are indeed affecting the divergence, the results in Figure 3.16 indicated by dashed lines would correspond to the diurnal variations over open ocean. Since the two processes are about 12 hours out of phase to each other, their combined response, assuming equal amplitudes, approaches zero. Thus Figure 3.14a would apply near the coastline. If the sea-breeze circulation is the only

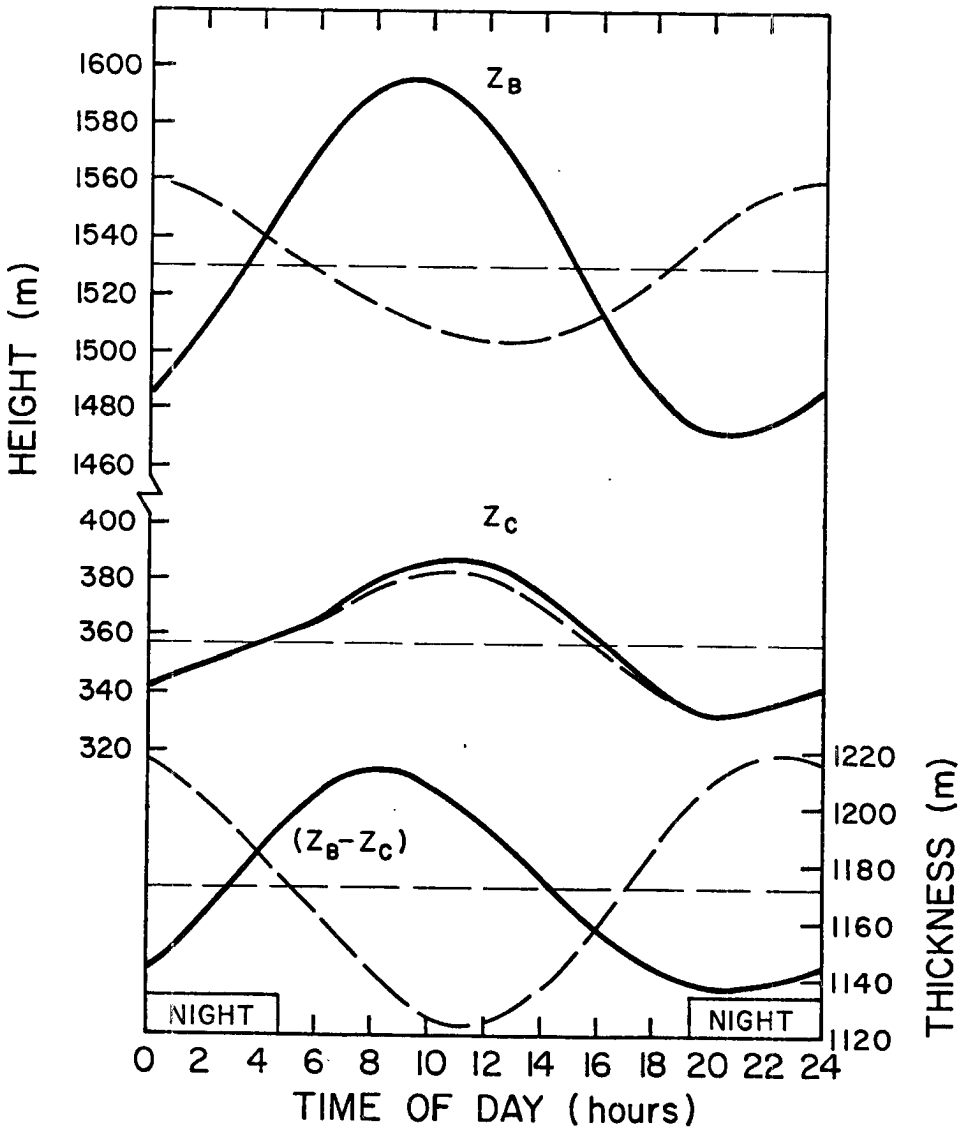

Figure 3.16. Results of the experiments with diurnally-varying divergence and shortwave radiation: maximum divergence at 1600 LT (solid lines); maximum divergence at 0400 LT (dashed lines).

diurnal mechanism affecting divergence, then it might be expected that the solid lines in Figure 3.16 would apply near the coast, and Figure 3.14a over open ocean.

4. Input data and procedure

In this chapter, the initialization of the model will be discussed. Climatological data for July over the eastern North Pacific Ocean are used to determine fields of sea surface temperature, winds, and divergence on a geographical grid. In addition, upper-air data from several stations are combined to produce vertical profiles of water vapor mixing ratio, moist static energy, and downward long-wave radiative flux above the mixed layer. Then, in section 4.3, the experimental procedure will be discussed.

4.1 Input data for the mixed layer

As noted in Table 1.1, the model requires input of sea surface temperature, wind speed, and large-scale divergence. In addition, for the numerical integration as performed here, knowledge of the wind direction is also necessary.

4.1.1 Sea surface temperature

July mean sea surface temperature data were obtained from a compilation by LaViolette and Seim (1969). The data were presented in graphical form, and data on a 2° latitude-longitude grid were picked off. Input for the model was required for the region bounded by 145°W, 115°W, 50°N, and 20°N. The field was extrapolated into those parts of the grid where no data exist. The resulting sea surface temperature field is shown in Figure 4.1.

4.1.2 Wind speed and direction

Mean wind data for July of 1961 through 1974 as presented by Miller and Stevenson (1974) were used as input to the model. Their

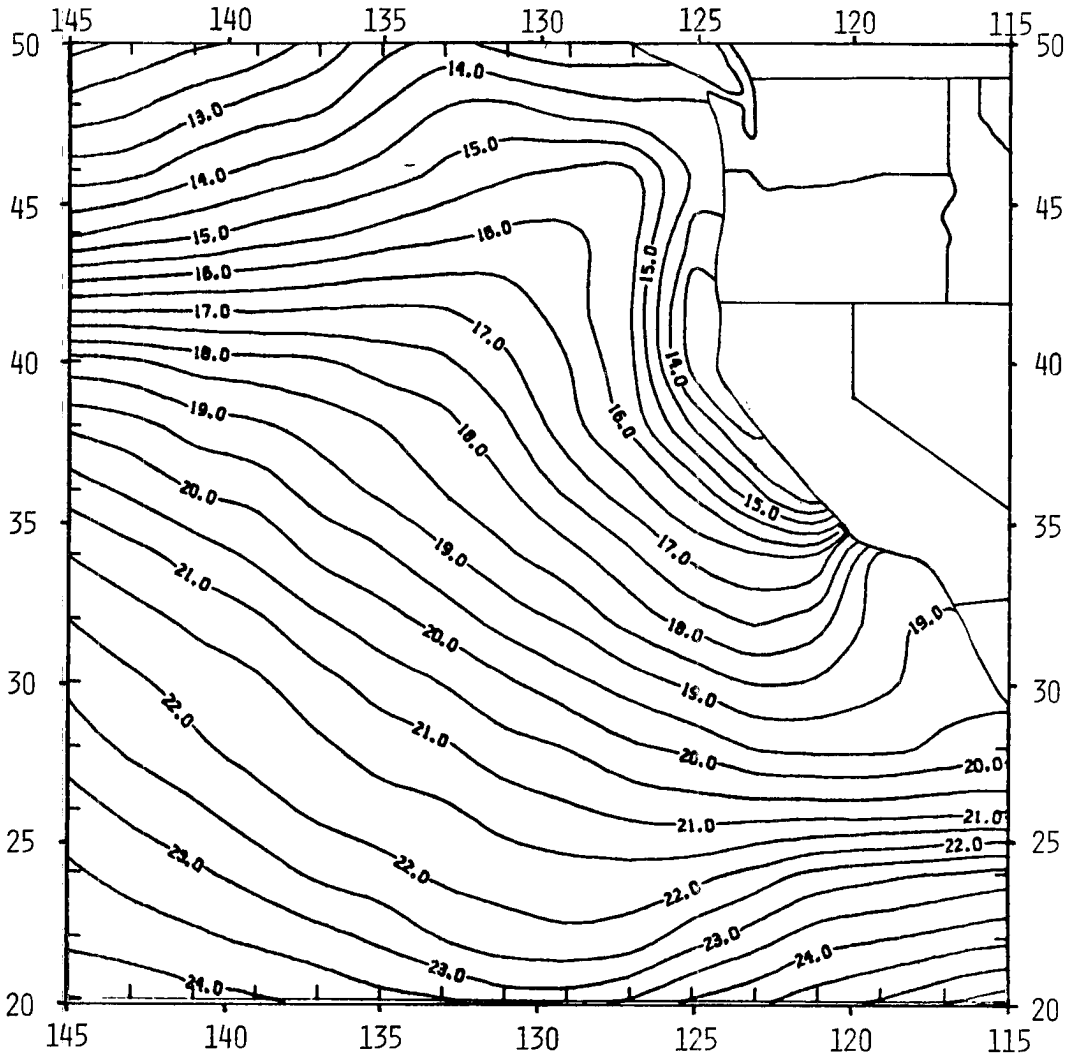

Figure 4.1. Input field of sea surface temperature (°C).

data, shown in Figure 4.2, are given as average values over 5 degree by 5 degree areas. Data presented by Neiburger et al. (1961) display the same qualitative features.

The direction of each arrow in Figure 4.2 was determined with a protractor, and the speed and direction for that box was assigned to the point at its center (e.g. 32.5°N, 142.5°W). The mean winds (using average wind speed) were then decomposed into their u and v components. These mean u and v were then linearly interpolated onto a 2 degree by 2 degree grid bounded by 145°W, 115°W, 50°N, and 20°N. Missing values were extrapolated from the data. The resulting u, v, and V (= $(u^2 + v^2)^{\frac{1}{2}}$) fields are shown in Figure 4.3. Resultant streamlines are also shown in Figure 4.3c.

It should be pointed out here that several sources of error are inherent in this sort of analysis. Perhaps the most significant is that any maxima or minima in the original (Miller and Stevenson) data are considerably smoothed. This smoothing is a result of assigning the mean to the center of each box. If the average in a given box is higher than that of any of the surrounding boxes, then the interpolated value at any point within that box will be less than the center point since a linear interpolation is performed. Thus, the average value in the box will be smaller than the original data. The same will be true in the opposite sense for a local minimum. Therefore, the procedure utilized herein has performed an a priori smoothing on the data. This smoothing should not be considered damaging, however, since the quantitative nature of this study is not rigorous.

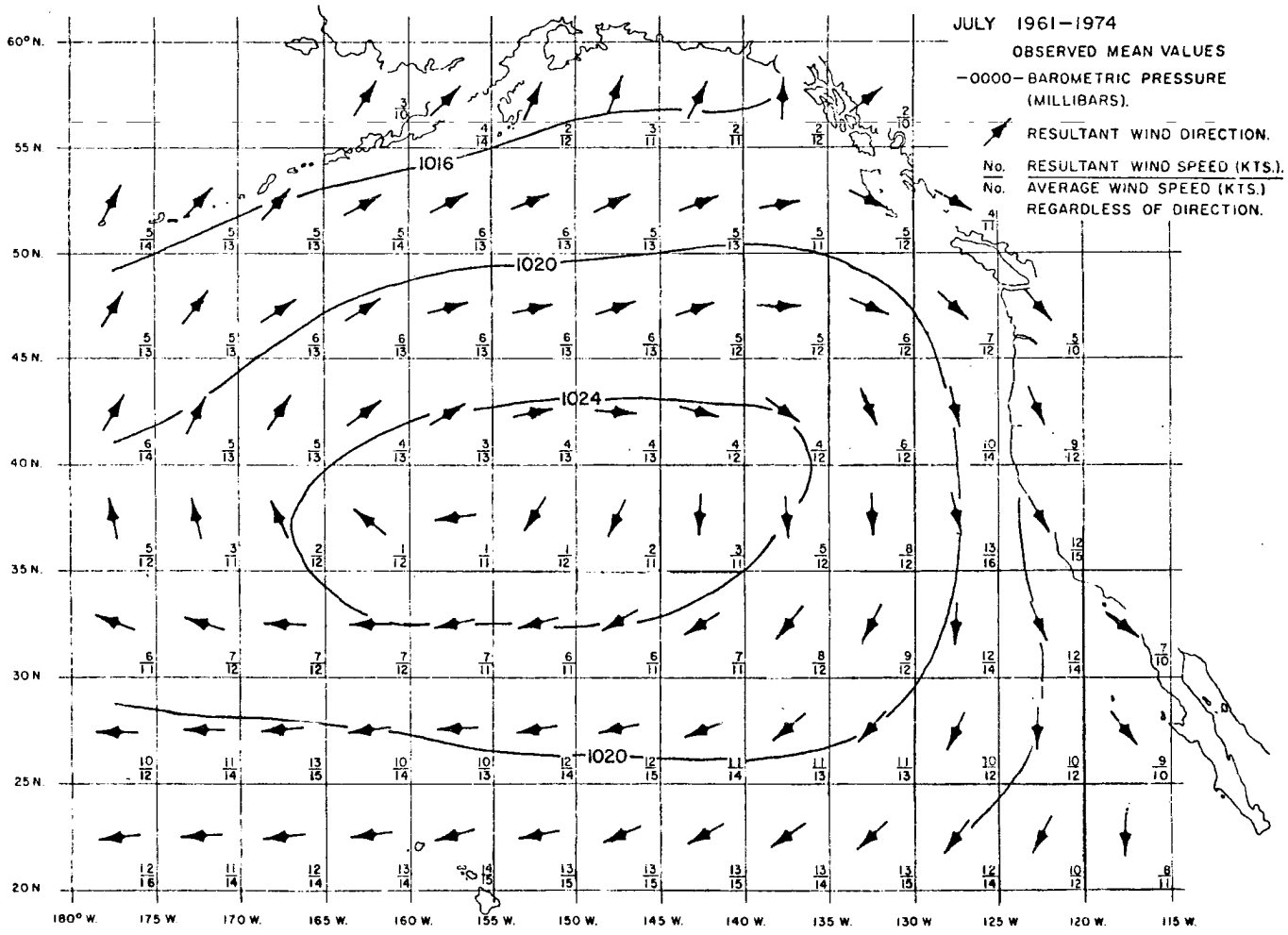

Figure 4.2. Mean July (1961-1974) surface pressure, resultant wind direction and speed, and average wind speed (from Miller and Stevenson, 1974).

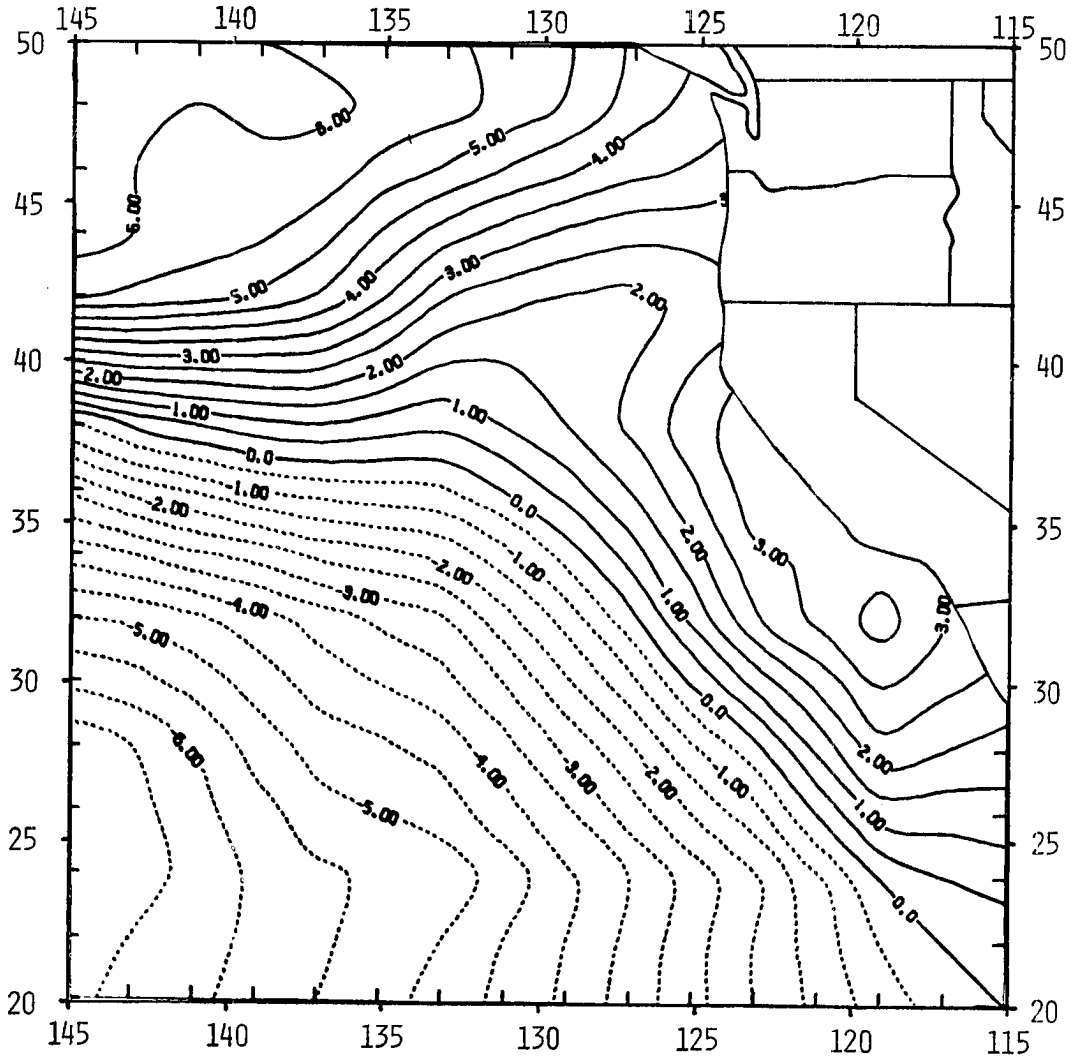

Figure 4.3a. Input field of eastward component of wind, u; (m s^{-1}). Dashed lines in this and subsequent figures indicate negative values.

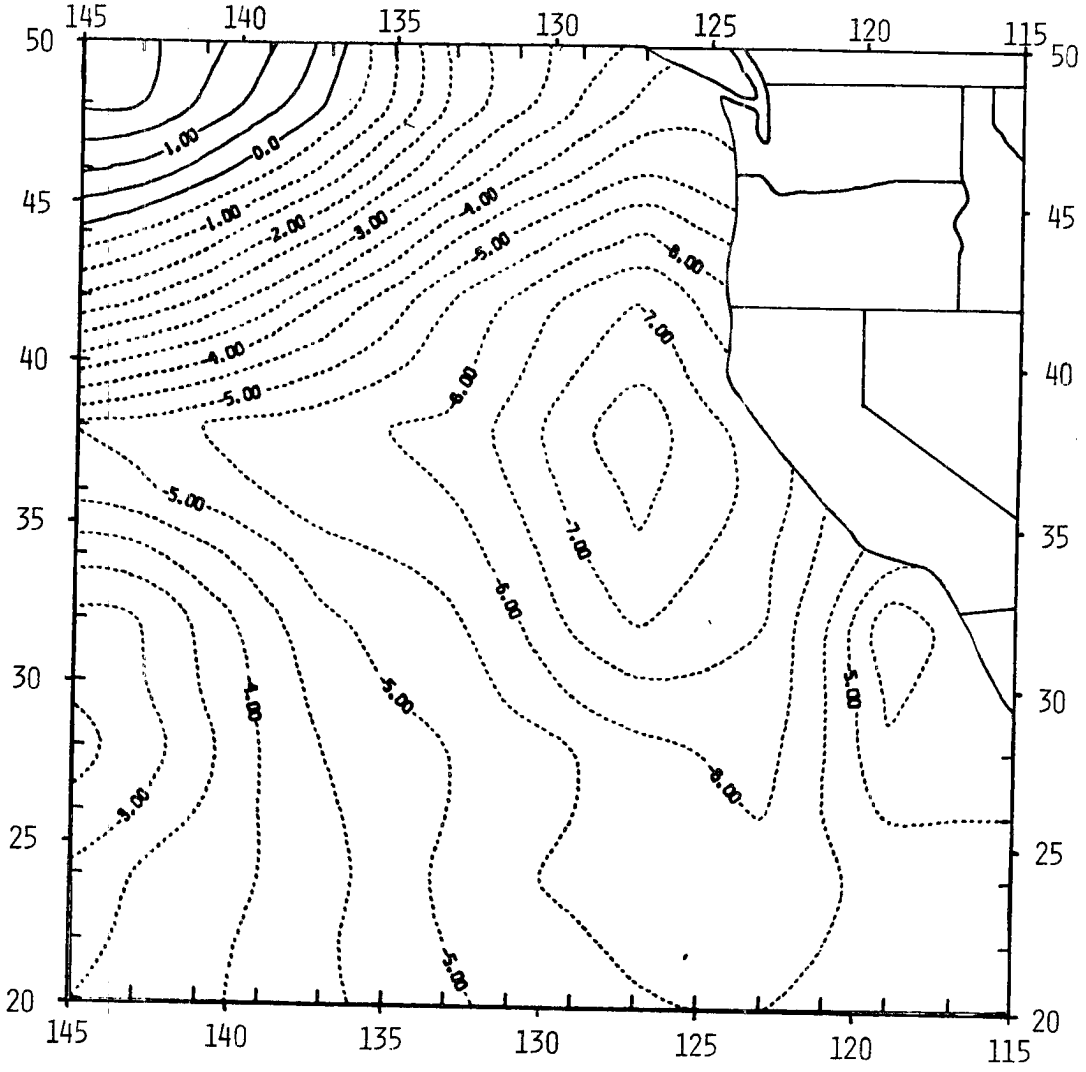

Figure 4.3b. Input field of northward component of wind, v; (m s^{-1}).

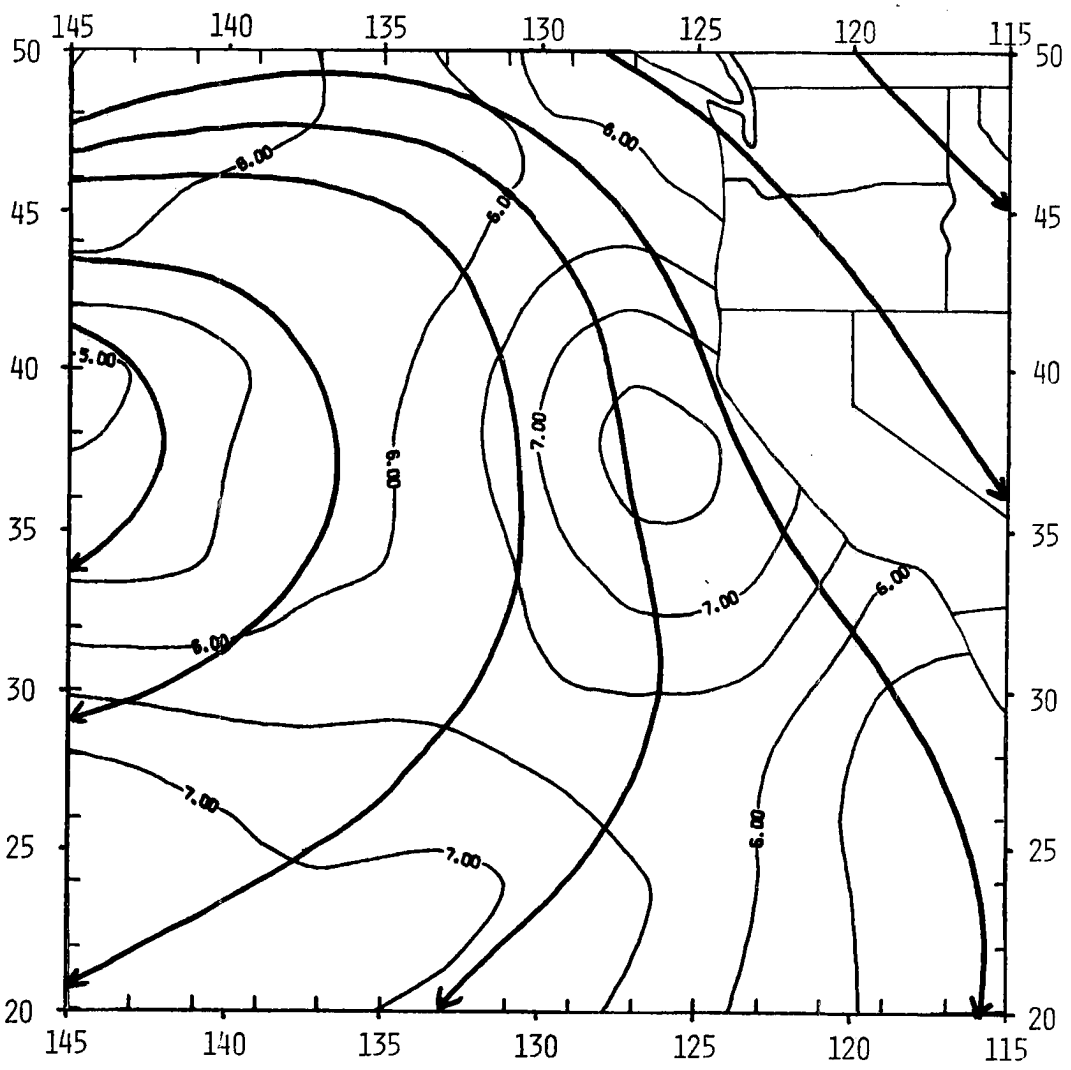

Figure 4.3c. Input field of wind speed, V; (m s^{-1}), and resultant streamlines.

4.1.3 Large-scale divergence

The third large-scale input to the model is the divergence of the horizontal wind. Included in the data of Miller and Stevenson (1974) are resultant wind speeds. These resultant speeds may be used to obtain the mean large-scale divergence over the field. This was done in two ways.

In the first method, the resultant winds were treated in the same manner as the average winds in the previous subsection. That is, they were interpolated and extrapolated onto a 2 degree by 2 degree grid, with the exception that in this case, the boundaries were 147°W, 113°W, 52°N, and 18°N. Divergence was then computed at each of the interior points of this grid, using the winds at the surrounding four points (i.e. $D = \frac{\Delta u}{\Delta x} + \frac{\Delta v}{\Delta y}$). The results of this method are shown in Figure 4.4. Comparison of this field to that observed by Neiburger et al. (1961), (Figure 4.5), shows that this method produces a serious discrepancy between calculated and observed large-scale divergence in the vicinity of southern California and southward along 120°W. The sharp east-west gradient of divergence is apparently not real.

This problem led to the calculation of large-scale divergence using a different method. In this case, the Miller and Stevenson data were employed to compute divergence on the 5 by 5 degree grid, and the resulting values were interpolated and hand-extrapolated onto the 2 by 2 degree grid. The results of this procedure are illustrated in Figure 4.6. The unextrapolated field extended from 141°W to the coastline or 119°W and from 50°N to 28°N. The shape of the southern

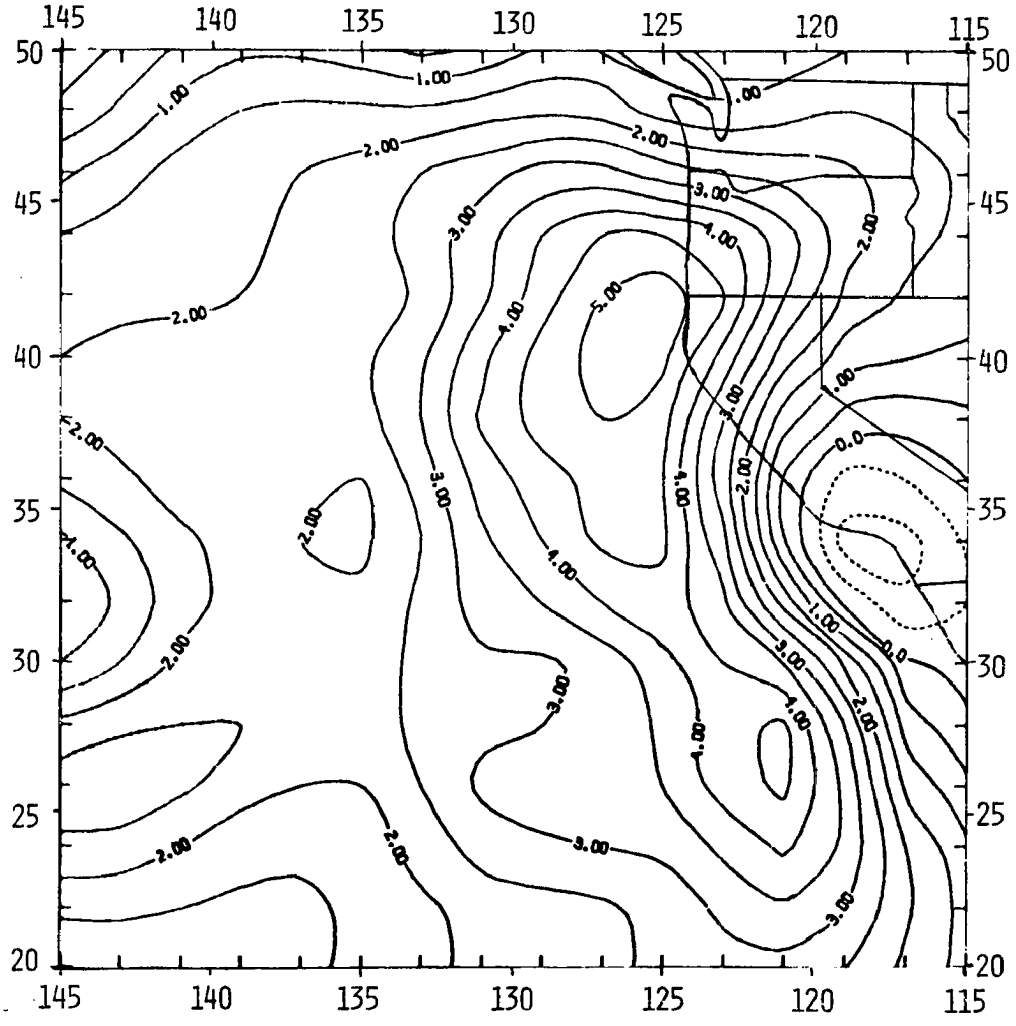

Figure 4.4. Large-scale divergence calculated from Figure 4.3 ($10^{-6}s^{-1}$).

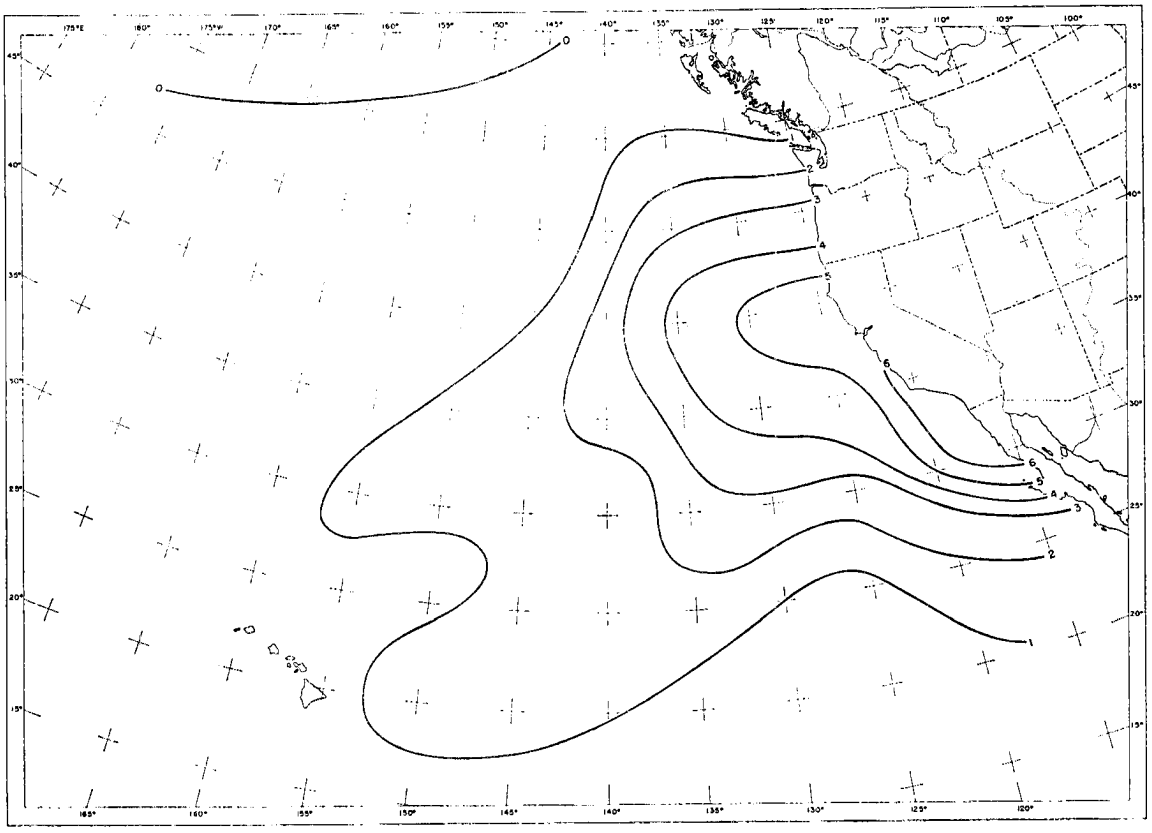

Figure 4.5. Large-scale divergence for July (from Neiburger et al., 1961).

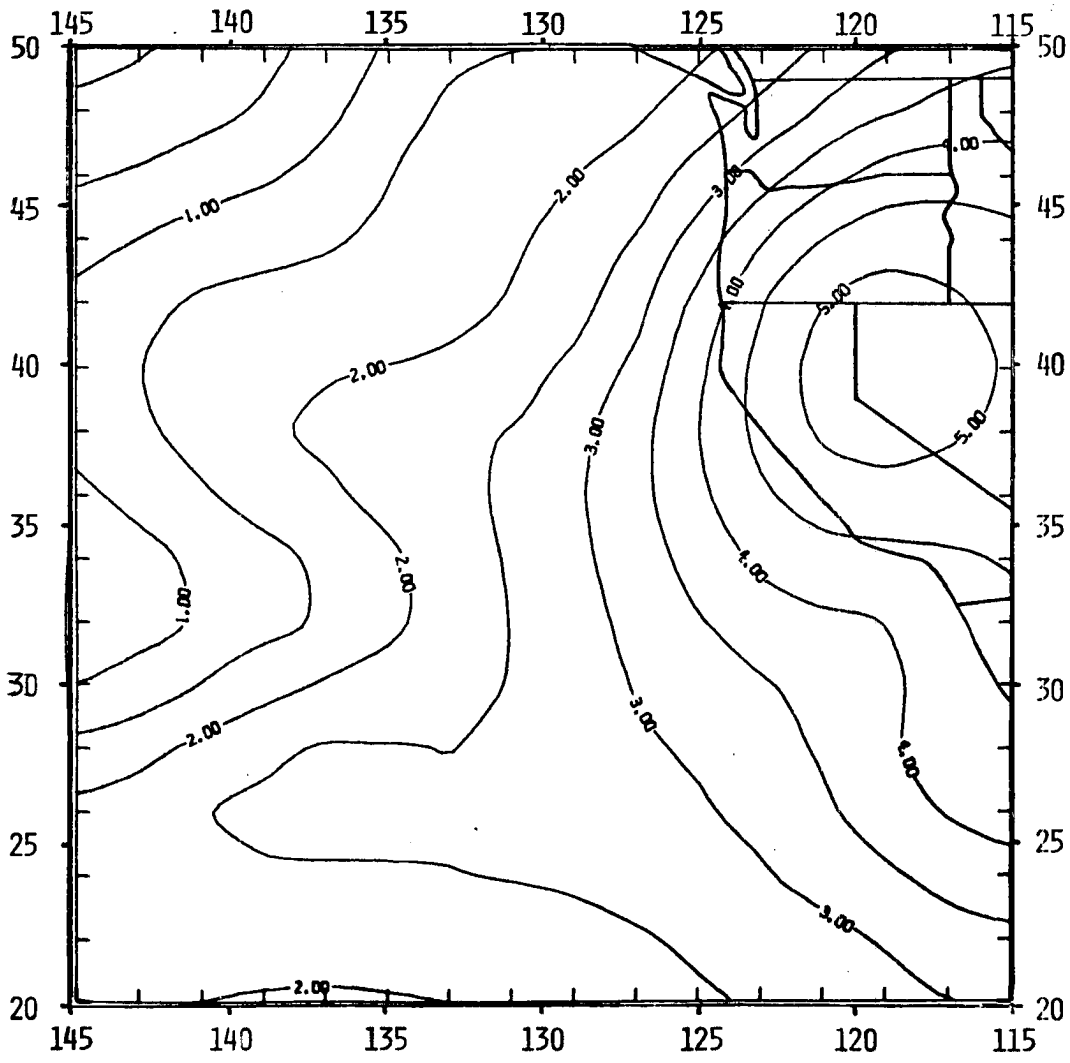

Figure 4.6. Large-scale divergence calculated from Figure 4.2 and interpolated ($10^{-6}s^{-1}$).

quarter of the field was drawn to approximately conform to Figure 4.5, and the maximum over western Nevada is purely hypothetical. Its existence has virtually no effect on the results of the numerical integration, since none of the streamlines passing through it emerge over the ocean.

In this second divergence field the major problems with the first have been eliminated, i.e. the divergence is large over the area south along 120°W and the strong east-west gradient has been removed.

The discussion above illustrates that care must be taken when processing data, since the same data base produced two significantly different divergence fields when analyzed differently. This also illustrates that the results to be presented in the next chapter should be interpreted with caution, since the large-scale divergence field in Figure 4.6, as well as the other inputs already discussed and forthcoming, are only best estimates of the climatological conditions. Day to day variations in these input fields may be quite large.

4.2 Input data above the mixed layer

In order that the cloud-top jumps of water vapor mixing ratio, moist static energy, and longwave radiative flux may be calculated, a knowledge of those three quantities above the mixed layer is required.

Mean atmospheric data for July of 1967 through 1970 were obtained from U. S. Department of Commerce (1967-1970a) for the rawinsonde stations Quillayute, Oakland, and San Diego, and from U. S. Department of Commerce (1967-1970b) for Ship P and Ship N. These data were averaged over the four Julys, resulting in July soundings of temperature and dew point temperature as functions of

height. These data, listed in Table 4.1, were used for each of the three required parameters.

4.2.1 Moist static energy

Water vapor pressure was calculated from the dewpoint temperature data in Table 4.1 by the method of Lowe (1977). Water vapor mixing ratio, q, was then calculated using the atmospheric pressure. These values were then coupled with temperature and height data to produce moist static energy, h.

A linear least squares fit was made to each of the resulting h profiles, using only the data above about 1.5 km. The purpose of this was to eliminate any effects of the boundary layer and inversion that characterize these stations in July. The fit coefficients were, in turn, subjected to a least squares fit as a function of the cosine of the latitude. (Cosine was chosen because it yielded a better representation of the data.) The resulting equation for h as a function of height and latitude is

$$h(z_{B+}) = 242.29 + 94.34 \cos\phi + (4.72 - 3.93 \cos\phi) \times 10^{-3} z_B \quad (\text{kJ kg}^{-1}), \tag{4.1}$$

where ϕ is the latitude and only Ship P, Quillayute, and Oakland were used as inputs to the fitting equation. Equation (4.1), as well as the original data, is plotted in Figure 4.7.

4.2.2 Water vapor mixing ratio

The water vapor mixing ratio data obtained from the mean soundings were fit by functions of height and latitude. The resulting

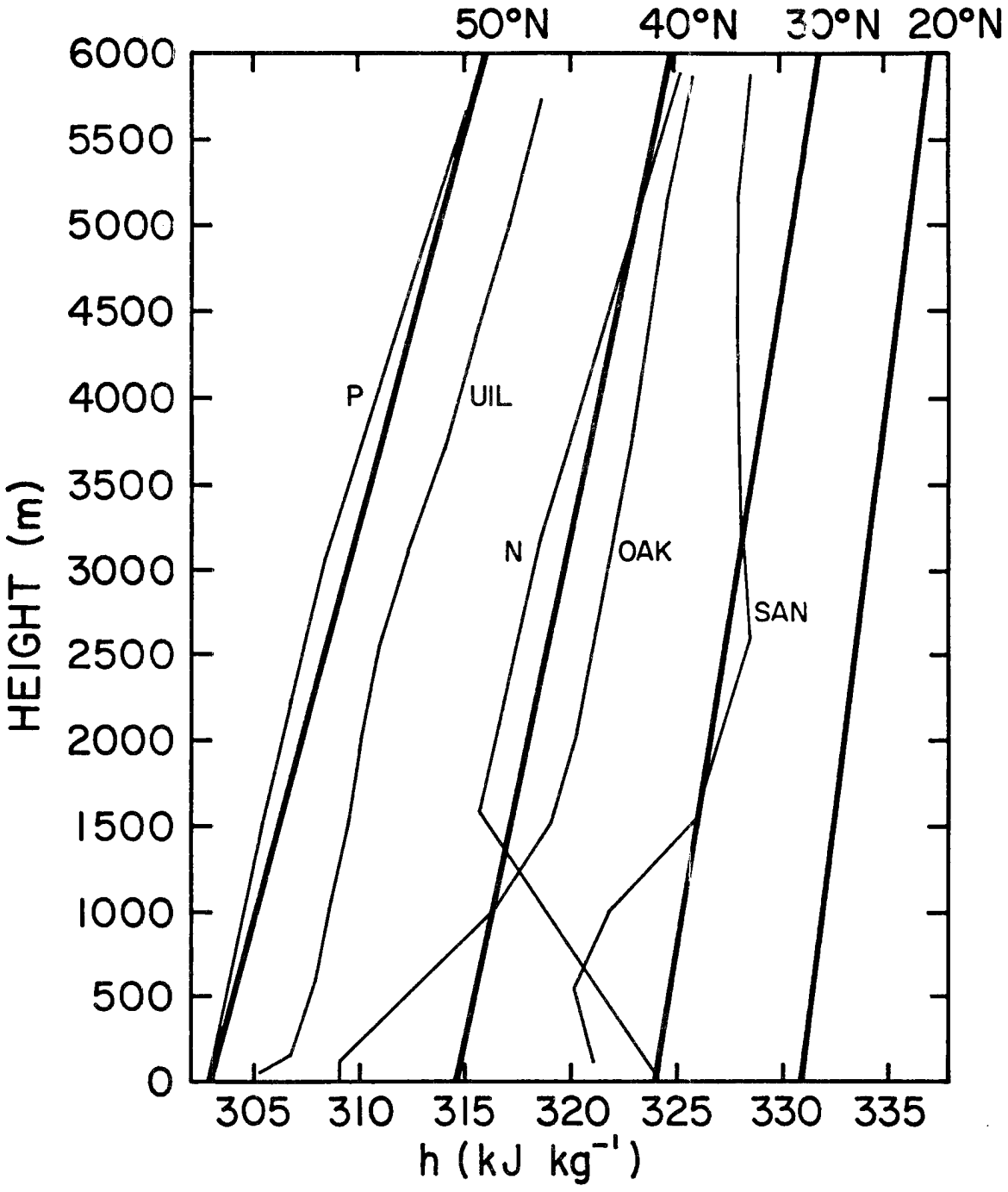

Figure 4.7. Profiles of moist static energy from the data in Table 4.1 and from (4.1). P=Ship P (50°N), UIL=Quillayute (47.9°N), N=Ship N (30°N), OAK=Oakland (37.8°N), SAN=San Diego (32.8°N).

Table 4.1. Mean July (1967-1970) soundings used to compute profiles of h, q, and $F_L^{\downarrow}$ above the mixed layer. The number above the station name is the mean surface pressure. Temperatures are in °C, heights in m, and pressures in kPa.

	101.2 Quillayute			101.35 Oakland			99.85 San Diego			101.8 Ship P			102.2 Ship N		
p	T	T_d	z	T	T_d	z	T	T_d	z	T	T_d	z	T	T_d	z
SFC	11.1	10.2	58	13.5	11.7	6	17.7	15.7	124	10.5	9.3	(0)	20.7	16.8	(0)
100	11.5	10.1	156	12.9	11.1	121			(110)						
95	11.6	6.7	589	17.2	6.2	563	18.9	11.0	552						
90	11.2	2.7	1038	22.8	-1.8	1022	23.4	4.1	1019						
85	9.6	-0.7	1514	21.2	-3.5	1517	22.4	3.2	1517	5.0	0.0	1492	11.7	3.3	1572
80	7.6	-4.7	2016	18.0	-5.4	2038	19.5	1.7	2041						
75	5.1	-8.8	2544	14.4	-8.0	2585	15.7	0.4	2591						
70	2.1	-12.1	3105	10.5	-10.8	3164	11.4	-2.5	3174	-1.5	-12.0	3060	7.2	-11.4	3189
65	-1.1	-15.2	3697	6.4	-13.6	3773	7.0	-5.8	3787						
60	-4.9	-19.1	4334	1.8	-17.4	4427	2.4	-9.9	4442						
55	-9.2	-22.8	5008	-3.0	-21.8	5115	-2.2	-15.3	5136						
50	-14.2	-26.7	5743	-8.2	-27.0	5870	-7.0	-21.5	5890	-16.7	-28.0	5666	-8.7	-28.1	5880
45	-19.6	-32.1	6531	-14.0	-32.0	6675	-12.1	-27.9	6701						
40	-25.9	-37.9	7399	-20.7	-37.5	7563	-18.2	-33.7	7597						
35	-33.1	-43.9	8353	-27.9	-43.6	8537	-25.0	-39.6	8581						
30	-41.2	-49.9	9417	-36.4	-50.3	9625	-33.1	-47.4	9683	-43.0		9311	-37.1	-50.3	9628
25	-49.6		10633	-45.3		10865	-42.2		10941						
20	-54.4		12074	-54.1		12325	-53.1		12415	-53.9		11964	-55.8		12311
17.5	-53.8		12930	-58.0		13173	-59.0		13264						
15	-53.8		13921	-61.9		14136	-65.1		14217	-52.7		13817	-61.9		14115
12.5	-54.9		15089	-65.1		15254	-69.6		15315						
10	-55.6		16512	-65.3		16613	-69.5		16643	-52.9		16433	-65.6		16591
8	-55.1		17937	-63.0		17978	-66.2		17983						
7	-54.6		18790	-61.1		18803	-63.7		18797						
5	-52.7		20953	-56.2		20918	-57.4		20892	-50.8		20926	-57.7		20870
3										-47.9		24276	-51.6		24140
2.5	-46.8		25486	-48.8		25399	-49.2		25359						

equation, plotted in Figure 4.8 along with the original data, is

$$q(z_{B+}) = \begin{cases} \dfrac{20}{z_B + 300 + 30\phi} - 0.0016 & z_B \geq 1500 \\ \dfrac{20}{1800+30\phi} - 0.0016 - (0.42-2.96\cos\phi) \times 10^{-6}(1500-z_B) & z_B < 1500 \end{cases} \quad (g\,g^{-1}), \qquad (4.2)$$

where ϕ is latitude in degrees and the slope below 1500 m is based on the slopes of the Ship N and Ship P data above 1500 m.

The reason for the break at 1500 m may be seen by examining Figure 4.9, which depicts the temperature profiles computed from (4.1) and (4.2). The definition of h implies that

$$T(z_{B+}) = \frac{h(z_{B+}) - Lq(z_{B+}) - gz_B}{c_p}, \qquad (4.3)$$

so that T is easily computed, provided an estimate of L. For the purposes of the numerical integration, L is based on a reference temperature 4.5 degrees colder than the sea surface temperature, so

$$L = 3145922 - 2368(T_S - 4.5), \qquad (4.4)$$

for T_S in kelvins. For the profiles in Figure 4.9, a sea surface temperature of 290 K has been assumed. If the curves above 1500 m had been allowed to extend to the surface, the temperature below 1500 m would be unrealistically cold, and, in fact, the surface temperature at 20°N would be colder than that at 50°N.

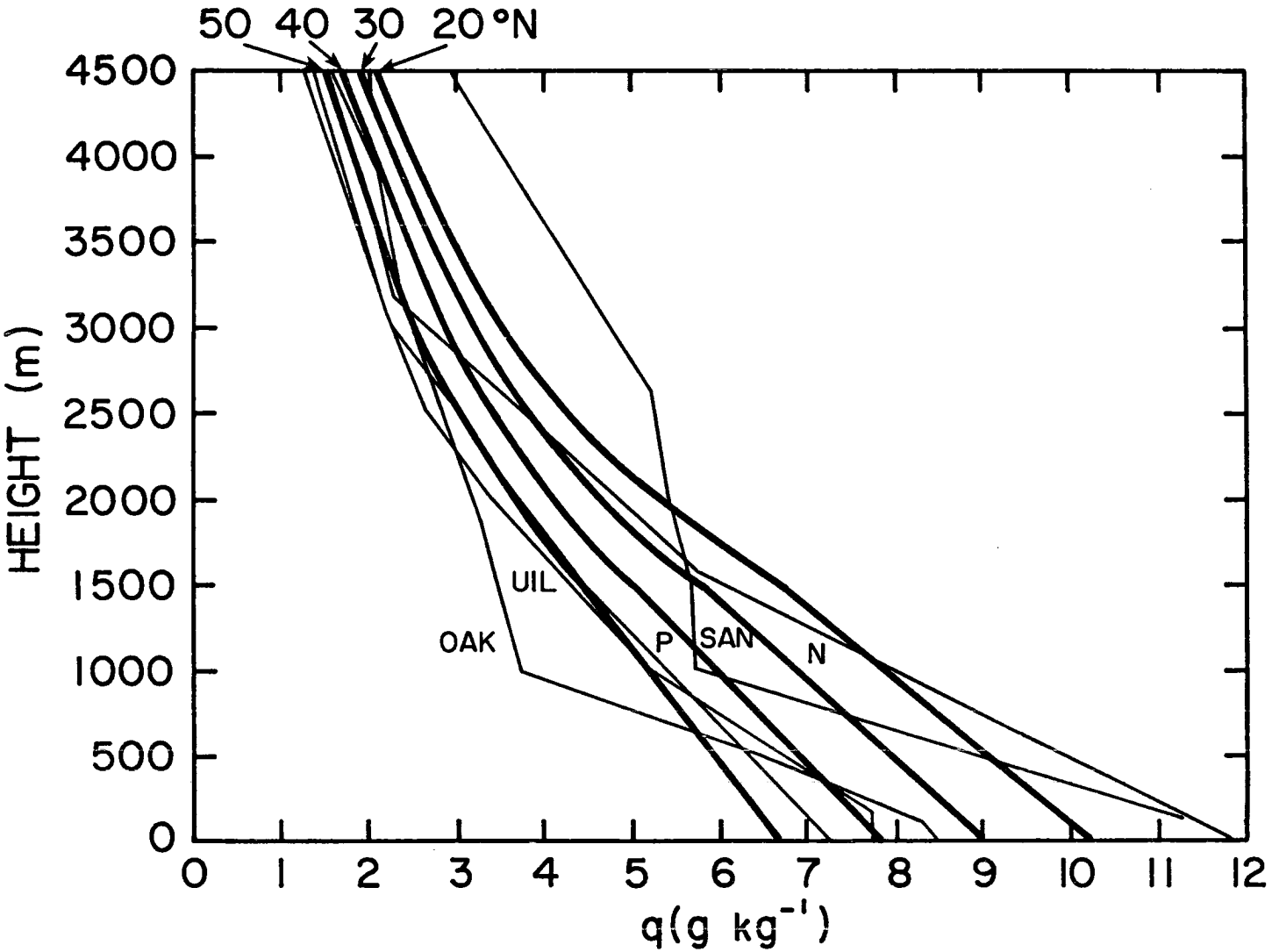

Figure 4.8. Profiles of water vapor mixing ratio from Table 4.1 and (4.2).

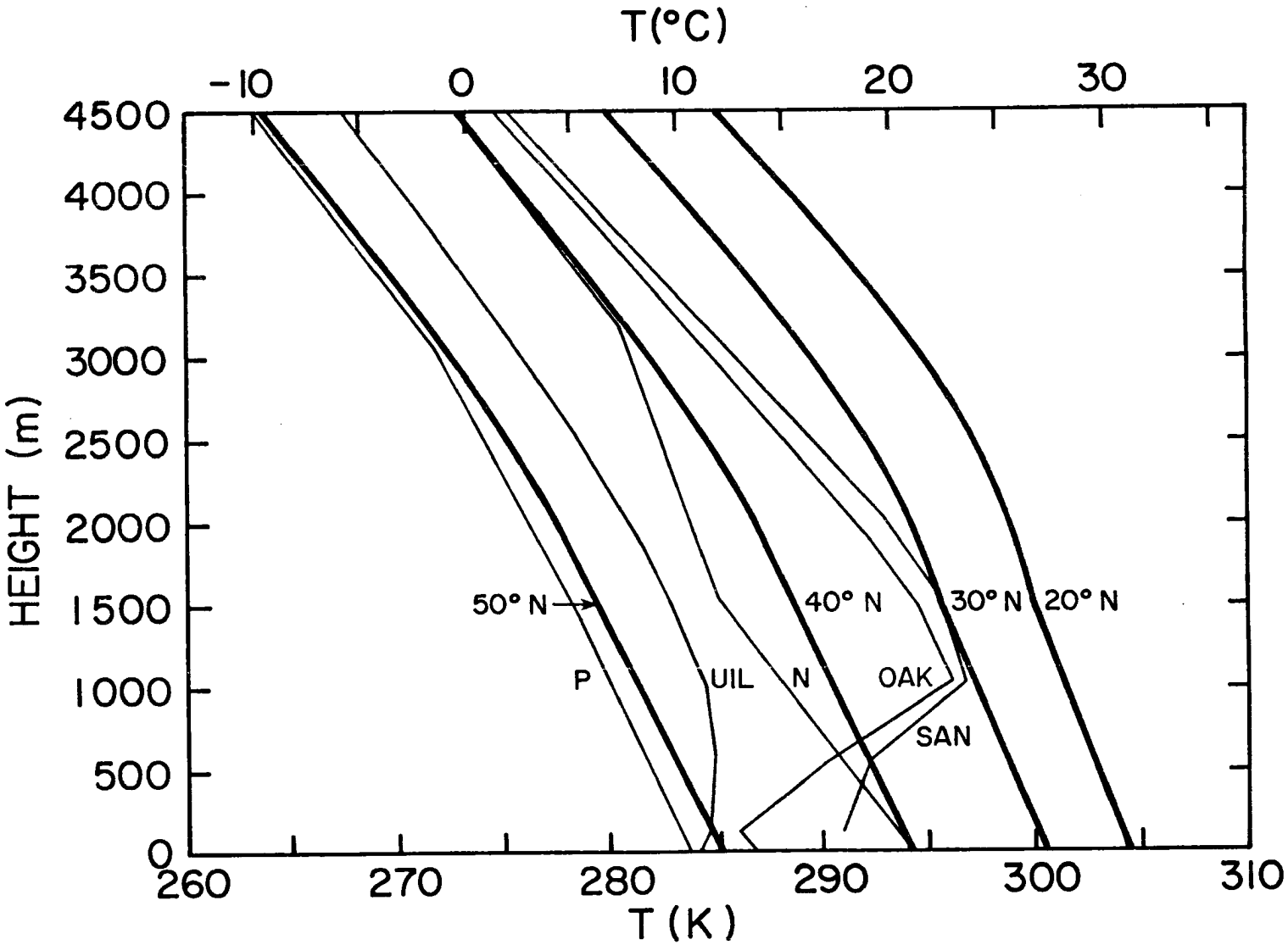

Figure 4.9. Profiles of temperature from Table 4.1 and from (4.3).

4.2.3 Downward longwave radiative flux

The longwave radiative transfer model of Cox (1973) was used to calculate the vertical profiles of downward longwave radiative flux. The inputs to the model are temperature, pressure, and water vapor mixing ratio. Straight lines were fit to these profiles as functions of height and latitude. Illustrated in Figure 4.10 are the calculated profiles and the equation

$$F_L^{\downarrow}(z_{B+}) = 60.23 + 339.9\cos\phi - (1.084+2.974\cos\phi) \times 10^{-2} z_B \quad (W\,m^{-2}) . \tag{4.5}$$

4.3 Procedure

The model as outlined in chapter 2 was integrated over the region bounded by 145°W, 115°W, 40°N, and 20°N. The integration proceeded along the streamlines illustrated in Figure 4.3c. Descriptions of the method employed and of the initialization procedure are given in the following sections.

4.3.1 Trajectory calculations

Given an initial position, a wind direction, and a distance increment, one may calculate a new position using the methods of great circle navigation. The procedure employed herein has been discussed by Steiner and Schubert (1977). A summary will be presented here.

Referring to Figure 4.11, if we move a distance d in a direction α from point (ϕ_i, λ_i), we will arrive at point $(\phi_{i+1}, \lambda_{i+1})$. By applying the cosine law for sides of a spherical triangle, we find that

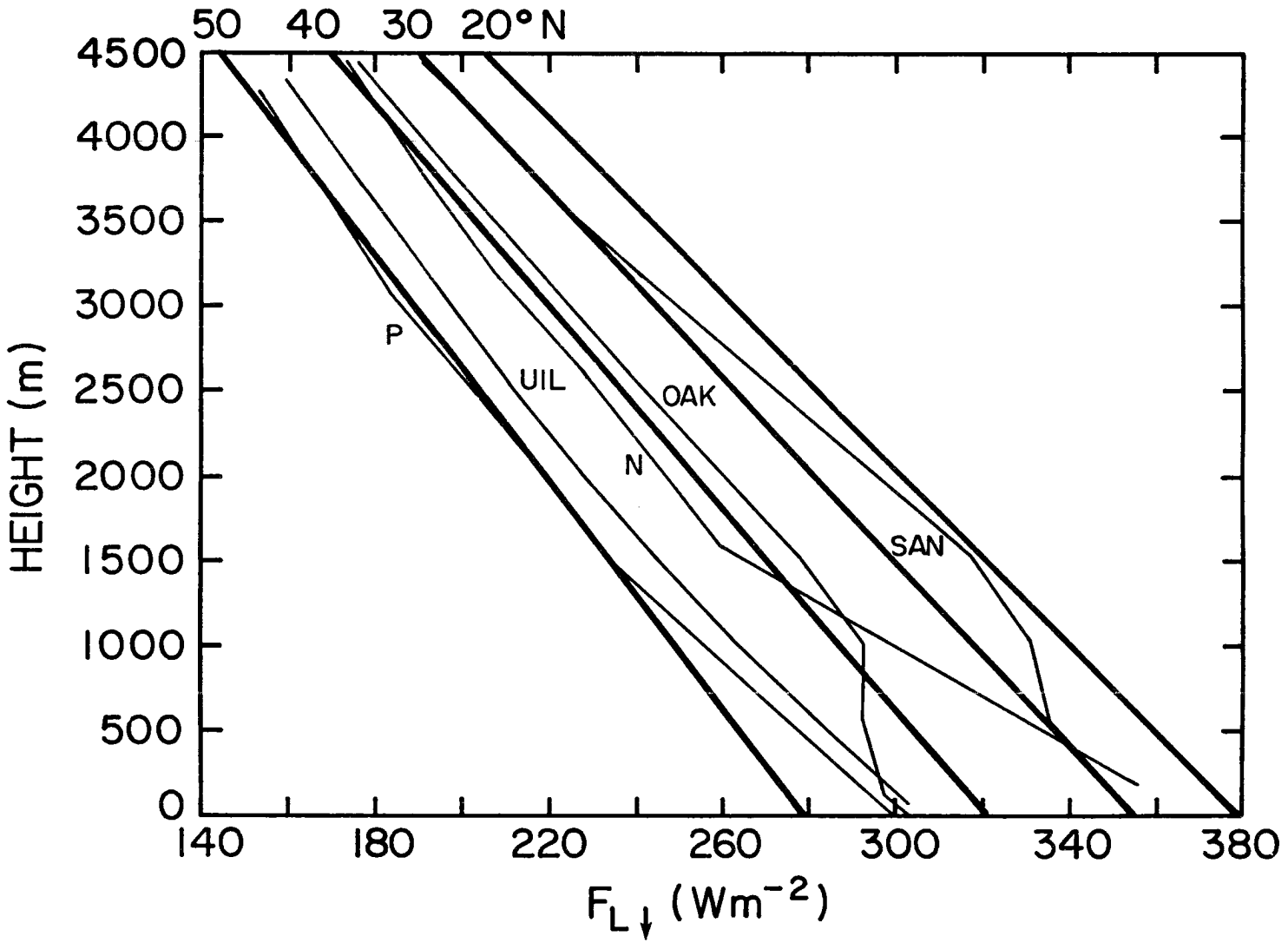

Figure 4.10. Profiles of downward longwave radiative flux calculated from the data in Table 4.1 and from (4.5).

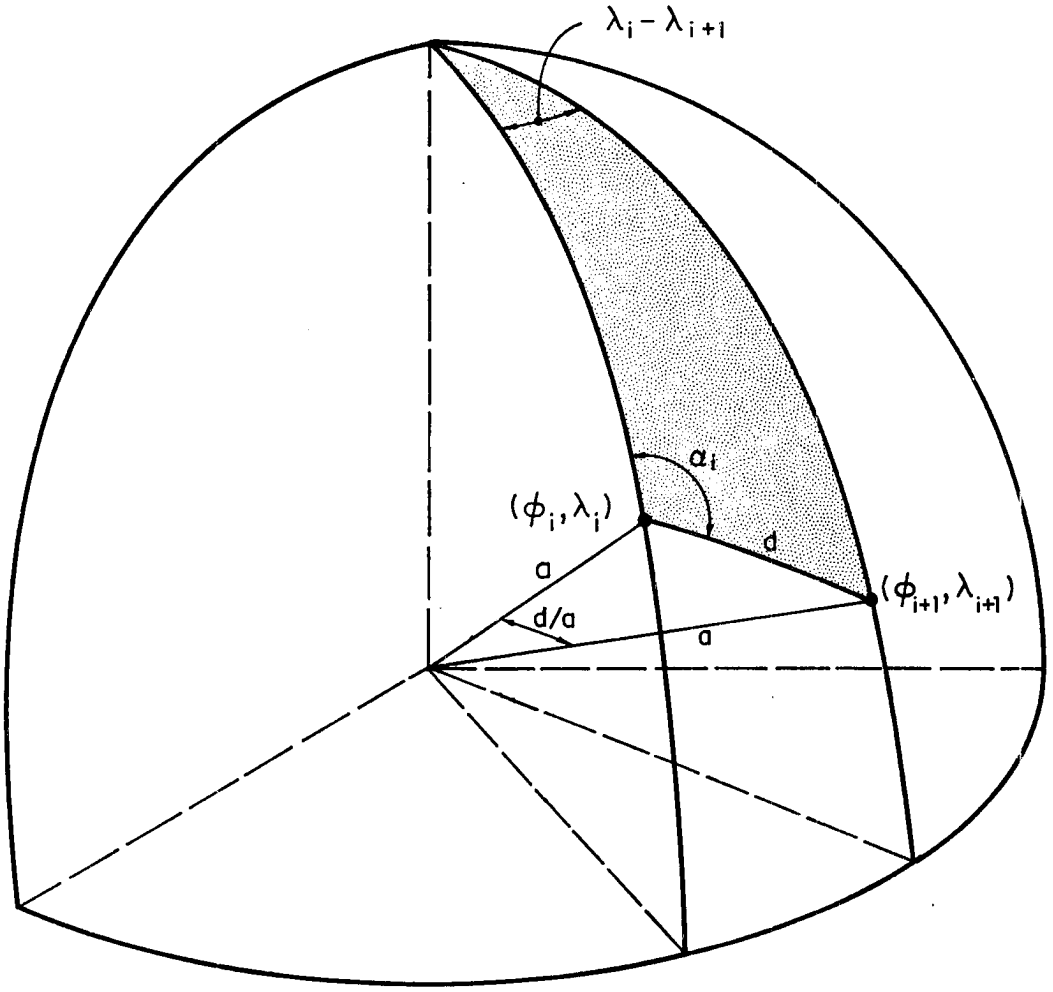

Figure 4.11. Method used for the trajectory calculation.

$$\sin\phi_{i+1} = \sin\phi_i \cos(\frac{d}{a}) + \cos\phi_i \sin(\frac{d}{a}) \cos\alpha \,, \tag{4.6}$$

$$\cos(\lambda_i - \lambda_{i+1}) = \frac{\cos(\frac{d}{a}) - \sin\phi_i \sin\phi_{i+1}}{\cos\phi_i \cos\phi_{i+1}} \,, \tag{4.7}$$

where a is the radius of the earth, ϕ is latitude, and λ is longitude.

By making use of (4.6), (4.7), and the wind data presented earlier in this chapter, the behavior of the mixed layer may be studied as the air flows along the streamlines of Figure 4.3c. The trajectories† are initialized at one-half degree intervals along the west and north sides of the grid and followed equatorward with a distance increment of 5000 m.

4.3.2 Initialization of trajectories

An examination of the model equations (Chapter 2) reveals that for the initial pass through the system, the following need to be known: C_T, V, h_S^*, h_M, q_S^*, $(q+\ell)_M$, H, γ, L, b, $h(z_{B+})$, $q(z_{B+})$, c_p, z_B, g, σ, $F_L^{\downarrow}(z_{B+})$, ΔF_S, β, ε, δ, k, and D. Values assumed for the constants are listed in Table 4.2. For those remaining constants which require a reference temperature and/or pressure (b, H, L, β, γ, and ε), a reference temperature of 4.5 K colder than the sea surface temperature, and a reference pressure 4.5 kPa less than the assumed surface pressure (102 kPa) were used. The remaining parameters are all

†Under the assumption of steady state winds made here, the terms trajectory and streamline are interchangeable. In the more general case, trajectories would be calculated, so we use that term.

Table 4.2. Constants used in integration.

$c_p = 1004.52\ J\ kg^{-1}\ K^{-1}$
$g = 9.8\ m\ s^{-1}$
$k = 0.2$
$\delta = 0.608$
$\sigma = 5.67 \times 10^{-8}\ W\ m^{-2}\ K^{-4}$

externally specified by the fields and profiles presented in sections 4.1 and 4.2, with the exception of h_M, $(q+\ell)_M$, and z_B.

Cloud top height, z_B, was initialized using Neiburger et al.'s (1961) observations. The data were obtained from Figure 4.12, which is taken from that study. Initial z_B for each of the trajectories is listed in Table 4.3.

Initial h_M and $(q+\ell)_M$ were obtained from (2.3), which may be rewritten

$$(q+\ell)_M = \frac{\gamma}{L}\left((s-L\ell)_M - h_S^*\right) + (1+\gamma)q_S^* - \frac{bz_C}{H}\ , \tag{4.8}$$

where $(s-L\ell)_M$ is simply $h_M - L(q+\ell)_M$. Assuming that $z_C = z_B/2$ and that there is no air-sea temperature difference, so that $(s - L\ell)_M$ is given by

$$(s - L\ell)_M = c_p T_S\ , \tag{4.9}$$

(4.8) reduces to

$$(q+\ell)_M = q_S^* - \frac{bz_B}{2H}\ . \tag{4.10}$$

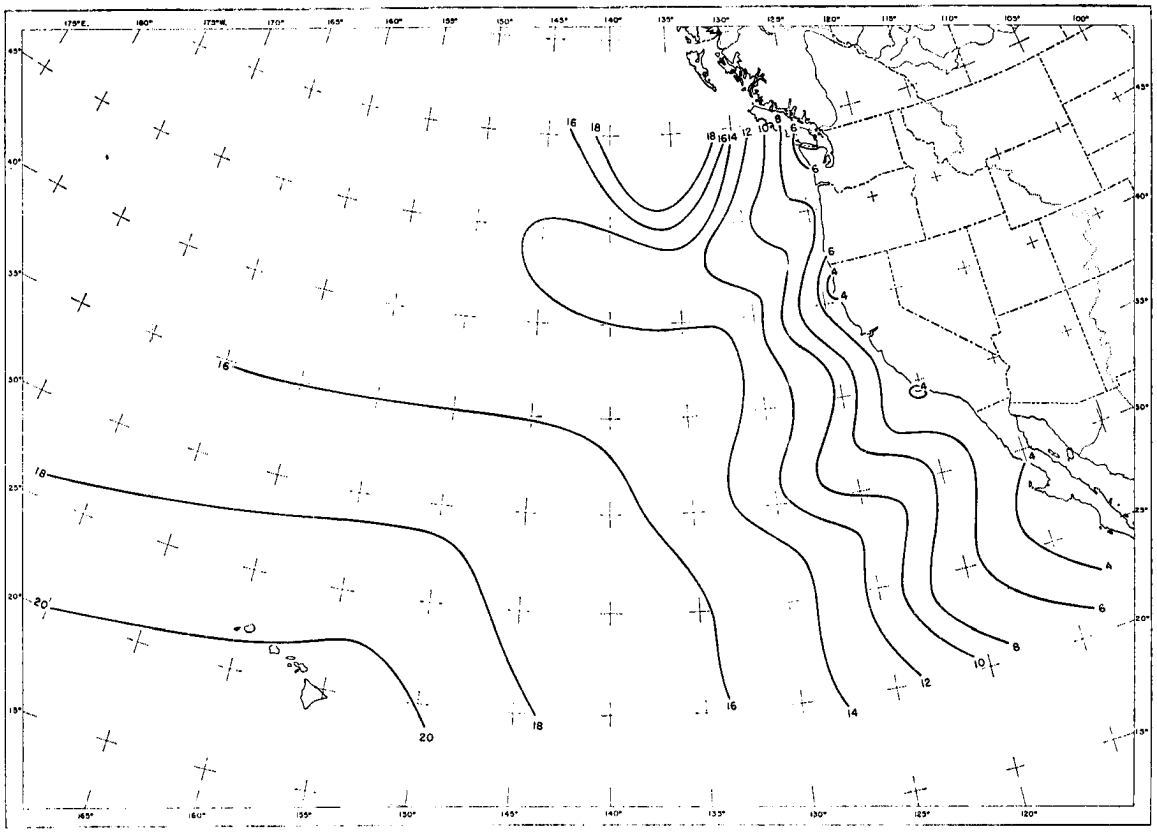

Figure 4.12. June through September cloud-top data (hm) from Neiburger et al. (1961).

Table 4.3 Initial cloud-top heights for the 30 trajectories.

Latitude	Longitude	Initial z_B (m)
40	145	1460
40	144	1450
40	143	1435
40	142	1425
40	141	1415
40	140	1400
40	139	1395
40	138	1390
40	137	1390
40	136	1390
40	135	1390
40	134	1385
40	133	1380
40	132	1355
40	131	1300
40	130	1235
40	129	1130
40	128	1010
40	127	860
40	126	720
40	125	570
40	124	380
40	123	370
40	122	360
40	121	350
40	120	340
40	119	330
40	118	320
40	117	310
40	116	300

Then, by definition,

$$h_M = (s-L\ell)_M + L(q+\ell)_M \ . \tag{4.11}$$

Results of the numerical integration were written on tape for every 5th time/distance step (i.e. every 25 km) along each of the 30 trajectories. These included the latitude and longitude of each set of results. These numbers were interpolated onto a one-half degree square grid and machine contoured. The analyzed fields will be presented and discussed in the next chapter.

5. Results and discussion

In this chapter, the results of the numerical integration of the model will be presented and compared to observations. In addition, the results will be discussed in general terms.

5.1 Results of the numerical integrations

Two runs of the model were made during the course of this research. In the first, initialization was made along the north and west edges of the grid, to 50°N latitude. Results did not adequately reproduce the observations of Neiburger et al. (1961), primarily as a result of the initialization of the model. Shown in Figure 5.1 is the cloud top height field produced by the model. It can be seen that cloud tops are significantly higher than those observed (Figure 4.12) and that the gradients are oriented at right angles to each other in some instances. Since the initialization is at high z_B in the north central part of the field and this is a region of low divergence, the cloud tops rise to unrealistically high values off the coast of Oregon and Washington.

Other results were equally bad in various ways. In addition, the observations are probably less reliable in the north, where inversions are less frequent (Figure 1.2). Consequently, a second run was made with initialization at 40°N latitude. These results are described below.

5.1.1 Mixed layer depth and cloud thickness

The physical dimensions of the model-produced clouds are illustrated in Figure 5.2. Isolines of cloud top height, z_B, are shown in

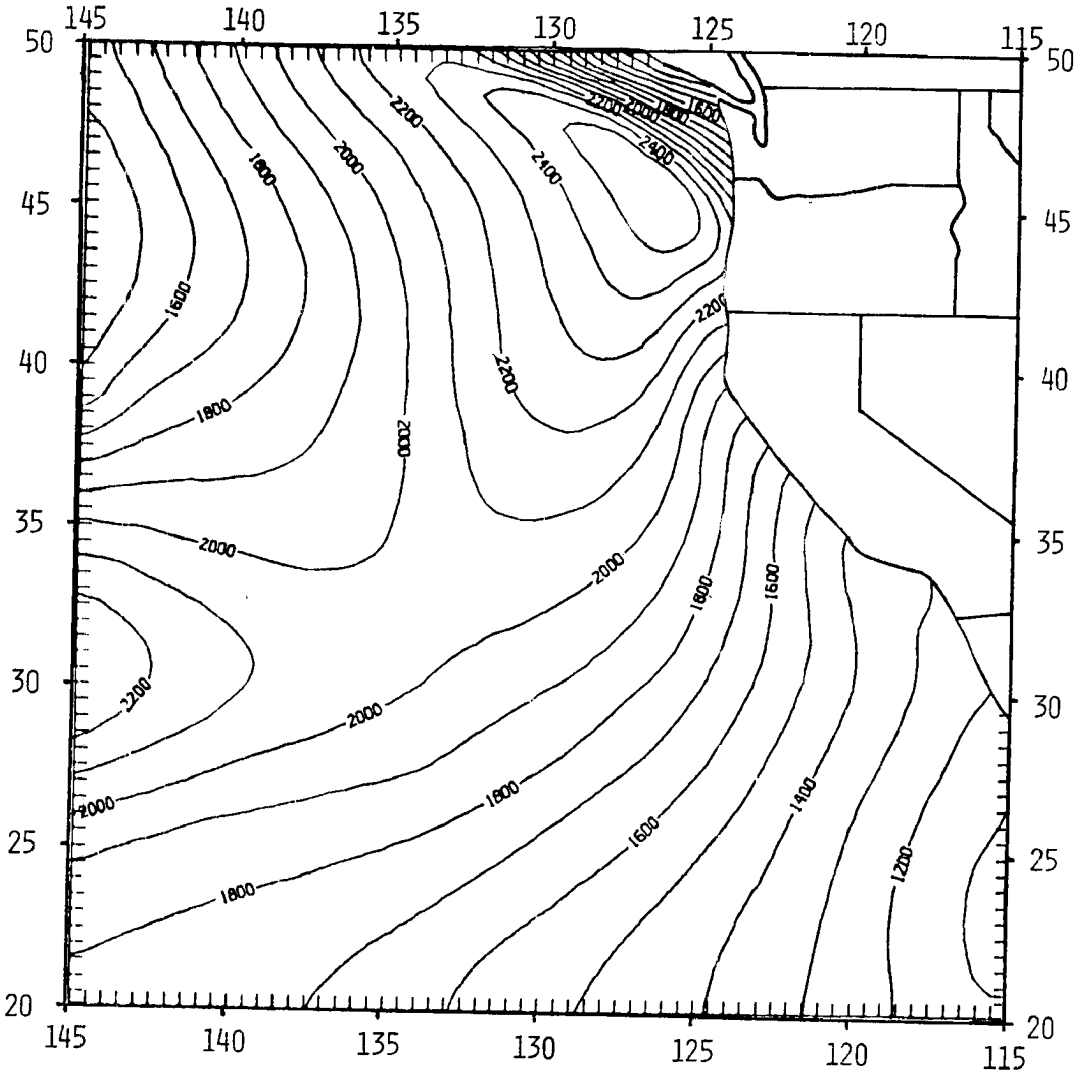

Figure 5.1. Cloud top heights produced by the model with initialization at 50°N (m).

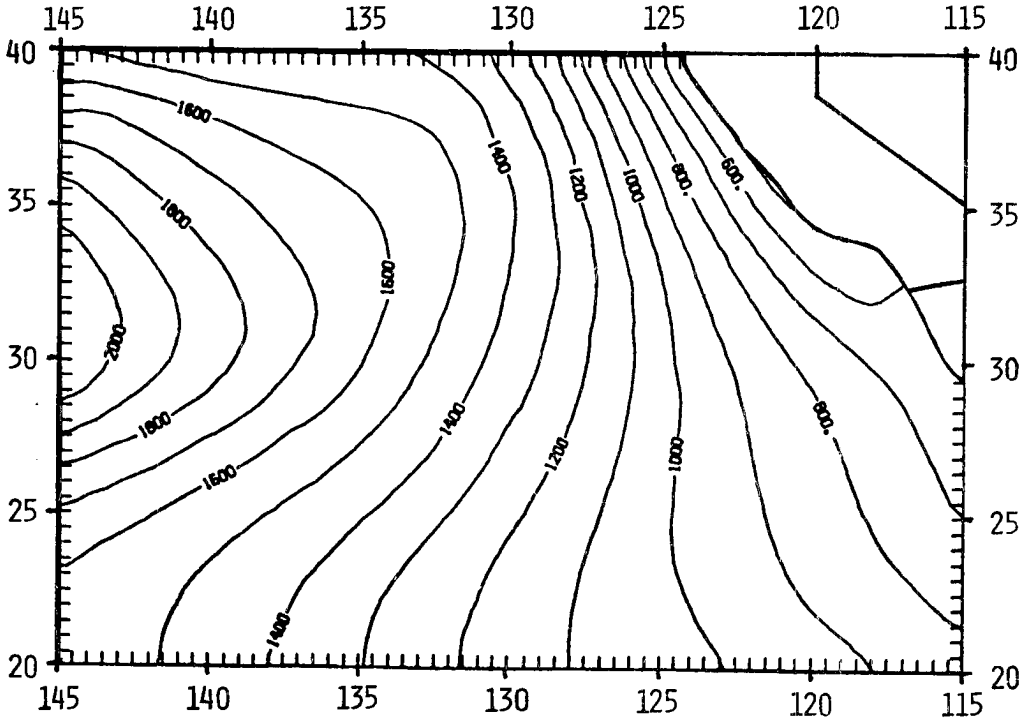

Figure 5.2a. Cloud top height (m).

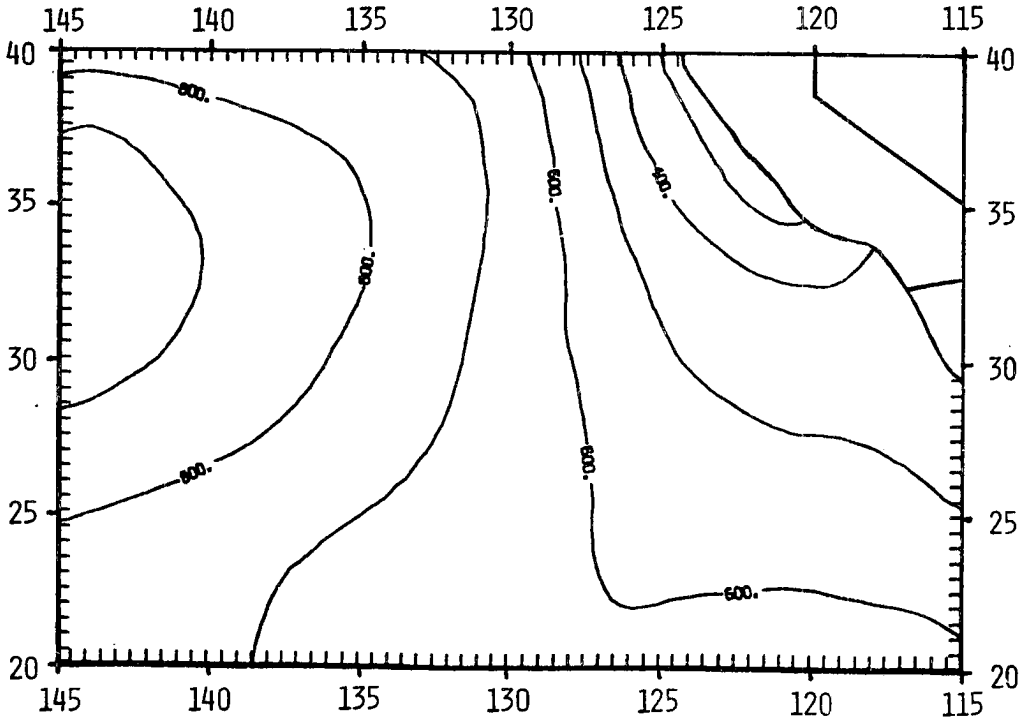

Figure 5.2b. Cloud base height (m).

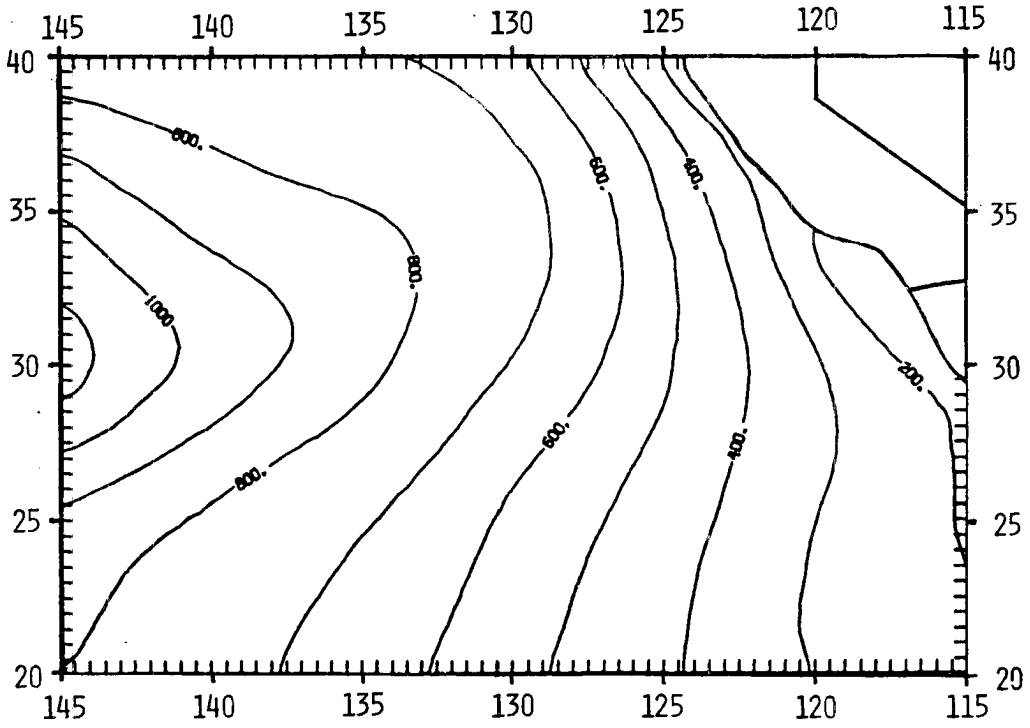

Figure 5.2c. Cloud thickness (m).

Figure 5.2a; cloud base height, z_C, in Figure 5.2b; and cloud thickness, $z_B - z_C$, in Figure 5.2c.

In this case, it can be seen (Figure 5.2a) that the mixed layer is initially near equilibrium along the coast, since z_B there is nearly constant along the trajectories. Away from the coast, cloud tops rise to the west, in accordance with the lower divergence there. (As noted by Schubert et al. (1978a), cloud top height is roughly inversely proportional to divergence).

Cloud base height, z_C, (Figure 5.2b) is closely related to sea surface temperature. A comparison of Figures 5.2b, 4.1, and 4.3c shows that the most rapid changes in z_C occur where both the wind speed is high and the sea surface temperature isolines are closely packed.

Equation (2.3), which governs the cloud base height, can be used to examine the effects of changing sea surface temperature on z_C. Using typical values of h_M and $(q+\ell)_M$, an increase of 4°C in sea surface temperature results in a less than 1% increase in the cloud base height. The relatively small increase of z_C with increasing sea surface temperature may be understood by observing that q_S^* and h_S^* increase in a related manner such that the difference in (2.3) is unchanged. This arises from the relation that

$$\frac{\gamma}{L}\Delta h_S^* = (1+\gamma)\Delta q_S^* \ , \tag{5.1}$$

which follows simply from the definition of γ. Thus, small changes in z_C arising from a change in sea surface temperature must be due to changes in γ, H, L, and b in (2.3). When sea surface temperature rises, however, both h_S^* and q_S^* and, accordingly, surface fluxes of

h and q, increase. This results in small increases in h_M and $(q+\ell)_M$. Even a 1% rise in h_M and $(q+\ell)_M$ leads to a significant (approximately 40% in this case) raising of cloud base. Model results to be presented later indicate that $(q+\ell)_M$ increases more slowly than h_M in the region off the central California coast, which means that the air temperature rises (as expected). Therefore, cloud base rises in this area.

Cloud base height responds more quickly to varying external parameters than does the mixed layer depth, z_B. This result was explored numerically and analytically by Schubert et al. (1978b), who found that the response time of z_B was an order of magnitude longer than that for z_C.

The cloud thickness field (Figure 5.2c) closely follows that of the cloud top height field, further illustrating that the response of cloud top height is larger than that of cloud base height. It can be seen in Figure 5.2c that almost all of the clouds are thick enough that the blackbody assumption for longwave emissivity would be reasonable. In terms of shortwave absorption, however, Figure 3.3 shows that ΔF_S may vary by a factor of 4 over the range of thicknesses produced by the integrations.

Comparison of Figures 5.2b and 5.2c illustrates the importance of the initialization of z_C. At the north edge of the grid, z_C and $z_B - z_C$ are almost identical. Although this indicates further that the layer is near equilibrium (otherwise, rapid changes would be evident), it also means that downstream results may be influenced to a considerable degree by the choice of z_C initially. As noted above, however, z_C responds rapidly to imbalance, and we might expect that a different initial z_C would not produce significant changes in the results.

5.1.2 Mixed layer properties

The mixed layer values of both moist static energy and total water mixing ratio closely parallel the sea surface temperature. Isolines of h_M and $(q+\ell)_M$ are shown in Figure 5.3. Note that near the central California coast, h_M increases more rapidly than $(q+\ell)_M$ along the trajectories. This indicates that the air is warming. This warming may be examined by comparing the air temperature near the surface ($T_{air} = (h_M - L(q+\ell)_M/c_p)$ with the sea surface temperature, isolines of which are shown in Figure 5.4.

As the air flows south along the California coast, it crosses a region of positive gradient in the sea surface temperature. Since the air temperature exhibits inertia (as seen in the diurnal variation experiments of Chapter 4) it lags behind the warmer water, such that the difference $T_S - T_{air}$ is positive. Note that when the mixed layer is near equilibrium, $T_S - T_{air}$ is slightly negative (as implied in Chapter 4).

5.1.3 Radiative and turbulent fluxes

Surface vertical turbulent fluxes of moist static energy and water vapor mixing ratio are shown in Figure 5.5. The general shape of these fields is closely related to the wind speed (Figure 4.3c), since the surface fluxes are directly proportional to the wind speed (equations (2.1) and (2.2)). The behavior near the coast, however, follows the sea surface temperature (Figure 4.1) in a manner that can be explained by examining (2.1), (2.2), and Figure 5.4. The difference (2.1) - (2.2) implies that

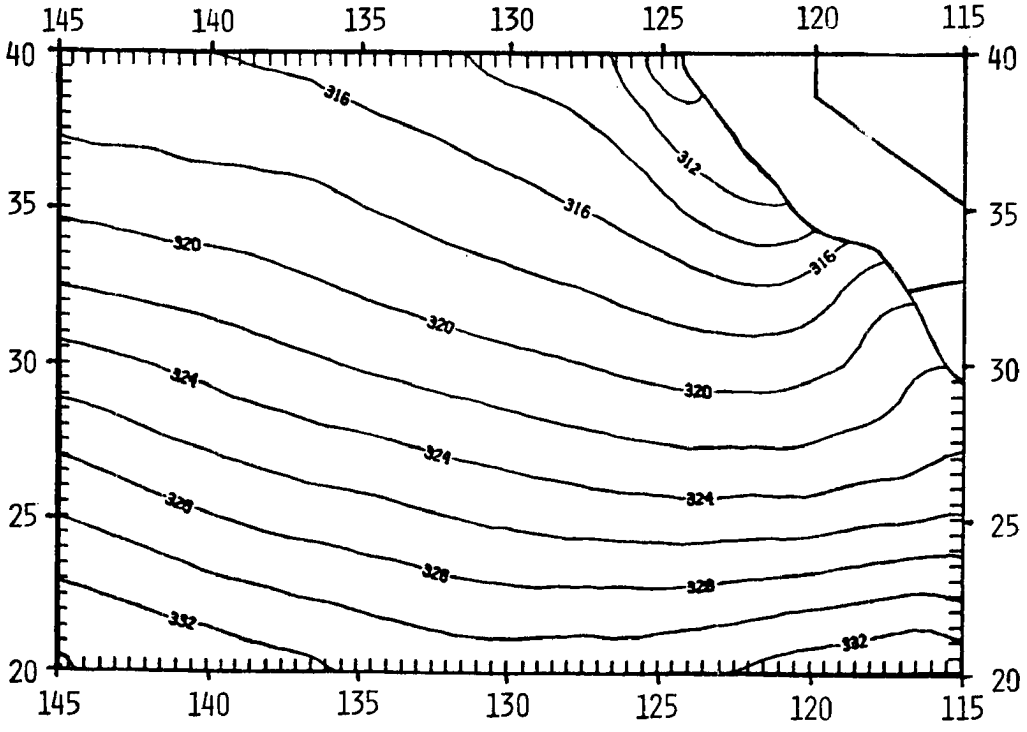

Figure 5.3a. Mixed layer moist static energy ($kJkg^{-1}$).

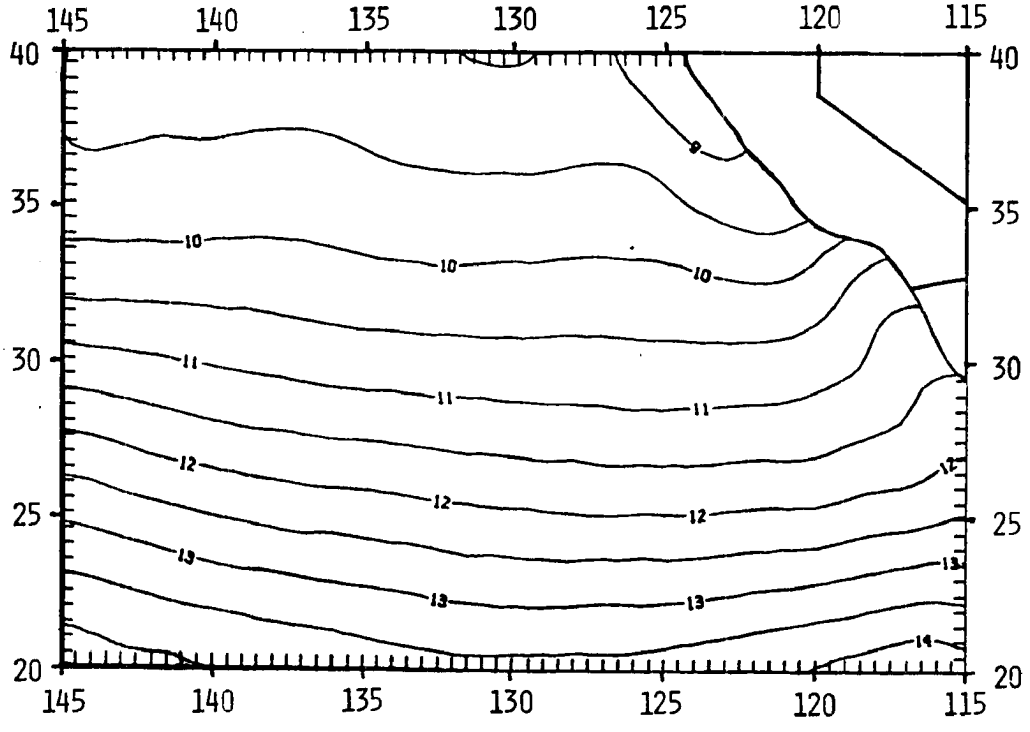

Figure 5.3b. Mixed layer total water mixing ratio (gkg^{-1}).

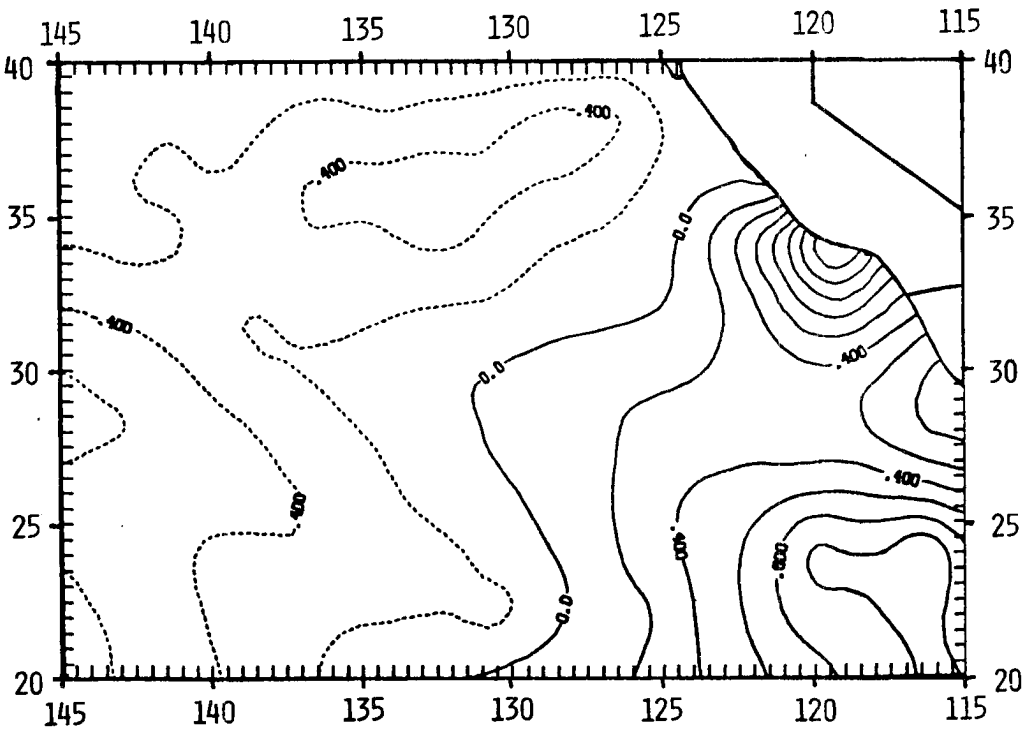

Figure 5.4. Sea surface temperature minus surface air temperature (°C).

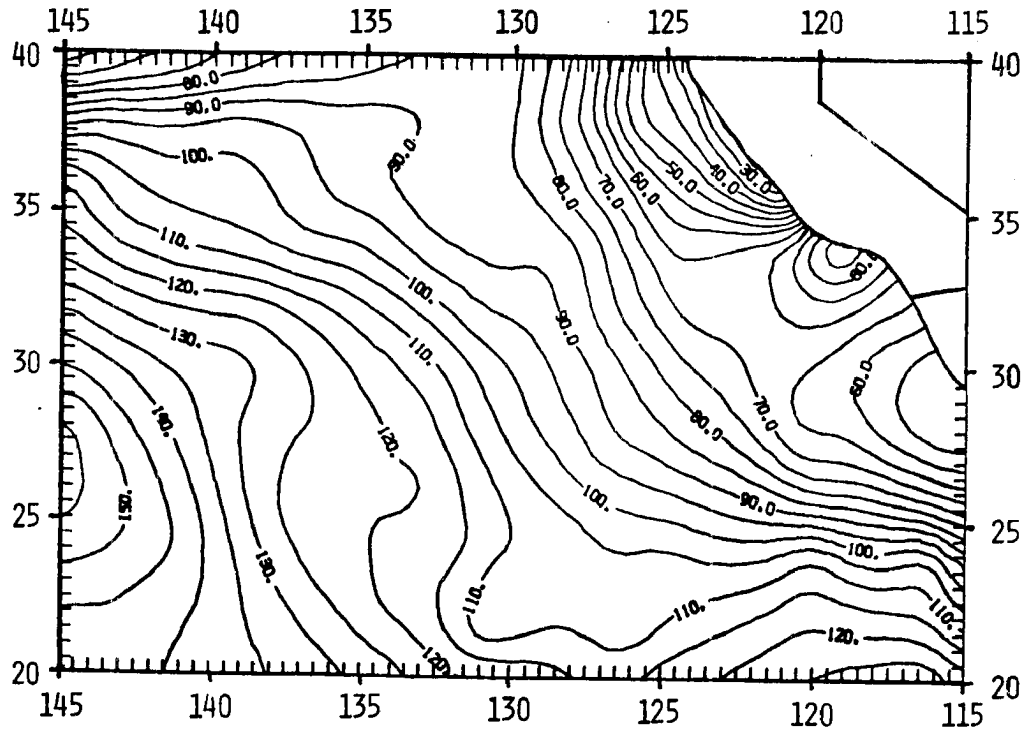

Figure 5.5a. Surface flux of moist static energy (Wm^{-2}).

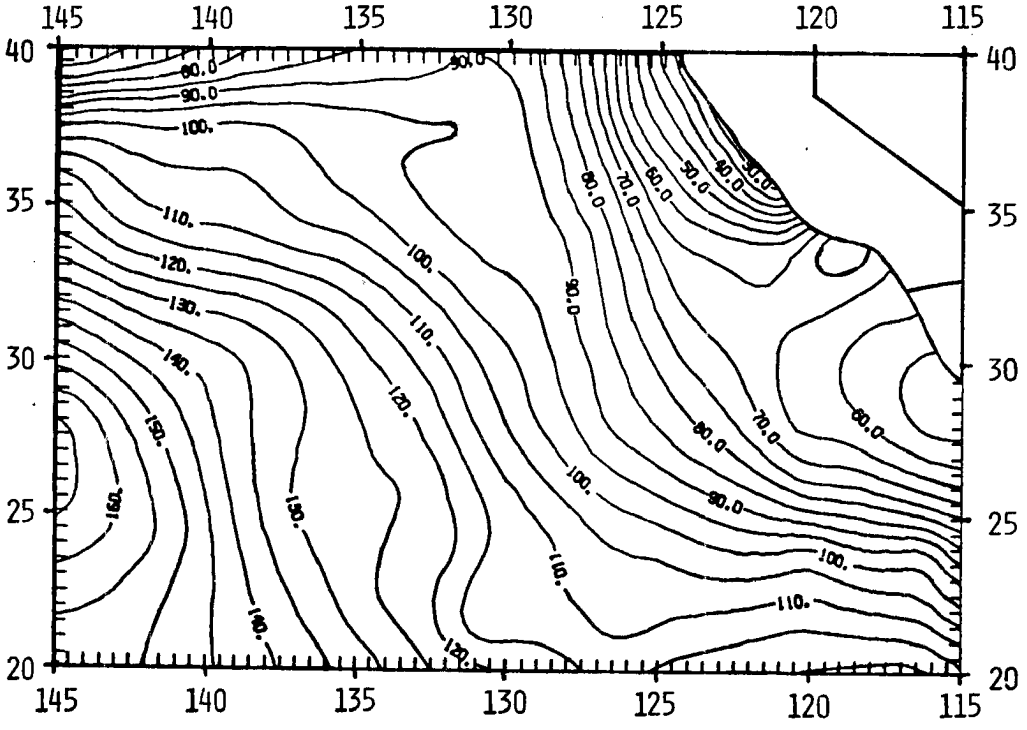

Figure 5.5b. Surface flux of water vapor mixing ratio (Wm^{-2}).

$$(\overline{w's'})_S = C_T V c_p (T_S - T_{air}) \ , \qquad (5.2)$$

or that when $T_S - T_{air}$ is negative $\overline{w'h'}_S < L\overline{w'q'}_S$, and when it is positive, $\overline{w'h'}_S > L\overline{w'q'}_S$. A comparison of Figures 5.4 and 5.5 verifies that this is indeed the case.

Cloud-top fluxes of moist static energy, total water mixing ratio, and longwave radiation (Figure 5.6) are interrelated in a complex manner. The first two (Figures 5.6a and 5.6b) exhibit characteristics similar to the surface fluxes shown earlier, although their general features are oriented more toward the large-scale divergence field (Figure 4.6) than to the sea surface temperature field (Figure 4.1).

The ΔF_L field is similar to the z_B field, with a lesser southeastward slope due to the latitudinal dependence of $F_L^{\downarrow}$ and the increase in the sea surface temperature.

Fluxes of virtual dry static energy are shown in Figure 5.7. These fluxes are simply linear combinations of the moist static energy and water vapor fluxes, as given by equation (2.15). As a result, the surface flux is similar in appearance to the other surface fluxes and the air-sea temperature difference and the cloud-top flux is similar to the other cloud-top fluxes. Note that the flux just below cloud base is always negative and that, as indicated in Chapter 2, the s_v flux increases across cloud base.

5.1.4 Cloud-top jumps and entrainment

Cloud-top jumps of moist static energy and total water mixing ratio are shown in Figure 5.8. The air above the mixed layer is in all cases warmer and drier than the air below the inversion. Thus,

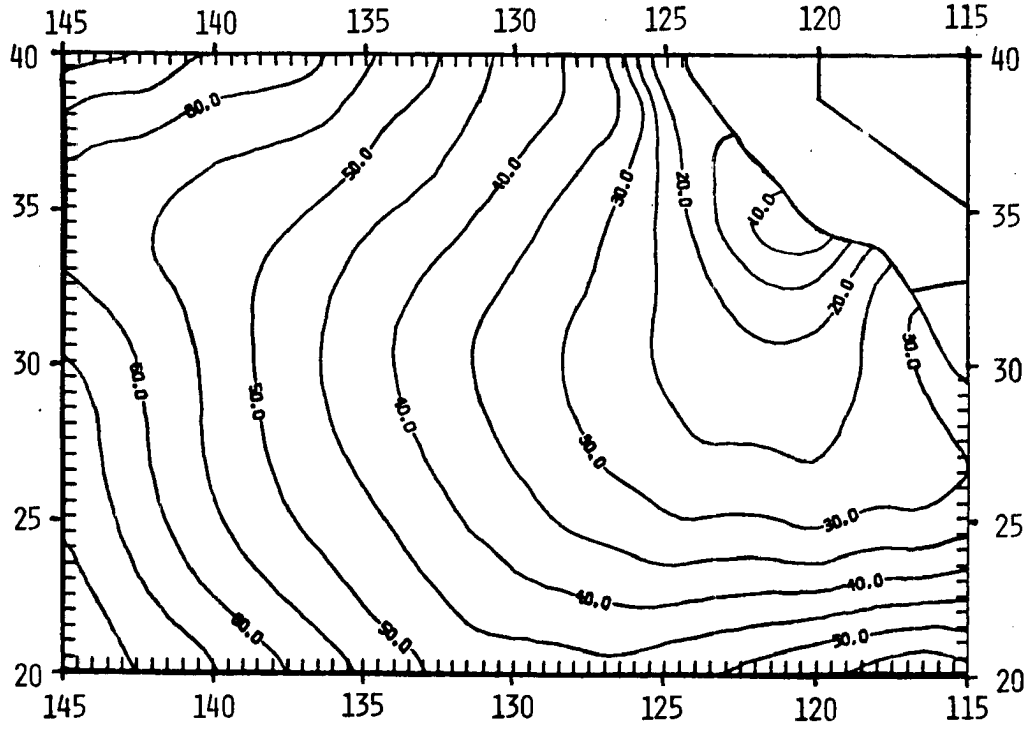

Figure 5.6a. Cloud-top flux of moist static energy, (Wm^{-2}).

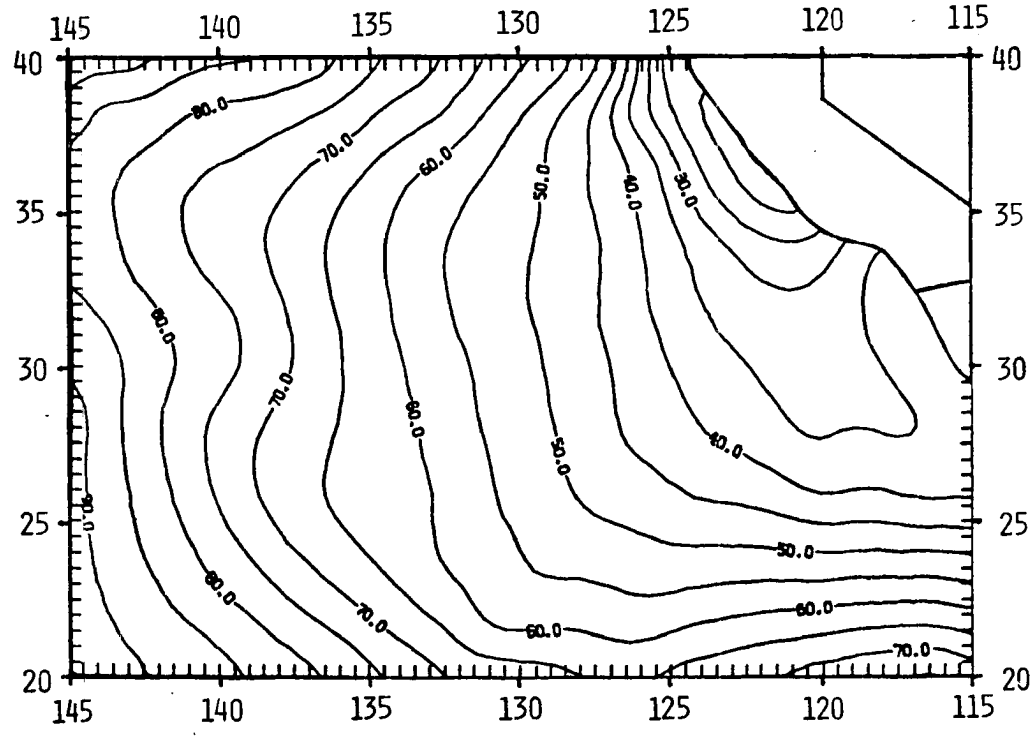

Figure 5.6b. Cloud-top flux of total water mixing ratio (Wm^{-2}).

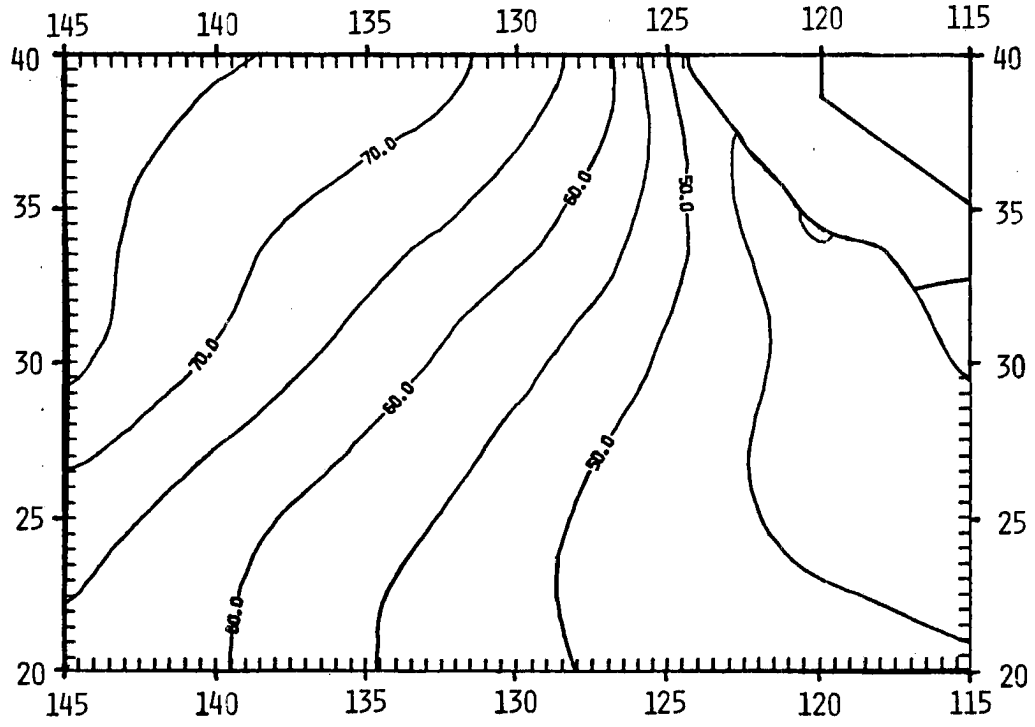

Figure 5.6c. Longwave radiative flux divergence across cloud top (Wm^{-2}).

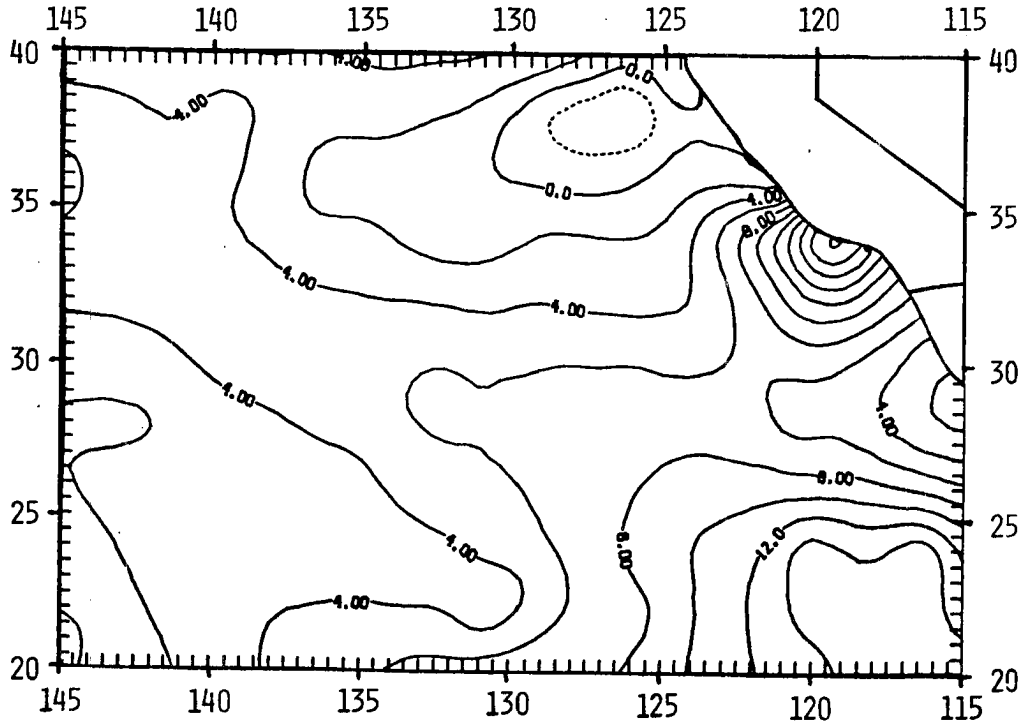

Figure 5.7a. Flux of virtual dry static energy at the surface (Wm^{-2}).

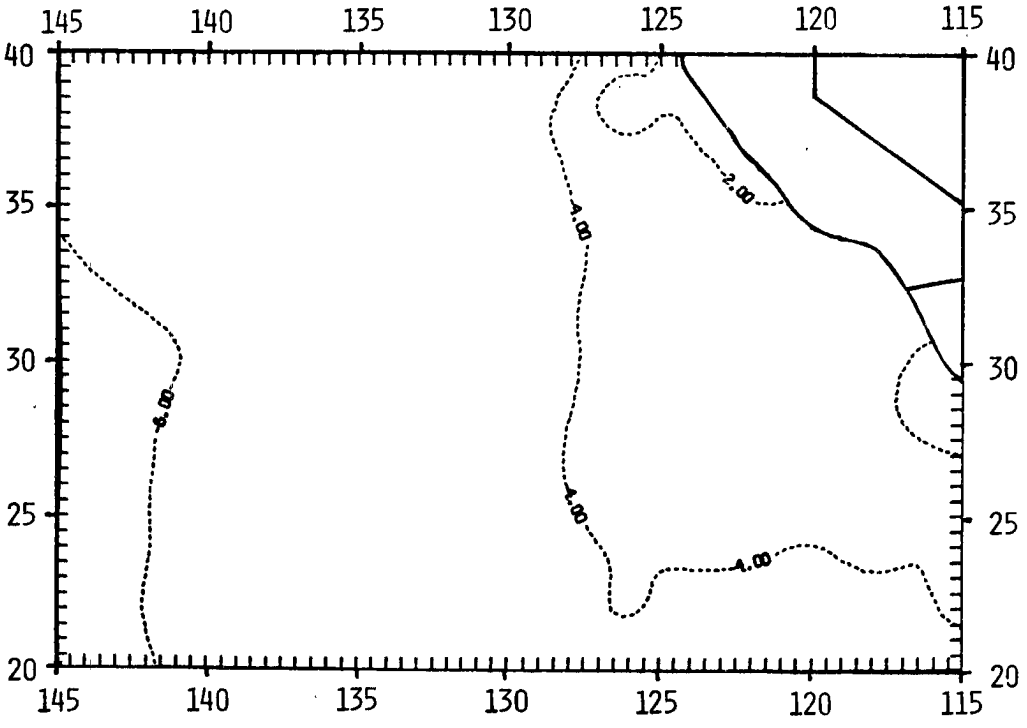

Figure 5.7b. Flux of virtual dry static energy at just below cloud base (Wm^{-2}).

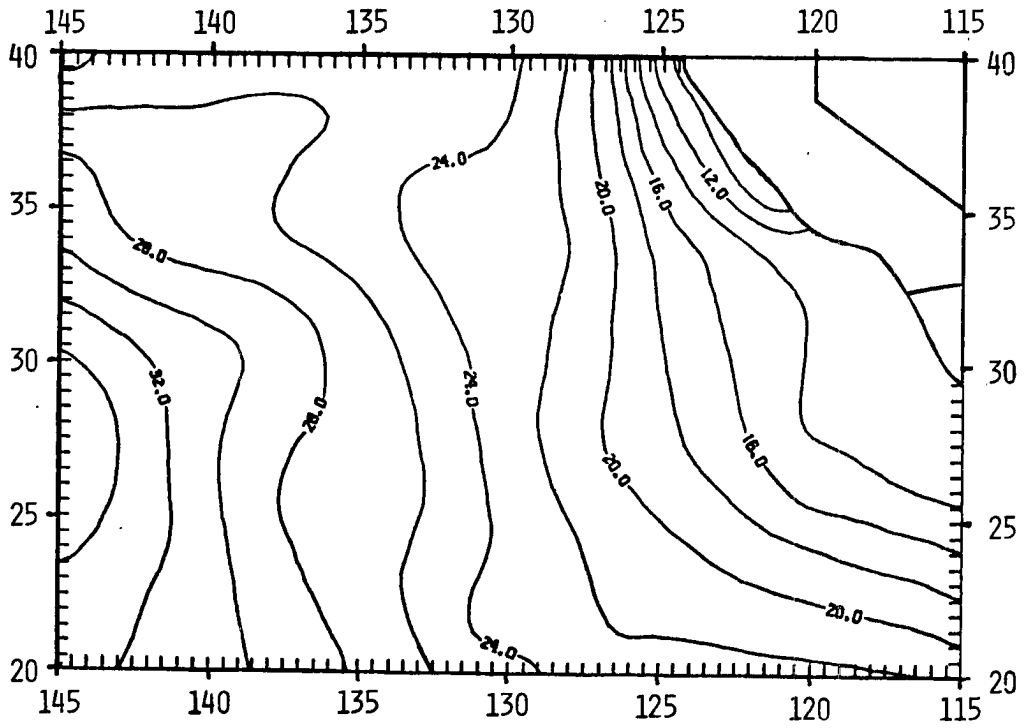

Figure 5.7c. Flux of virtual dry static energy just above cloud base (Wm^{-2}).

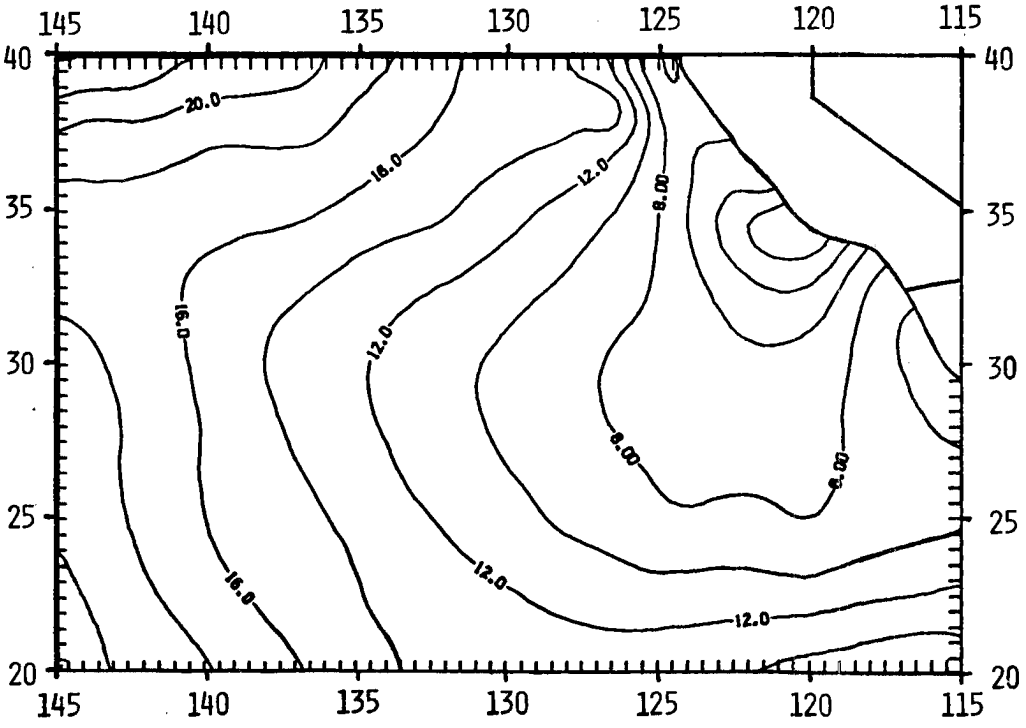

Figure 5.7d. Flux of virtual dry static energy at cloud top (Wm^{-2}).

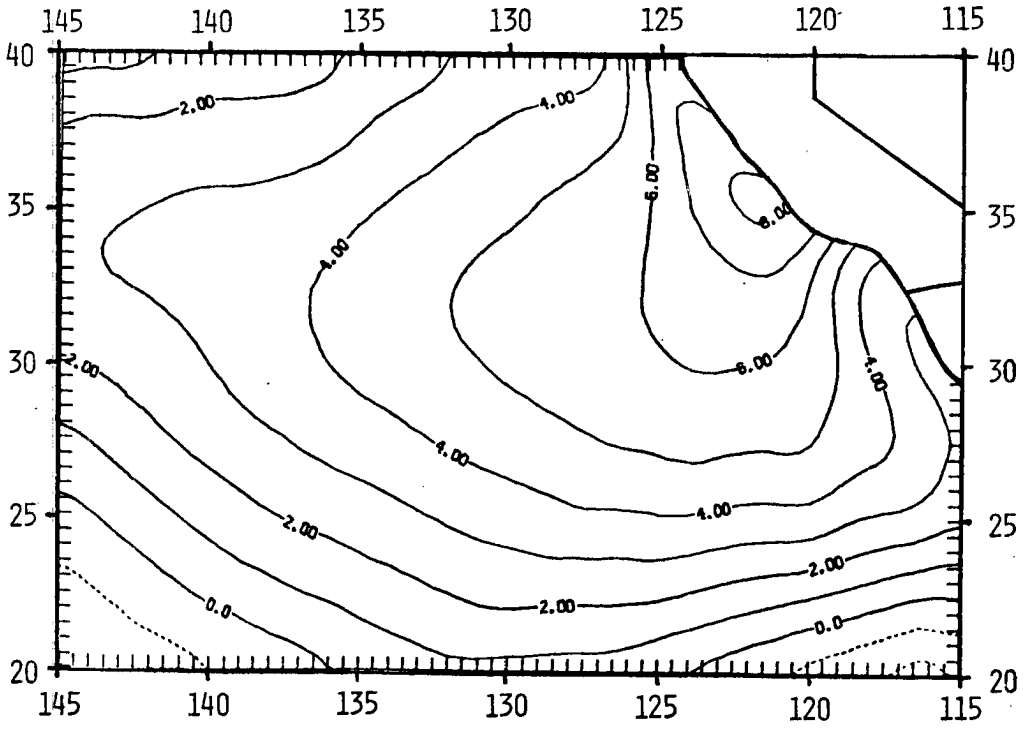

Figure 5.8a. Cloud-top jump of moist static energy ($kJkg^{-1}$).

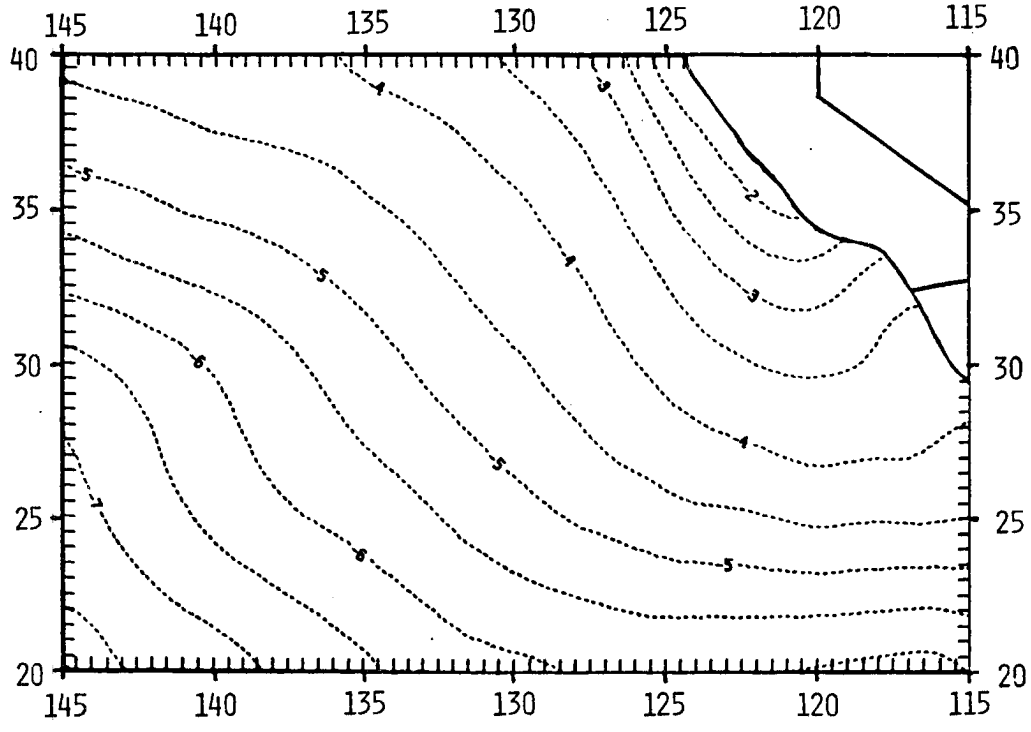

Figure 5.8b. Cloud-top jump of total water mixing ratio (gkg^{-1}).

$\Delta(q+\ell)$ is always negative and Δh is (almost) always positive. In the small areas where Δh is negative (southwestern and southeastern corners), the results are questionable, since negative Δh implies negative buoyancy of a parcel brought from above the mixed layer across the inversion. This situation would be unstable.

The temperature difference from base to top of inversion is shown in Figure 5.9a and the cloud-top temperature in Figure 5.9b. The latitudinal dependence of above-inversion temperature can be seen to play a significant role in the inversion strength.

The cloud-top jumps of h and $q+\ell$ are related by equation (2.9). Another way of rewriting (2.22) and (2.23) is

$$\rho\left(\frac{dz_B}{dt} - w_B\right) = \frac{\Delta F_L - \rho(\overline{w'h'})_B}{\Delta h} = -\frac{\rho\overline{w'(q'+\ell')}_B}{\Delta(q+\ell)} . \qquad (5.3)$$

The left-hand term, $\rho\left(\frac{dz_B}{dt} - w_B\right)$, is just the net mass flowing into the mixed layer per unit horizontal area per unit time, i.e. the net mass entrainment at cloud top. This entrainment is shown in Figure 5.10. Under normal circumstances, the entrainment must be positive, so that air above the inversion is mixed into the mixed layer. Note that since $\Delta(q+\ell)$ is always negative, the entrainment is positive as long as the water flux at cloud top is positive.

In this case, the water flux at cloud top is always positive, so entrainment is always positive. Equation (5.3) indicates that for entrainment to remain positive when Δh becomes negative, ΔF_L must become smaller than $\rho(\overline{w'h'})_B$. That this is indeed the case may be verified by comparing Figures 5.5a, 5.5c, and 5.8a.

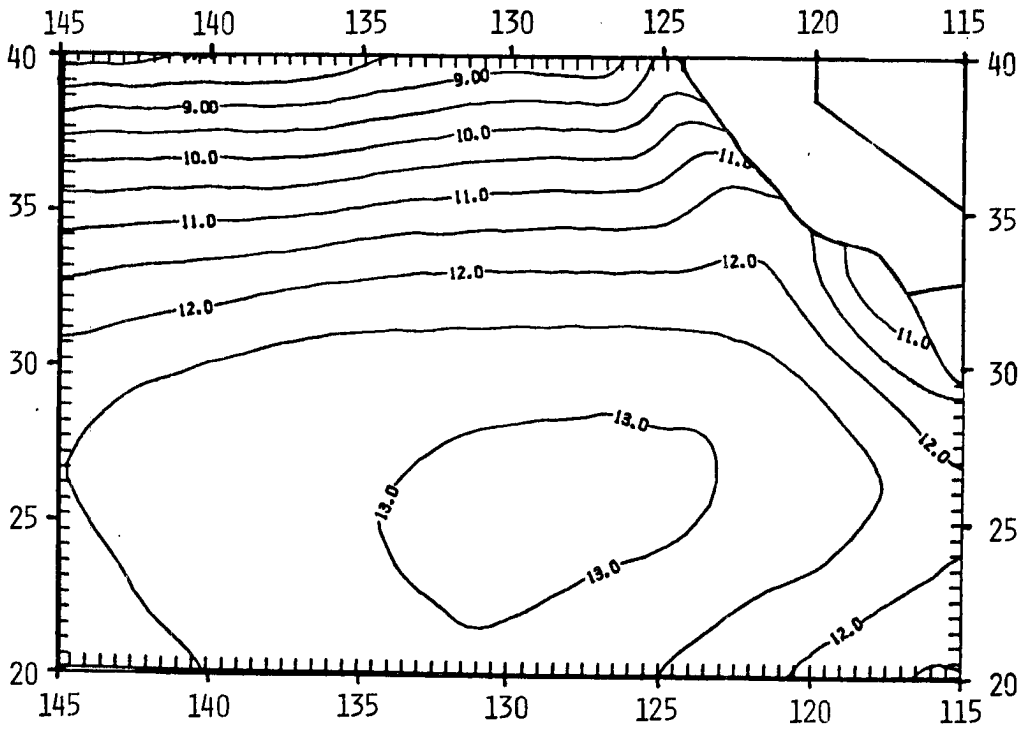

Figure 5.9a. Magnitude of inversion (°C).

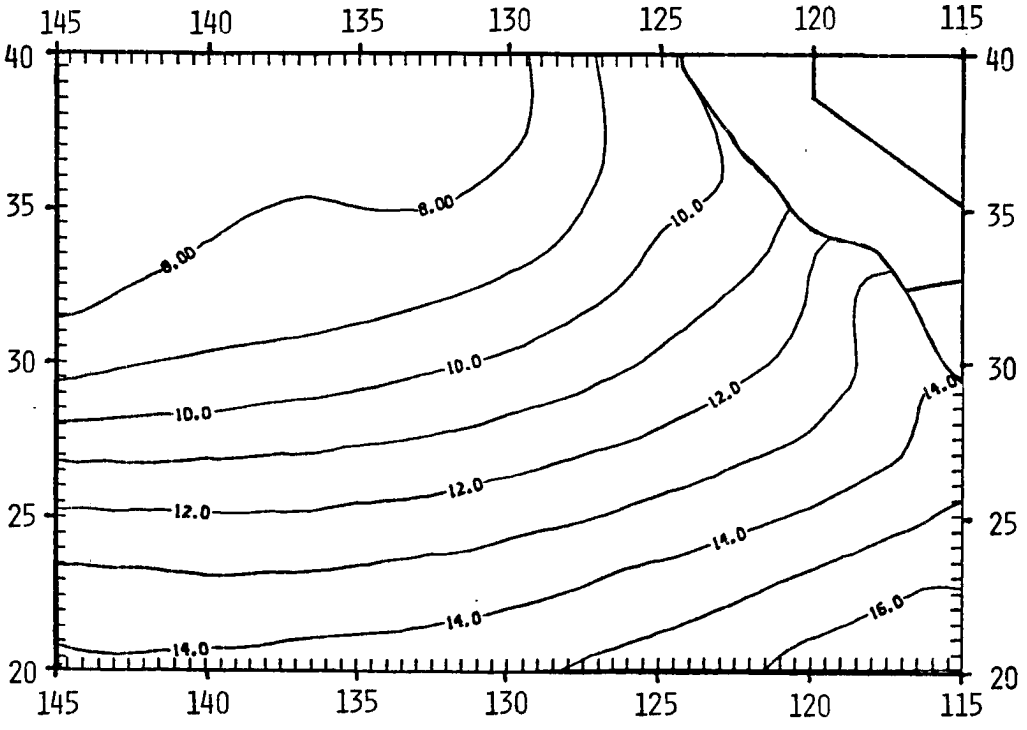

Figure 5.9b. Cloud-top temperature (°C).

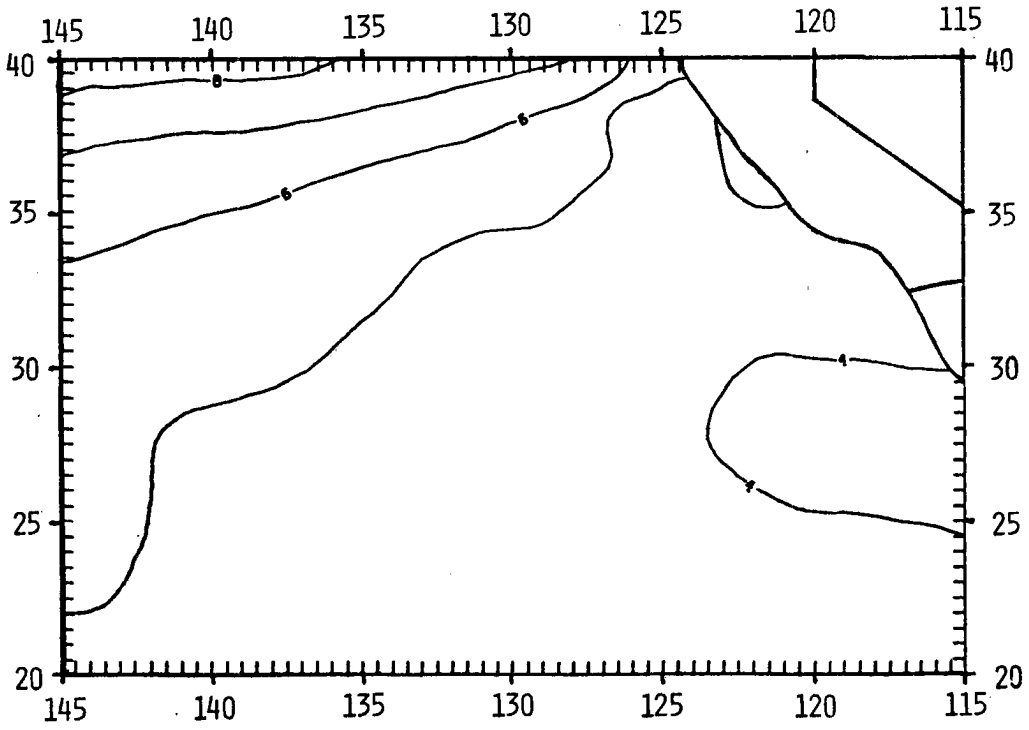

Figure 5.10. Cloud-top mass entrainment ($g\,m^{-2}\,s^{-1}$).

5.2 Comparison with observations

Only three of the several parameters presented earlier in this chapter were recorded in the observations of Neiburger et al. (1961). These three are cloud top height, temperature at cloud top, and the increase of temperature across the inversion. The observations are for the whole summer (June through September), while the model results are based on July data.

The inversion magnitudes observed by Neiburger et al. are shown in Figure 5.11a, and cloud-top temperatures in Figure 5.11b. The cloud top height field was previously shown in Figure 4.12.

Cloud top heights (Figures 4.12 and 5.2a) show a basic similarity in the northern portions of the grid, as would be expected from the initialization scheme. The fields are similar in that isolines run more-or-less north to south and there is an increase in height away from the coast. Isolines tend to follow the trajectories in the southwest, as would be expected from the long memory of z_B. In general, though, the comparison is good.

Comparison of Figures 5.9 and 5.11 indicates that there is better agreement between the model and observations for cloud top temperature than for the inversion magnitude. The general shape of the cloud top temperature model results is the same as the observations, with a maximum to the southeast and a minimum to the northwest. Inversion magnitudes produced by the model fit best near the coast, although in most cases they are larger than those observed.

Some insight into the model's inversion magnitude results may be gained by examination of Figure 1.3. The magnitude of this inversion

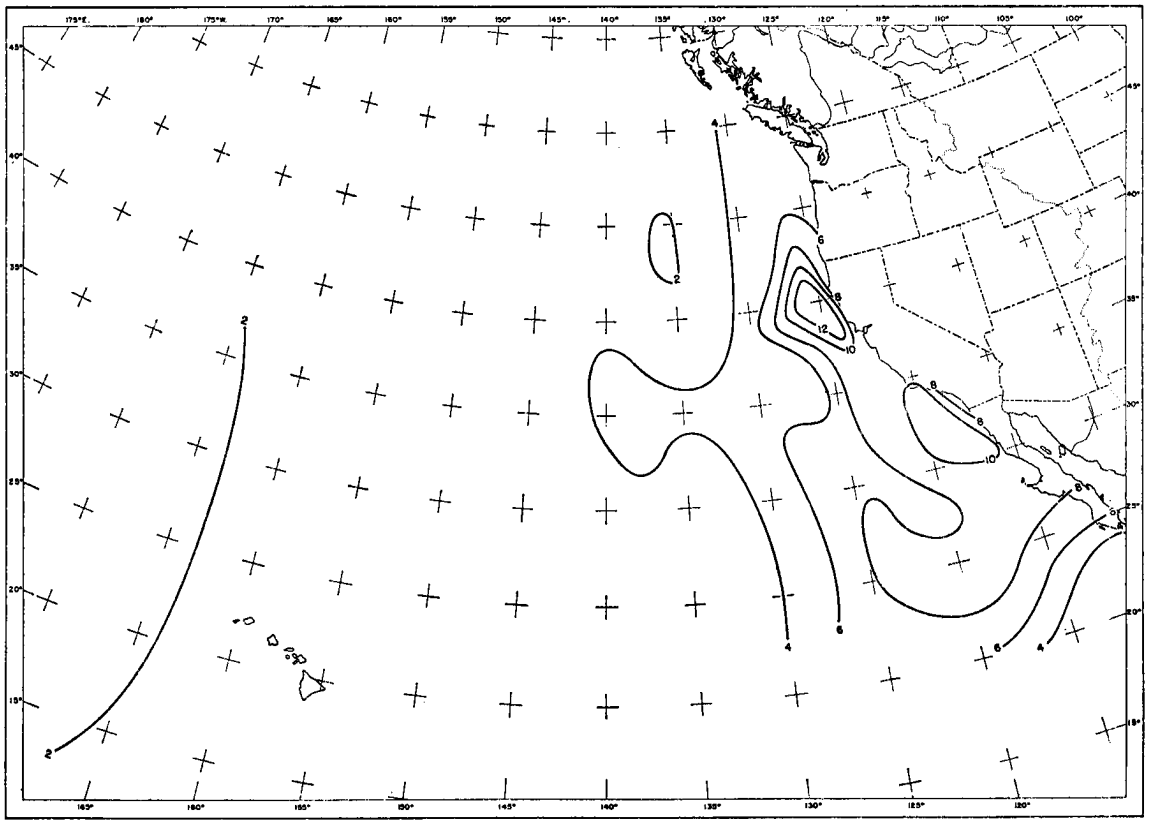

Figure 5.11a. June through September observations of inversion magnitude (°C). From Neiburger et al. (1961).

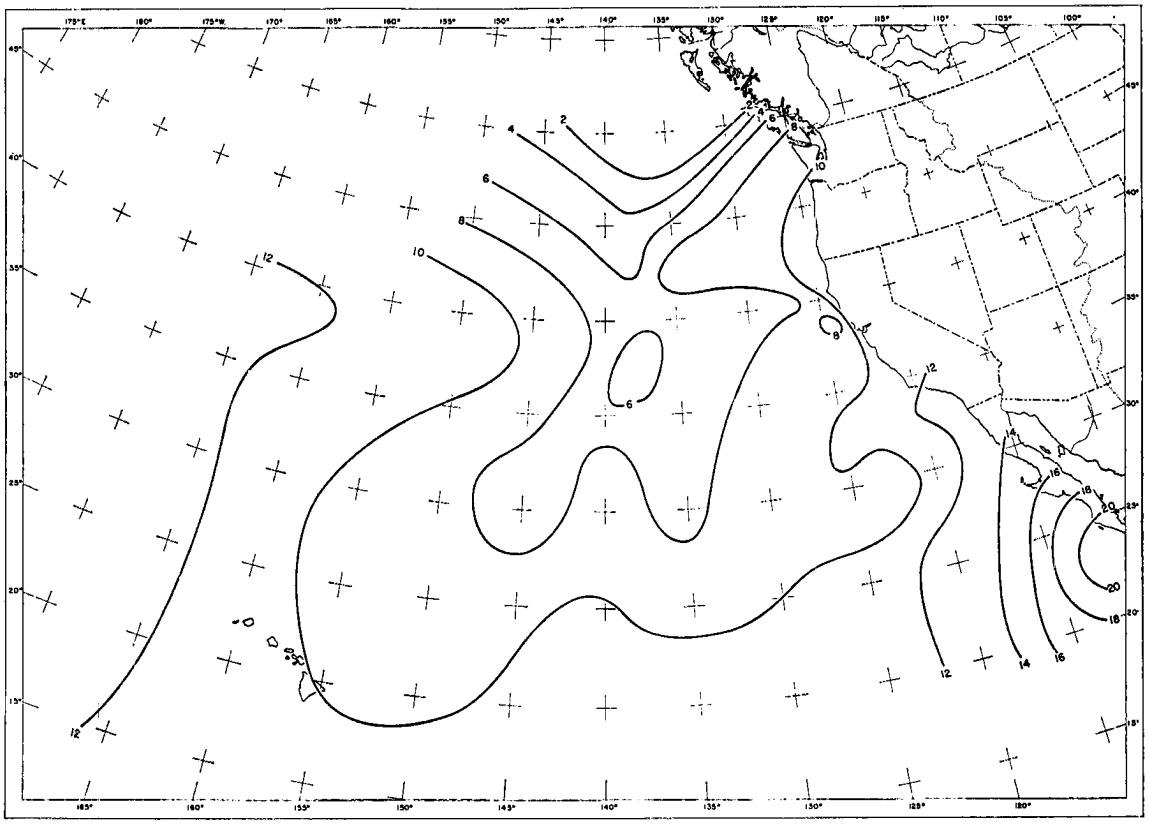

Figure 5.11b. June through September observations of cloud-top temperature (°C). From Neiburger et al. (1961).

would commonly be taken as about 12°C, i.e. the temperature difference between 95 kPa and 85 kPa. This of itself is a rather strong inversion, but the model assumes an inversion thickness approaching zero. Under this condition, the temperature above cloud top would continue down along the line above 85 kPa, intersecting the 95 kPa level at about 27°C. Thus, the model inversion is this case would have a magnitude of about 17° or 18°. The observational evidence of Neiburger et al. (1961), of course, does not indicate zero-depth inversions. This overestimate of inversion magnitude by the model explains in part the differences between Figures 5.9a and 5.11a.

5.3 Discussion

Section 5.2 demonstrated that the model's reproduction of the observed mixed layer features is adequate, but lacking in several respects. There are, however, a number of things which should be kept in mind when considering these results.

In the first place, it was noted above that the Neiburger et al. observations cover the period June through September, while the input data for the model were July only. Neiburger et al. (1961) indicate in their data that, at sixteen of the eighteen land or ship stations whose data were employed, the July incidence of inversion is greater than the summer average. This suggests the possibility that July inversions may have somewhat different characteristics than the all-summer average data presented. Steiner and Schubert (1977) found considerable differences in July and August model results over the eastern South Pacific.

A second basis for dissimilarity lies in the initialization procedure. Initialization of cloud base and air-sea temperature difference is hampered by the lack of observational data. Better initialization of these parameters could contribute to improving the model results. Both cloud base and air-sea temperature difference do adjust rapidly to local conditions, as can be seen by comparing z_c to $z_B/2$ and $T_S - T_{air}$ to zero at the initialization locations.

Problems at the coastline constitute a third source of error. In this case, the model has no provisions for landfall, so the results along the coast may be worse than those over open ocean. For example, the Bowen ratio is known to change dramatically from sea to land, but the model assumes a fictitious sea everywhere, so the flux of water vapor does not change over land. It has already been noted that the cloud-top temperature away from the coast is better modeled than that close to the coast.

Finally, it must be kept in mind when considering any climatologically-based study that most atmospheric systems are non-linear. Schubert et al. (1978a) have amply demonstrated that the steady-state results of this model are decidedly non-linear. This is of particular importance when trying to reproduce mean observations from mean data. It is quite likely that the stratocumulus field on any given day would be considerably different from either the model results presented here or the observational evidence presented by Neiburger et al. Furthermore, the length of some of the trajectories used in the model calculations is such that the traverse time for a parcel of air could be as much as 5½ days, a time period during which many changes would surely take place in the basic synoptic pattern.

For these reasons, the model results should not necessarily be expected to closely match the observed stratocumulus regime, nor should either of the two be expected to correspond to any single day's convection. The fact that the model approximately reproduces the observations speaks in its favor.

It should be noted that the improvement in the cloud-top height results gained by moving the initialization from 50°N to 40°N may be due in large part to the long memory of the mixed layer depth. Schubert et al. (1978b) have demonstrated that cloud-top height responds much more slowly to varing external conditions than do other properties of the mixed layer. It is therefore possible that much of the agreement between Figures 4.12 and 5.2a, especially along the southern coast of California, is due to the fact that the initialization is remembered by the model. Since other results show some significant improvements over the 50°N results (not shown), the shift to 40°N may be considered to be an acceptable move.

6. Summary and conclusion

Schubert's (1976) formulation of Lilly's (1968) model of a cloud-topped mixed layer has been used in a slightly modified form to model the stratocumulus convection over the eastern North Pacific Ocean. The model relates sea surface temperature, wind speed, large-scale divergence, and properties of the air above the mixed layer to the mixed layer properties and profiles of the vertical turbulent fluxes of moist static energy and total water mixing ratio.

The model's radiative parameterization has been slightly modified, with the most significant change being the relocation of shortwave heating from the cloud-top jump into the mixed layer. Experiments with diurnally-varying shortwave radiation have proven that this modification results in a more realistic diurnal behavior of the model clouds. Additionally, both longwave and shortwave radiation have been made functions of cloud thickness.

The effects on the model clouds of diurnally varying large-scale divergence have been briefly examined. While a diurnal variation in divergence does produce appropriately-varying cloud top heights, the response of cloud base height does not appear to be realistic.

With the model so modified, the model was run over climatologically-derived fields of sea surface temperature, divergence, and wind speed and direction, with upper air properties also based on climatology. The results, when compared to the climatology of the eastern North Pacific area compiled by Neiburger et al. (1961), show qualitative and a degree of quantitative agreement. It was noted that the use of climatological data introduces the probability of disagreement

due to non-linearities in the atmospheric response to external parameters.

Data taken during the Marine Stratocumulus Experiment in 1976 could possibly be of some use in comparing the model results to observations, but again the above sources of inconsistency must be considered. In addition, the data from that experiment cover only a small portion of the area modeled in this study.

Cloud-top temperature data on a day-to-day basis are available from satellite sensors, and such data could be used to verify the model results. Satellite data have been compared to cloud-top temperature data taken during the Marine Stratocumulus Experiment, with the results agreeing within one or two degrees.

Possible improvements of the model include the incorporation of day-to-day changes in the external fields described in chapter 4, such that the trajectories would become true trajectories rather than steady state streamlines. This could then allow the model to be used on a daily basis compared to actual synoptic conditions. This opens the door to the possibility of using the model as a forecasting tool, especially if a momentum budget were added, such that only the sea surface temperature and surface pressure would be specified. In addition, the imposition of a land-sea interface is probably required in order that the coastal convection be adequately modeled.

The model does appear to produce a cloud under any conditions; this is a potential problem for any predictive usage, since the stratocumulus do not form 100% of the time in all of this area. Resolution

of this problem would require a significant increase in the complexity of the model.

ACKNOWLEDGEMENTS

The authors wish to thank Drs. S. Cox and E. Maxwell for their critical reviews of the manuscript, which was typed by Ms. D. Chapman. The research reported herein was sponsored by the National Science Foundation through Grant ATM 76-09370.

REFERENCES

Agee, E. M., and R. P. Howley, 1977: Latent and sensible heat flux calculations at the air-sea interface during AMTEX 74. J. Appl. Meteor., 16, 443-447.

Albrecht, B. A., 1977: A time-dependent model of the trade-wind boundary layer. Atmos. Sci. Paper 267, Colorado State University, 174 pp.

Cox, S. K., 1973: Infrared heating calculations with a water vapor pressure broadened continuum. Q. J. Roy. Meteor. Soc., 99, 669-679.

Davis, J. M., S. K. Cox and T. B. McKee, 1978: Solar absorption in clouds of finite horizontal extent. Atmos. Sci. Paper 282, Colorado State University, 92 pp.

Deacon, E. L., and E. K. Webb, 1962: Interchange of properties between the sea and air. The Sea, Vol. 1, M. N. Hall, ed., Rockefeller Inst. Press, p.43.

Deardorff, J. W., 1976: On the entrainment rate of a stratocumulus-topped mixed layer. Quart. J. Roy. Meteor. Soc., 102, 563-582.

Hunt, G. E., 1973: Radiative properties of terrestrial clouds at visible and infrared thermal window wavelengths. Quart. J. Roy. Meteor. Soc., 99, 346-369.

Kraus, E. B., 1963: The diurnal precipitation change over the sea. J. Atmos. Soc., 20, 551-556.

Kraus, H., and E. Schaller, 1978: Steady-state characteristics of inversions capping a well-mixed PBL. To be published.

LaViolette, P. E., and S. E. Seim, 1969: Monthly charts of mean, minimum, and maximum sea surface temperature in the North Pacific Ocean. SP-123, U. S. Naval Oceanographic Office, Washington, D.C. 20390, 62 pp.

Lilly, D. K., 1968: Models of cloud-topped mixed layers under a strong inversion. Quart. J. Roy. Meteor. Soc., 94, 292-309.

Lowe, P. R., 1977: An approximating polynomial for the computation of saturation vapor pressure. J. Appl. Meteor., 16, 100-103.

Mack, E. J., U. Katz, C. Rogers and R. Pilié, 1974: The microstructure of California coastal stratus and fog at sea. Rep. CJ-5404-M-1, Calspan Corp.

REFERENCES Continued

Miller, D. B., and R. G. Feddes, 1971: Global atlas of relative cloud cover 1967-1970. Joint production by U. S. Dept. of Commerce and U. S. Air Force, Washington, D.C. [Available from NTIS, Springfield, Va., AD739434].

Miller, F. R., and M. R. Stevenson, 1974: Comparison of cloud top temperatures from satellites and sea surface temperatures along Baja California. Paper presented at V Congreso Nacional de Oceanografia, October 1974. [Available from the authors at Scripps Institution of Oceanography, LaJolla, California].

Neiburger, M., 1944: Temperature changes during formation and dissipation of West Coast stratus. J. Meteor., 1, 29-41.

_____, 1949: Reflection, absorption, and transmission of insolation by stratus clouds. J. Meteor., 6, 98-104.

_____, D. S. Johnson and C. W. Chien, 1961: Studies of the structure of the atmosphere over the eastern Pacific Ocean in summer, I, The inversion over the eastern north Pacific Ocean. Univ. Calif. Publ. Meteor., 1, 1.

Oliver, D. A., W. S. Lewellen and G. G. Williamson, 1978: The interaction between turbulent and radiative transport in the development of fog and low-level stratus. J. Atmos. Sci., 35, 301-316.

Paltridge, G. W., 1971: Solar and thermal radiation flux measurements over the east coast of Australia. J. Geophys. Res., 76, 2857-2865.

_____, 1974: Infrared emissivity, shortwave albedo and the microphysics of stratiform water clouds. J. Geophys. Res., 79, 4053-4058.

Schubert, W. H., 1976: Experiments with Lilly's cloud-topped mixed layer model. J. Atmos. Sci., 33, 436-446.

_____, J. S. Wakefield, E. J. Steiner and S. K. Cox, 1978a: Marine stratocumulus convection, Part I: Governing equations and horizontally homogeneous solutions. Submitted to J. Atmos. Sci.

_____, 1978b: Marine stratocumulus convection, Part II: Horizontally inhomogeneous solutions. Submitted to J. Atmos. Sci.

Steiner, E. J., and W. H. Schubert, 1977: Stratocumulus convection off the west coast of South America. Atmos. Sci. Paper 270, Colorado State University, 97 pp.

REFERENCES Continued

U. S. Dept. of Commerce, Environmental Science Services Administration, Environmental Data Service, 1967-70a: Climatological Data, National Summary, 18-21, 7. U. S. Government Printing Office, Washington, D.C.

_____, 1967-70b: Monthly Climatic Data for the World, 20-23, 7. U. S. Government Printing Office, Washington, D.C.

Wakefield, J. S., and W. H. Schubert, 1976: Design and execution of the marine stratocumulus experiment. Atmos. Sci. Paper 256, Colorado State University, 74 pp.

Yamamoto, G., M. Tanaka and K. Kamitani, 1966: Radiative transfer in water clouds in the 10-micron window region. J. Atmos. Sci., 23, 305-313.

_____, and S. Asano, 1970: Radiative transfer in water clouds in the infrared region. J. Atmos. Sci., 27, 282-292.

Zdunkowski, W. G., and W. K. Crandall, 1971: Radiative transfer of infrared radiation in model clouds. Tellus, 23, 517-527.

BIBLIOGRAPHIC DATA SHEET	1. Report No. CSU-ATSP-	2.	3. Recipient's Accession No.

4. Title and Subtitle

NUMERICAL SIMULATION OF EASTERN NORTH PACIFIC STRATOCUMULUS

5. Report Date: July, 1978

6.

7. Author(s): Joseph S. Wakefield and Wayne H. Schubert

8. Performing Organization Rept. No.

9. Performing Organization Name and Address

Department of Atmospheric Science
Colorado State University
Fort Collins, Colorado 80523

10. Project/Task/Work Unit No.

11. Contract/Grant No.: ATM 76-09370

12. Sponsoring Organization Name and Address

National Science Foundation

13. Type of Report & Period Covered

14.

15. Supplementary Notes

16. Abstracts

In this paper the theory first developed by Lilly (1968) of a cloud-topped mixed layer is employed in a slightly modified form to simulate stratocumulus convection in the eastern North Pacific Ocean. The radiative parameterization of the model is examined and, while the treatment remains simple, a significant change is made by moving the location of shortwave heating from the cloud-top jump into the mixed layer. In addition, shortwave absorption and longwave emissivity are made functions of cloud thickness. Several experiments are run to illustrate the effects of these changes on the mixed layer. The model's response to diurnal shortwave heating shows that the change in the heating profile results in a more appropriate diurnal variation in the mixed layer properties. Large-scale divergence is also subjected to a diurnal variation, such as might be observed due to a sea-breeze circulation. The model is numerically integrated over climatological fields of sea surface temperature, wind, and large-scale divergence along several two-dimensional trajectories.

17. Key Words and Document Analysis. 17a. Descriptors

17b. Identifiers/Open-Ended Terms

17c. COSATI Field/Group

18. Availability Statement	19. Security Class (This Report) UNCLASSIFIED	21. No. of Pages 115
	20. Security Class (This Page UNCLASSIFIED	22. Price